Transmission and Reflection Properties of Layered Left-Handed Materials

by

Jianbing James Chen

B.S., Fudan University, China (1992)
M.S., University of Mississippi (1997)

Submitted to the Department of Electrical Engineering and Computer Science
in partial fulfillment of the requirements for the degree of

Doctor of Philosophy

at the

MASSACHUSETTS INSTITUTE OF TECHNOLOGY
[February 2007]
Sept. 2006

Author .....
Department of Electrical Engineering and Computer Science
Sept. 18, 2006

Certified by .....
Jin Au Kong
Professor of Electrical Engineering
Thesis Supervisor

Accepted by .....
Arthur C. Smith
Chairman, Department Committee on Graduate Students

Transmission and Reflection Properties of Layered Left-Handed Materials

by

Jianbing James Chen

Submitted to the Department of Electrical Engineering and Computer Science
on Sept. 18, 2006, in partial fulfillment of the
requirements for the degree of
Doctor of Philosophy

Abstract

This thesis is concerned with the reflection and transmission properties of layered left-handed materials (LHM). In particular, the reflection properties of (LHM) slabs are studied for the Goos-Hänchen (GH) lateral shift phenomenon. We demonstrate a unique GH lateral shift phenomenon, which shows that both positive and negative shifts can be achieved using the same LHM slab configuration. This phenomenon is different from previously established cases where the GH lateral shift can be only negative or only positive when different LHM slab configurations are used. We also show that there exist two distinct cases with this unique phenomenon. One case has two regions of incident angles where the GH lateral shift directions are different, while another case has three regions with alternated GH shift directions. A generalized analytical formulation for analyzing the GH lateral shift direction is provided, which reveals that this unique phenomenon is related to the relative amplitudes of the growing and decaying evanescent waves inside the LHM slabs. The energy flux patterns within LHM slabs are further studied to show the influence of the evanescent waves on the GH shift direction change.

Furthermore, the transmission property of LHM slabs are studied on the finite slabs' imaging capability. First, the development of the numerical simulation tool - the Finite-Difference Time-Domain method (FDTD) - investigates the ability of the method to model a perfect lens made of a slab of homogeneous LHM. It is shown that because of the frequency dispersive nature of the medium and the time discretization, an inherent mismatch in the constitutive parameters exists between the slab and its surrounding medium. This mismatch in the real part of the permittivity and permeability is found to have the same order of magnitude as the losses typically used in numerical simulations. Hence, when the LHM slab is lossless, this mismatch is shown to be the main factor contributing to the image resolution loss of the slab. In addition, finite-size LHM slabs are studied both analytically and numerically since they have practical importance in the actual experiments. The

analytical method is based on Huygens' principles using truncated current sheets that cover only the apertures of the slabs. It is shown that the main effects on the images' spectra due to the size of the slabs can be predicted by the proposed analytical method, which can, therefore, be used as a fast alternative to numerical simulations. Furthermore, the property of negative energy streams at the image plane is also investigated. This unique property is found to be due to the interactions between propagating and evanescent waves and can only occur with LHM slabs, of both finite-size and infinite size.

The last part of the thesis deals with multi-layered media for the application to antenna isolations. The setup is with two horn antennas located beneath the ground plane with 10 λ distance apart. In order to reduce the coupling between antennas, multi-layered media placed on top of the ground plane need to be designed to suppress the fields. After the problem is simplified to the dipole antenna coupling in infinite slabs, the method to evaluate the fields inside layered media is presented. This method obtains the spectral domain Green's function first and then transforms the fields to the spatial domain using the Sommerfeld-type integration. After the method is validated using right-handed materials (RHM) from references, it is extended to include media like LHM as well as μ negative material and ϵ negative material . The validation with these materials are done by comparing the results with CST microwave studio simulations. The first configuration for the antenna isolation design if one layer slab backed by the grounded plane. Two different approaches are used to find the optimum slab parameters for the isolation. One approach is to use Genetic Algorithm (GA) to optimize the slab's constitutive parameters and the thickness for a minimum coupling level. The other approach is to develop an analytic asymptotic expression for the field, and then used the expression to design the slab parameters for the best isolation. We conclude that both approaches yield the same design for the given configuration. The effectiveness of the design is also validated on a grounded finite slab, which is the representation of the actual application. Finally, multi-layered media for the antenna isolation is studied. GA method is applied with an optimization scheme tailed for a five layered structure. We show that GA converges very fast to the solution and the result yields satisfactory isolation between the antennas.

Thesis Supervisor: Jin Au Kong
Title: Professor of Electrical Engineering

Acknowledgments

This thesis is the result of four years of work whereby I have been accompanied and supported by many people. It is a pleasant aspect I have now the opportunity to express my gratitude for them.

First of all, I would like to express my deep and sincere gratitude to Professor Kong. For a difficult subject like Electromagnetics, he has a keen ability to make it a fun topic. His humor, enthusiasm and dedication in teaching will always inspire me. As the advisor, Professor Kong gave me ample freedom to explore my research interests. He provided me with insightful suggestions and constructive critiques which have been of great value for me. His scholarly ideals and research philosophy have had a remarkable influence on me. I feel very fortunate to spend these years in his group.

I owe my most sincere gratitude to Dr. Grzegorczyk. He was always making himself available for discussions despite of his already busy and demanding schedule as a Research Scientist. His ability to simplify a complex problem and to illustrate a path for the solution made a deep impression on me. His passion for work, perfection in research and maturity in leadership made him a true role model for me. I thank him for the endless hours he spend on correcting all the papers I published during this study. Without his help, those research results can never be materialized. In many aspects, Dr. Grzegorczyk is truly a co-advisor for me.

My warm thanks are due to Dr. Bae-Ian Wu. He was the TA when I first took Prof. Kong's course. Needless to say, I received great help from him and had learned much from him. I am grateful for the fruitful discussions with him during the research meetings. I

often tapped into his expertise in FDTD and analytical methods. His guidance in the later part of my research is greatly appreciated.

I want to thank Professor Staelin, my thesis reader, for his effort in reviewing my thesis. I appreciate his interest in understanding my research results.

My sincere thanks are due to Dr. Hongsheng Chen. He had worked together with me in the antenna isolation part of the thesis. He provided me with valuable discussions and data to complete the work.

I am grateful to Dr. Xudong Chen, Dr. Jie Lu, Dr. Ben Barrows, Dr. Christopher Moss and Dr. Joe Pacheco who are the former colleagues in CETA. Xudong, Ben and Chris had been sharing an office with me until they graduated. Xudong was always enjoying challenging me with math riddles. He was a great office mate who really cared about other people. Ben got me into the world of Linux which I now appreciate more than Windows. Chris showed me the need to have fun in life. He upgraded his computer to play more video games rather to run more simulations. Dr. Jie Lu is another good friend of mine. His ability to bringing out physical insights in an engineering problem always impressed me. Dr. Pacheco is now working at Lincoln Lab. He is a great example to show how much you can achieve at a very young age.

I wish to extend my gratitude to my colleagues in CETA group – Brandon Kemp, Beijia Zhang, Bill Herrington, Song Liang Chua, Baile Zhang and Zhen Li. I thank them for the dinners we had together and the laughters we shared. I wish them the best in their graduate career.

In the beginning of my study, I had the opportunity to conduct research in Hypx group at Brigham and Women's Hospital. I appreciated the financial support from Dr. Mitch

Albert. Many of the people in Hypx group that I have come to know and become good friends since includes Xin Zhou, Yang-Sheng Tzeng, Joey Mansour, Jessica Gereige and Dr. Mary Mazzanti. I thank them for having me in their group and the help they gave me over the years.

I want to thank my parents for encouraging me to come to United States to study. Their unfailing support and trust helped me to go through many difficult times. I also want to thank my brother Haoying for his confidence in me and love for me.

I owe my loving thanks to my dear wife Sunny for her ever enduring love and for taking this journey together. I thank her for her sacrifice and understanding during my study at MIT. I also would like to thank our lovely daughter Lisa for bringing so much joy to our lives.

To Sunny and Lisa

Contents

List of Figures

List of Tables

Chapter 1

Introduction

1.1 Development of Left-Handed Materials

In the recent years, many of the new thrusts in electromagnetic research have been results of breakthroughs in other seemly unrelated research areas. One good example of such is the development of Left-handed materials.

The establishment of Maxwell's' equations connects the behaviors of electromagnetic waves to the the material's properties such as permittivity (ϵ) and permeability (μ). For media with positive constitutive parameters, which is abundant in nature, it is well-known that the triad of wavevector $\overline{k}$, electric field $\overline{E}$ and magnetic field $\overline{H}$ forms a right-handed system. For the purpose of differentiation, we terms such media Right-Handed Materials (RHM). What also exists in nature are ϵ negative materials (ENG) and μ negative materials (MNG). An example for ENG is a plasma medium. The permittivity of a plasma medium is frequency dispersive. In the frequency range below the plasma frequency, the permittivity takes negative values. The MNGs are not as common as ENGs, but they can found

as ferromagnetic materials. Considering the quadrants of values of permittivity and permeability, the only material that is missing from nature's abundance is the material with negative permittivity and negative permeability simultaneously. The idea of the existence of such materials was first pondered by Vessalago in 1968 [1]. From the Maxwell's equations, Veselago postulated several unusual phenomena related to the materials with both μ and ϵ being negative. He termed such materials "Left-handed materials" (LHM) due to left-handed system formed by the wavevector $\overline{k}$, electric field vector $\overline{E}$ and magnetic field vector ($\overline{H}$). However this idea remained as an academic curiosity for nearly half the century. With the rise of semiconductor process technology which enabled the fabrication of meta-materials (made from deposited metals in micro scales), the breakthrough came in the late 90's when Pendry proposed a theoretical design of meta-materials first with negative ϵ [2] then with negative μ [3], and in 2001 experiments by R.A.Schelby and colleagues [4] demonstrated a key phenomenon - Negative refraction - using materials with both negative μ and ϵ. The material constructed in the experiment used periodic structures with each element consisted of two square split rings (with an opening on the opposite side of each ring), and rods parallel to the plane of the rings. When the frequency of the incident magnetic field is close to the resonant frequency of the split rings, the structure becomes a resonant circuit. When losses are low, the induced magnetic energy can be very strong. As a result, the induced magnetic field can overpower the incident fields and the materials' permeability becomes negative. The permeability of the split rings LHM can be characterized by a Lorentz model due to the nature of its resonance. On the other hand, the negative permittivity was achieved by using periodic rods that resemble a plasma medium. When the incident electric fields are parallel to the rods, moving charges (i.e. currents) are induced

in the rods. The medium behaves as though there are free charges in space like in a plasma medium. The negative ϵ thus has a very wide frequency range. The lower limit of this range is determined by the minimum frequency required for treating the constructed material as a homogeneous medium, and upper limit is the plasma frequency of the rod structures.

Major drawbacks in the first LHM design with split rings are, firstly the high loss near the resonance frequency and secondly the narrow frequency band in which materials have LHM properties. In order to overcome these obstacles, many research efforts were devoted to developing new LHM materials design with lower loss and wider range of negative permeability. Notable achievements from these efforts were the designs with helicoil, Ω structure and "S" rings. Helicoil design [5] was used in the experiment and subwavelength resolution was demonstrated using a slab made of such materials. The Ω rings design was proposed to improve the bandwidth of the LHMs. The "S" rings design [6] [7] was shown to have lower loss and wider frequency band for LHM behavior. Generalization to 3-D structures had also been attempted [8].

1.1.1 Properties of LHMs

There are many unique properties due to the constitutive parameters μ and ϵ both being negative. First of all, the refractive index n of LHM is negative. From Maxwell's equations, $n = \sqrt{\mu\epsilon}$. It may be seen at first the *sign* of n is ambiguous since both positive and negative *sign* can be the solution. However if we examine the plane wave propagation inside LHM [9], we see that from $\overline{k} \times \overline{E} = \omega\mu\overline{H}$, the wave vector inside LHM is opposite to the one

in RHM. Therefore negative *sign* is the only allowed choice for n in LHM. This is the negative refraction property of LHM. An extension of negative refraction is the backward wave propagation inside the LHMs. This is due to the fact that the wavevector in LHM is opposite to the direction of the Poynting power vector. Inside LHMs, Cerenkov radiation has a backward propagating power due to the phase matching in the forward direction for wave vectors. When both dispersion and dissipation are considered in LHMs [10], it is found that both forward and backward power exist and the radiation angle is related to the loss.

For a LHM half space, the negative refraction bends the transmitted wave to the same side of the normal as the incident wave, while the bending indicating the RHM is to the opposite side of the normal. The negative refraction in LHMs has been confirmed in experiments in [11][12]. Due to the negative refraction, the propagating waves from a point source in RHM half space can be re-focused to an image point in LHM. The LHM can also restore the evanescent wave amplitudes at the image point. The Goos-Hänchen (GH) shift due to the total internal reflection is to the negative direction [13] instead of the positive direction for the RHM half space.

The properties of LHM slabs are the most studied research topic since the structure bears great importance in the practical applications. The seminal paper is the one by Pendry[14] which proposed the idea of perfect lens made of LHM slabs. Building upon the idea proposed by Veselago [1] that LHM slabs can focus the propagating waves into an image, Pendry further postulated that the evanescent waves can also be reconstructed to the same image. Therefore the entire spectrum of a source can be reproduced at the image plane yielding the name of a lens with a "perfect resolution". The sensitivity of

the image resolution to material properties was studied in [15], which showed that perfect lens can never be realized due to the loss and mismatch in the LHMs. In order to understand the imaging capability of practical LHM lens, many numerical simulation studies [16] [17] [18] [19] [20] were carried out, which concluded that subwavelength resolution instead of a perfect resolution can be achieved with LHM lens. Such a conclusion had been confirmed by experiments [5][21]. Studies on silver flat lens, which is an approximated version of LHM lens in the quasi-static limit, have also shown the image results with subwavelength resolutions [22][23][23] [24]. The perfect lens concept was further generalized to include anisotropic media [25] as well as with multifocal capability [26]. Besides subwavelength resolution property of LHM slabs, interesting GH lateral shift phenomena were also found for LHM slabs. The shifts with LHM slabs, depending on the material backing the slab, can be either positive or negative [27]. It was further found that the GH lateral shift can change directions as incident angle changes and the phenomena was explained by the energy flux changes inside the LHM slabs [28]. Furthermore, the guidance conditions with LHM slabs [29] have been investigated and showed that the imaginary wavevectors modes can be excited inside the LHM slabs in addition to the conventional real wavevectors modes. Furthermore, using the LHM slabs backed by a ground plane as antenna substrates, [30] [31] [32] showed that the antenna isolation and the leaky wave radiation can be tailored by the slab's properties. Lately, another interesting property with LHM slabs was found [33] which showed that a lossless LHM slab can localize the electromagnetic energy completely by placing two sources at each other's image location. This is because the image has the same amplitude as the source with an opposite phase therefore the radiated power is canceled.

For multi-layered LHM structures, the excitation of guided waves inside the slabs was studied in [34]. For general isotropic cases, the analytical formulation for the guided waves inside the multi-layered structure was presented in [9] and for bianisotropic stratified media in[35]. Beam shaping by a one-dimensional photonic crystal consisting of alternating slabs of two materials with positive and negative refractive index was studied in [36].

1.2 Overview of Thesis Work

In the thesis, the reflection and transmission properties of layered LHMs are studied. Chapter 2 deals with the reflection properties of LHM slabs, in particular the GH lateral shift phenomenon. A unique GH lateral shift phenomenon is found, which shows that both positive and negative shifts can be achieved using the same LHM slab configuration depending on the incident angle. We also show that there exist two distinct cases with this unique phenomenon. One case has two regions of incident angles where the GH lateral shift directions are different, while another case has three regions with alternated GH shift directions. A simplified analytical formulation is developed to study the dependence of the GH lateral shift direction on the slab parameters, from which we show that the phenomenon of both positive and negative GH shifts at different incident angles can be observed with LHM slabs. The formulation also reveals that this unique phenomenon is related to the relative amplitudes of the growing and decaying evanescent waves inside the LHM slabs. The energy flux patterns with LHM slabs are further studied to show the influence of the evanescent waves on the GH shift direction change.

Chapter 3 studies the transmission properties of LHM slabs with a focus on the imaging

capability of the LHM slabs. First, the development of a numerical simulation method - the Finite-Difference Time-Domain method (FDTD) - investigates the ability of the method to model a perfect lens made of a slab of homogeneous left-handed material (LHM). It is shown that because of the frequency dispersive nature of the medium and the time discretization, an inherent mismatch in the constitutive parameters exists between the slab and its surrounding medium. This mismatch in the real part of the permittivity and permeability is found to have the same order of magnitude as the losses typically used in numerical simulations. Hence, when the LHM slab is lossless, this mismatch is shown to be the main factor contributing to the image resolution loss of the slab. Furthermore, finite-size left-handed material (LHM) slabs are studied both analytically and numerically. The analytical method is based on Huygens' principles using truncated current sheets that cover only the apertures of the slabs. It is shown that the main effects on the images' spectra due to the size of the slabs can be predicted by the proposed analytical method, which can, therefore, be used as a fast alternative to the numerical simulations. Furthermore, the property of negative energy streams at the image plane is also investigated. This unique property is found to be due to the interactions between propagating and evanescent waves and can only occur with LHM slabs, both finite-size and infinite.

Chapter 4 of the thesis investigate multi-layered media properties for the application of antenna isolations. The antennas used in the setup are two horn antennas located under the ground plane and facing upward. Layered slab materials are placed in between antennas to suppress the coupling (i.e. to improve the isolation). After investigating the coupling between the horn antennas, the problem is simplified to the study of dipole antennas coupling in layered media. The method of spectral Green's functions is used to evaluate the

fields inside layered media from the transmission line analogy. Using Sommerfeld-type integrations, the fields are transformed back to the spatial domain. The spectral Green's function method is further extended to include LHM as well as μ negative material (MNG) and ϵ negative material (ENG) and the method is validated with examples. For the antenna isolation consideration, the configuration of a slab backed by a grounded plane is studied analytically for the guidance conditions for different materials. A design example is provided with the z directed dipole antenna coupling. Two different approaches are used to find the optimum slab parameters for the best isolation. One approach is to use Genetic Algorithm (GA) to optimize the slab's constitutive parameters and the thickness for a minimum coupling level. The other approach is to develop an analytic asymptotic expression for the field, which is then used to design the slab parameters for the best isolation. We conclude that both approaches yield the same design for the given configuration. The effectiveness of the design is also validated on a grounded finite slab, which is a closer representation of the actual application. In addition, possibility of using multi-layered media in place of the slab for the antenna isolation is studied. GA method is applied with an optimization scheme tailed for a five layered structure. We show that GA converges very fast to the solution and the result yields satisfactory isolation for the antennas.

Chapter 2

Goos-Hänchen (GH) Lateral Shifts

2.1 Introduction

The Goos-Hänchen (GH) lateral shift effect, which refers to the spatial displacement of the reflected beam along the interface between two media from an incident beam, has been studied for many years [37] [38] [39]. Recently, due to the emergence of LHM, the interest in the study of GH shifts has been renewed [13] [34] [40] . In this chapter, we consider a three media configuration as illustrated in Fig. 2-1, in which a beam is incident from medium #1 onto medium #2 (the slab) with the center of the beam at an angle θ_i from the normal. The spatial displacement S, or GH lateral shift, can be either positive or negative depending on the constitutive parameters of the three media. A positive GH lateral shift refers to a shift to the other side of the normal from the incident beam (which is the case shown in Fig. 2-1), while a negative shift refers to a shift on the same side of the normal as the incident beam. The GH lateral shift phenomenon can be explained by the fact that a Gaussian beam is a summation of plane waves with a Gaussian-tapered amplitude dis-

tribution around the incident angle θ_i. At incident angles greater than the critical angle, the plane waves undergo different phase changes due to total internal reflection and sum to form a laterally shifted reflected beam. The condition $k_1^2 > k_2^2$ needs to be satisfied in order for the critical angle to exist, where k_1, k_2 are the wave vectors of media #1 and #2, respectively.

For slab configurations, as depicted in Fig. 2-1, it has been shown that a slab of RHM embedded in free-space yields a positive GH shift, while a slab of LHM embedded in free-space yields a negative GH shift [40][41]. More recently, however, a positive GH shift has been demonstrated with an LHM slab [27]. This phenomenon has been shown to occur when the third medium is perfectly matched with the LHM slab, which refers to the situation where the respective permittivities and permeabilities of the slab and the third medium are opposite of one another (*i.e.* $\epsilon_2 = -\epsilon_3$ and $\mu_2 = -\mu_3$ in Fig. 2-1). Furthermore, it has been demonstrated that, for specific multi-layered LHM systems [34][36], both positive and negative GH shifts at different incident angles (referred to as *simultaneous* positive and negative GH shifts hereafter) can be obtained. In this chapter, we extend this study and show that the phenomenon of *simultaneous* positive and negative GH shifts can be demonstrated with a single slab of LHM and it is in fact a fundamental property of LHM slabs. An analytical study is carried out and reveals the connection between the GH lateral shift direction and the relative magnitudes of growing and decaying evanescent waves inside the slab. The energy flux line patterns associated with different GH shifts are studied, and the physical interpretation of the relation between GH shifts and evanescent waves is discussed.

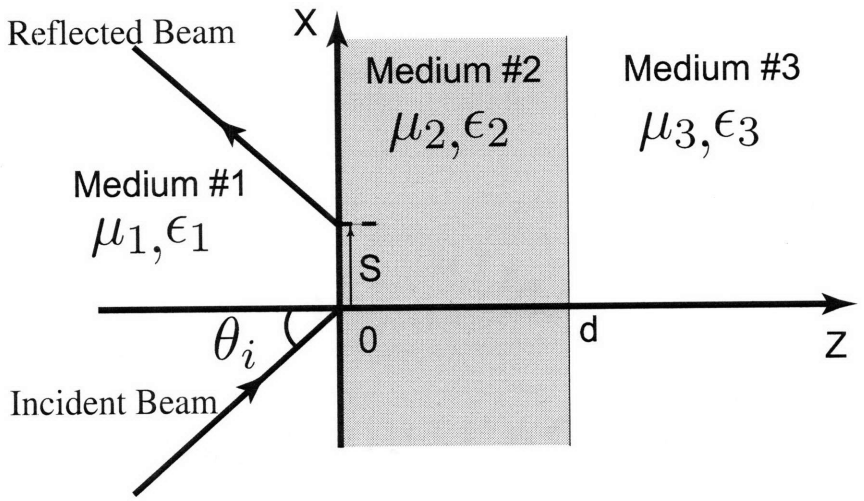

Figure 2-1: Configuration of a Gaussian beam incident upon a slab of thickness d and constitutive parameters (μ_2, ϵ_2). A GH lateral shift can be observed when $\theta_i > \theta_c$ (the critical angle).

2.2 Positive and Negative Lateral Goos-Hänchen Shifts With an Isotropic LHM Slab

The configuration of the problem under study is depicted in Fig. 2-1: a Gaussian beam centered at θ_i impinges onto a slab of material (which can be either RHM or LHM) backed by a half-space. This configuration can be analyzed using the formulation presented in [9] [42], where the fields as well as the reflection and transmission coefficients in multi-layer isotropic RHM and LHM have been derived. Using the same notation, for a Gaussian beam incident under a TE polarization, the incident electric field can be expressed as:

$$E_{1y}^{i}(x,z) = \int_{-\infty}^{\infty} \mathrm{d}k_x e^{ik_x x + ik_{1z} z} \psi(k_x) \tag{2.1}$$

where $\psi(k_x) = (g/2/\sqrt{\pi})\exp[-g^2(k_x - k_{ix})^2/4]$ and $k_1^2 = \omega^2\mu_1\epsilon_1 = k_x^2 + k_{1z}^2$. Eq. (2.1) describes the electric field with a Gaussian-shaped footprint of width g centered at $x = 0$

along the x axis. The incident beam is centered about $\overline{k}_i = \hat{x}k_{ix} + \hat{z}k_{iz} = \hat{x}k_1 \sin\theta_i + \hat{z}k_1 cos\theta_i$. In all three regions, the total electric field can be expressed as:

$$E_{iy}(x,z) = \int_{-\infty}^{\infty} \mathrm{d}k_x \left[A_i(k_x)e^{ik_{iz}z} + B_i(k_x)e^{-ik_{iz}z}\right] e^{ik_x x}\psi(k_x) \tag{2.2}$$

where i denotes region 1, 2 or 3. It is clear that $A_1 = 1$ and $B_3 = 0$, while the other coefficients can be obtained by letting $d_1 = 0$ and $d_2 = d$ in Eqns. 64–67 in [9] and replacing R, T, A, B with B_1, A_3, A_2, B_2 respectively.

When the Gaussian beam's incident angle θ_i is above the critical angle, each reflected plane wave (after a total internal reflection) carries a Goos-Hänchen phase shift $\Phi(k_x)$ which is a function of k_x, and recombines to form a reflected beam with a center locally shifted with respect to the incident beam. With the reflection coefficient $R(k_x)$ expressed as: $R(k_x) = e^{i\Phi(k_x)}$, under the linear approximation for the phase term $\Phi(k_x)$, the lateral shift can be characterized by [38]:

$$S = -\left.\frac{\partial\Phi(k_x)}{\partial k_x}\right|_{k_x=k_{ix}} \tag{2.3}$$

where S is the spatial displacement from the focal center of the incident beam (as shown in Fig. 2-1). For the slab, we have

$$\Phi(k_x) = -2\tan^{-1}\frac{p_{12}(1 - R_{23}e^{-2\alpha_{2z}d})}{1 + R_{23}e^{-2\alpha_{2z}d}} = -2\tan^{-1}F \tag{2.4}$$

where

$$F = \frac{p_{12}(1 - R_{23}e^{-2\alpha_{2z}d})}{1 + R_{23}e^{-2\alpha_{2z}d}} \tag{2.5}$$

and the Fresnel reflection coefficients R_{12} and R_{23} are defined as [42] :

$$R_{12} = \frac{1 - p_{12}}{1 + p_{12}}, \quad R_{23} = \frac{1 - p_{23}}{1 + p_{23}} \tag{2.6}$$

where

$$p_{12} = i\frac{\mu_1 \alpha_{2z}}{\mu_2 k_{1z}}, \quad p_{23} = \frac{\mu_2 \alpha_{3z}}{\mu_3 \alpha_{2z}} \tag{2.7}$$

We consider the cases when the incident angle θ_i is above the critical angle for both media 2 and 3 (*i.e.* $k_x^2 > k_2^2$ and $k_x^2 > k_3^2$), which dictates that both k_{2z} and k_{3z} are imaginary wavenumbers. In medium #3, we choose $k_{3z} = i\alpha_{3z}$ where α_{3z} is a positive real quantity so that the waves decay as z increases. In addition, it is known that the choice of the sign for k_{2z} does not affect the values of the reflection coefficient [27], so that $k_{2z} = i\alpha_{2z}$ is chosen, with α_{2z} being real and positive. After some mathematical manipulations (see Appendix A for details), the $sign$ of the GH shift S can be expressed as follows :

$$sign\{S\} = sign\left\{-\frac{\mu_{1r}}{\mu_{2r}}[C - C_1][C - C_2]\right\} \tag{2.8}$$

where

$$
\begin{aligned}
C &= B_2/A_2 = R_{23}e^{-2\alpha_{2z}d} \\
C_1 &= 2UV + \sqrt{4U^2V^2+1} \\
C_2 &= 2UV - \sqrt{4U^2V^2+1}
\end{aligned}
\tag{2.9}
$$

and

$$
\begin{aligned}
U &\equiv \frac{\alpha_{2z}k_{1z}^2}{k_1^2 - k_2^2} \\
V &\equiv d - \frac{(k_2^2 - k_3^2)\mu_{2r}\mu_{3r}}{\alpha_{3z}(\mu_{3r}^2\alpha_{2z}^2 - \mu_{2r}^2\alpha_{3z}^2)}
\end{aligned}
\tag{2.10}
$$

By introducing Eq. (2.8), we are able to analyze the GH shift direction change and its dependence on the incident angles and the slab's thickness. Although Eq. (2.3) can also be used for the parametric study of GH shifts, Eq. (2.8) has the advantage of directly relating the GH shift directions to the slab's parameters and the electromagnetic waves in the system. More importantly, the physical meaning of C is the ratio of the growing and decaying evanescent wave amplitudes inside the slab. Hence Eq. (2.8) reveals the connection between the GH lateral shift direction change and the variations of the ratio of the evanescent wave amplitudes inside the slab, which is further illustrated in Section 2.4.

Note that Eq. (2.10) has a singularity point at $\mu_{3r}\alpha_{2z} + \mu_{2r}\alpha_{3z} = 0$, which requires

Eq. (2.8) to be modified as

$$sign\{S\} = sign\Big\{-\mu_{1r}\mu_{2r}\big[(k_1^2-k_2^2)\alpha_{3z}^2 e^{-2\alpha_{2z}d} - (k_2^2-k_3^2)k_{1z}^2\big]\Big\} \tag{2.11}$$

The above singularity condition can be re-arranged as $\mu_{3r}/\alpha_{3z} + \mu_{2r}/\alpha_{2z} = 0$, which corresponds to the surface polariton condition for TE waves [34][43]. The surface polariton condition can also be viewed as the condition in which only one evanescent wave exists. As observed in [34], the excitation of forward (backward) surface waves can result in positive (negative) GH shifts. This can also be seen from Eq. (2.11) by ignoring the exponentially small term and observing that the GH shift direction is therefore determined by $k_3^2 \lessgtr k_2^2$, which can be further reduced to the forward and backward surface polariton condition $XY = (|\epsilon_{3r}|/\epsilon_{2r})(|\mu_{3r}|/\mu_{2r}) \lessgtr 1$. Hence Eq. (2.11) give a general relation between the GH shift direction and surface wave modes.

As an application of Eq. (2.8) when $\mu_{3r}/\alpha_{3z} + \mu_{2r}/\alpha_{2z} \neq 0$, we shall now show that LHM slabs in general exhibit the *simultaneous* positive and negative GH shifts at certain slab thicknesses. Note that C, C_1 and C_2 are real numbers and $C_1 > 0 > C_2$. Considering an electrically large thickness d, we can treat V as a positive variable increasing linearly as d increases and U as a positive constant. Then C_1 and C_2 can be approximated as:

$$C_1 \approx 2UV + 2UV(1 + \frac{1}{2}\frac{1}{4U^2V^2}) \approx 4UV \tag{2.12}$$

$$C_2 \approx -\frac{1}{4UV} \tag{2.13}$$

which says that $C_1 \propto d$ and $C_2 \propto d^{-1}$ for a large thickness d. Since C decays faster than C_2 ($C \propto e^{-\alpha_{2z}d}$), it becomes clear that $C_1 > C > C_2$. This means the GH shift direction is negative (positive) if an LHM (RHM) slab is used (according to Eq. (2.8)). As d decreases, C becomes greater than C_1 and C_2 in magnitude due to $|R_{23}| > 1$ and the GH shift becomes positive for an LHM slab. As an illustration, Fig. 2-2 shows a typical curve of C, C_1 and C_2 as functions of the slab's thickness d. Applying Eq. (2.8), it can be seen that for LHM slabs in general, the GH shift direction changes from positive to negative as d increases. Note that this does not happen to an RHM slab since the value of C starts within [C_2,C_1] (for positive GH shift at d close to zero) and stays within [C_2,C_1] as d increases. This explains why the GH shift is always positive for an RHM slab. Furthermore if we take the slab thickness which corresponds to the zero shift (intersect points of C and C_1 or C_2) and look at the GH shifts with different incident angles, the phenomenon of *simultaneous* positive and negative shifts can be observed. This is shown in Fig. 2-3 where the GH shift direction changes at different incident angles. Therefore this phenomenon is general to LHM slabs and it is associated with the fact that the GH shift direction can change from negative to positive as the LHM slab thickness becomes smaller. To verify the above results, Fig. 2-2 and Fig. 2-3 also show the GH shift amplitude changes as functions of the slab thickness and the incident angle with the help of Eq. (2.3). The phenomenon of *simultaneous* positive and negative GH shift effect is clearly observable.

Furthermore, using Eq. (2.8), we can classify the GH shift effects with LHM slabs into three cases. The first case is the unidirectional GH shift in which C is always in between C_1 and C_2 as the incident angle varies and the shift is always negative. An exception is when

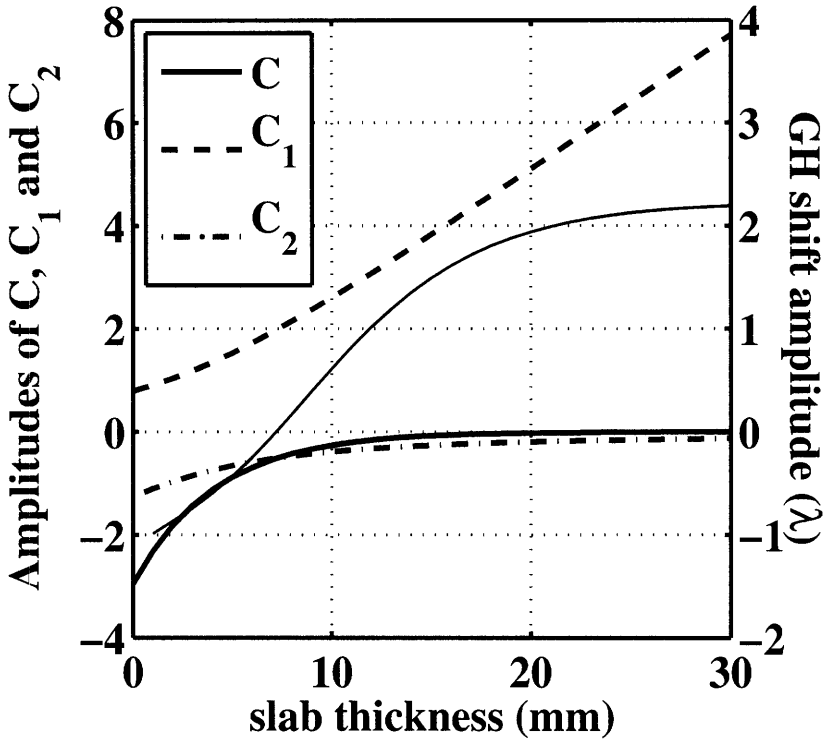

Figure 2-2: The values of C, C_1, C_2 and the shift amplitude are plotted as the slab thickness d varies. Slab's constitutive parameters are $\mu_{1r} = \epsilon_{1r} = 1$, $\mu_{2r} = \epsilon_{2r} = -0.5$, $\mu_{3r} = \epsilon_{3r} = 0.3$. The Gaussian beam is incident at 50° with a frequency of 10 GHz. The curves in legend are for C, C_1, C_2. The thin solid line is the shift amplitude curve.

the LHM is matched to region 3, C becomes infinite and the GH shift becomes positive. This case has been reported in [27] [40] . The second case is the *simultaneous* positive and negative GH shifts, where C changes from within $[C_2, C_1]$ to outside this range. This case has been illustrated above. The third case is the alternated positive and negative shifts, where C becomes infinite at a specific incident angle yielding a positive shift. Away from this angle, C is within $[C_2, C_1]$ and the shift becomes negative. This case is similar to the configuration in [44] where a "giant" negative lateral GH shift is reported at this specific incident angle.

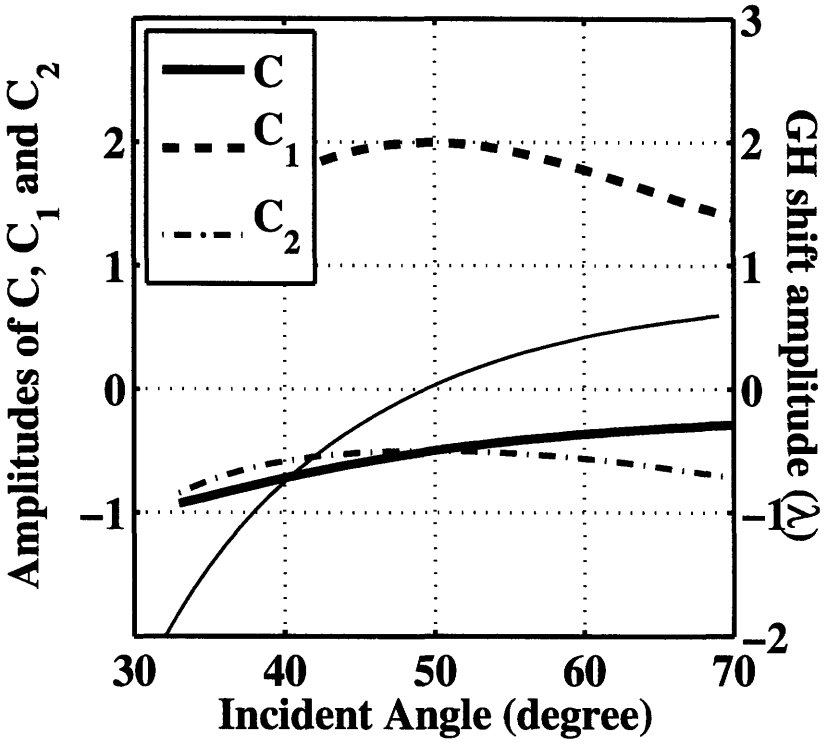

Figure 2-3: The values of C, C_1, C_2 and the shift amplitude are plotted as the incident angle varies. It can be seen that positive and negative GH lateral shifts at different incident angles occur at this configuration. Same constitutive parameters of the slab as in Fig. 2-2. Slab thickness is set to 7.31mm and The Gaussian beam's frequency is 10 GHz. The thin solid line is the shift amplitude curve.

2.2.1 Configurations with Unidirectional GH Lateral Shift Direction

In this section, we focus on the cases where the GH lateral shifts are unidirectional with the incident angles. These cases have been established previously [13][27], and our purpose is to apply Eq. (2.8) in order to identify the connections between the GH lateral shift direction and the ratio of the evanescent waves inside the slab. Since Eq. (2.3) suggests that the GH lateral shift direction can be predicted from the slope of the phase of the reflection coefficient R (opposite in sign), only the phases of R for these cases are plotted in this section.

i) When medium #2 is an RHM, the GH lateral shift is positive. An example is given in case 1 of Fig. 2-4(a) where the phase of R is plotted and the negative slope indicates a positive shift (from Eq. (2.3)). This result can also be seen from Eq. (2.8) by observing that C is always in between C_1 and C_2 (from Fig. 2-4(b)), and that μ_{1r}/μ_{2r} is positive. Fig. 2-4(b) also shows that the magnitude of C is much smaller than one, which is due to R_{23} being smaller than one for a positive p_{23} (from Eq. (2.6) and Eq. (2.7)). Since C is the ratio of evanescent wave amplitudes, a small value of C means that the decaying evanescent waves dominate inside the slab.

ii) When medium #2 is an LHM, it is known that the GH lateral shift can be negative. This is illustrated by the phase plot of R in case 2 of Fig. 2-4(a). This result can also be seen by using Eq. (2.8): since C is smaller than C_1 and greater than C_2 from Fig. 2-4(c) and since μ_{1r}/μ_{2r} is negative (medium 2 being LHM), the GH lateral shift is negative. Again Fig. 2-4(c) shows that the value of C is much smaller than one, which means the decaying evanescent waves dominate inside the slab, as in the previous case. From these two cases, it can be seen that since the value of C is small (much less than one), the GH lateral shifts are positive for RHM slabs and negative for LHM slabs. This has been the traditional observation of GH lateral shift with slabs established in [13][41][40].

iii) When medium #2 is an LHM that is matched to the RHM of medium #3 (i.e. $\mu_2 = -\mu_3$, $\epsilon_2 = -\epsilon_3$), unlike case (ii), the GH lateral shift is positive, as reported in [27]. This can be predicted from the phase plot of case 3 of Fig. 2-4(a). In this case, $p_{23} = -1$ from Eq. (2.7) so R_{23} and C are both infinite for all incident angles above the critical angle.

Applying Eq. (2.8), we see that the *sign* of S is determined by $-(\mu_{1r}/\mu_{2r})$ which indicates a positive shift. Compared with case (ii) where C is very small and decaying evanescent waves dominate inside the slab, C is now infinite and growing evanescent waves dominate inside the slab. In other words, when the GH lateral shift direction is changed, the value of C varies from much less than one to infinity. Note that in the cases shown here, the two different GH lateral shift directions happen with two different LHM slab configurations (one non-matched and one matched). In the following sections, we show that different GH lateral shift directions can be obtained with a single LHM slab.

2.2.2 Configuration With Two Regions of Different GH Lateral Shift Directions

In the previous section, the GH lateral shift direction flips from negative to positive when only medium #3 is changed, i.e. from mismatched to matched to medium #2 (the LHM slab). Since the continuous variation of medium #3 from mismatched to matched to medium #2 cannot result in the discontinuous change of GH lateral shift direction, there must be a new phenomenon in this transition. In fact, it is found that when the LHM used for medium #2 is slightly mismatched to the RHM of medium #3, namely $\mu_2 \approx -\mu_3$ and $\epsilon_2 \approx -\epsilon_3$, simultaneous positive and negative shifts can be observed with a single LHM slab. For the purpose of illustration, we use $\mu_{1r} = \epsilon_{1r} = 1$ for medium #1, $\mu_{2r} = \epsilon_{2r} = -0.51$ for medium #2, and $\mu_{3r} = \epsilon_{3r} = 0.5$ for medium #3. The phase plot of R for this configuration is shown in case (4) in Fig. 2-4(a), where it can be seen that the slope of the phase

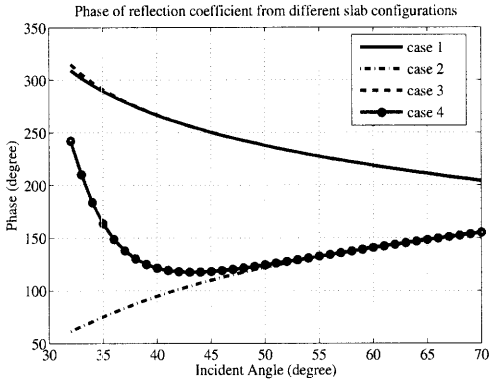

(a) Phase of the reflection coefficient for various slab configurations.

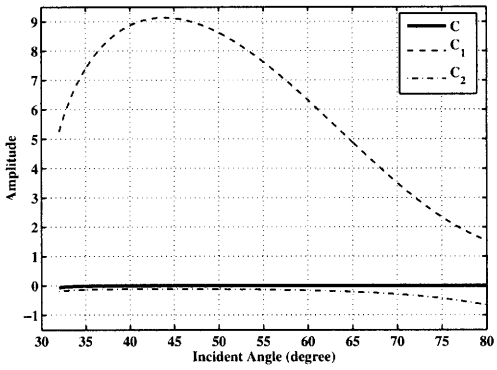

(b) Case 1: Values of C, C1 and C2.

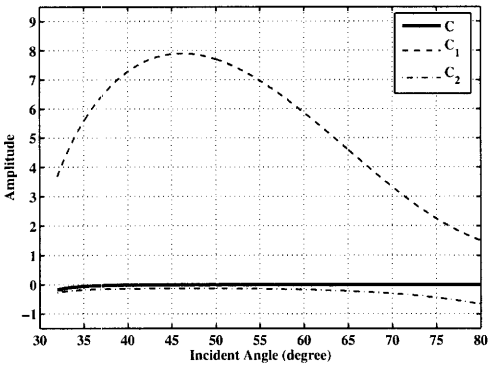

(c) Case 2: Values of C, C1 and C2.

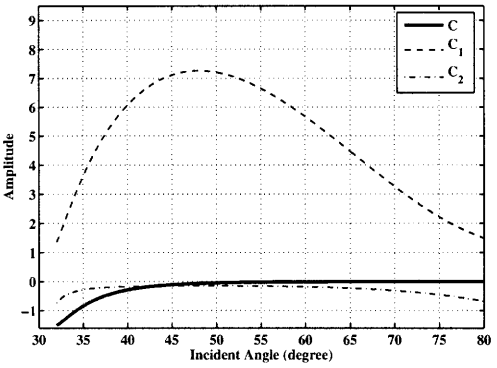

(d) Case 4: Values of C, C1 and C2.

Figure 2-4: The phase of reflection coefficients and values of C, C_1 and C_2. In all cases, the slab thickness is 3 cm and the plane wave frequency is 10 GHz. Other parameters are as follows: case 1: $(\mu_{1r}, \epsilon_{1r}) = (1, 1)$, $(\mu_{2r}, \epsilon_{2r}) = (0.5, 0.5)$, $(\mu_{3r}, \epsilon_{3r}) = (0.3, 0.3)$, case 2: $(\mu_{1r}, \epsilon_{1r}) = (1, 1)$, $(\mu_{2r}, \epsilon_{2r}) = (-0.5, -0.5)$, $(\mu_{3r}, \epsilon_{3r}) = (0.3, 0.3)$, case 3: $(\mu_{1r}, \epsilon_{1r}) = (1, 1)$, $(\mu_{2r}, \epsilon_{2r}) = (-0.5, -0.5)$, $(\mu_{3r}, \epsilon_{3r}) = (0.5, 0.5)$, case 4: $(\mu_{1r}, \epsilon_{1r}) = (1, 1)$, $(\mu_{2r}, \epsilon_{2r}) = (-0.51, -0.51)$, $(\mu_{3r}, \epsilon_{3r}) = (0.5, 0.5)$.

plot changes depending on the incident angle. Therefore, according to Eq. (2.3), it can be predicted that the lateral GH shift changes from positive to negative as the incident angle θ_i changes from near critical angle to near grazing angle.

In order to confirm the above observation, the method described in [27] has been used to calculate the reflected Gaussian beam magnitude pattern at the slab's first interface. In the calculation, only the propagating components of the Gaussian beam have been considered in the spectrum. Since the phase plot (case 4 of Fig. 2-4(a)) indicates that the change of the slope occurs around an incident angle of 43°, we choose $\theta_i = 35°$ and $\theta_i = 70°$ for the field calculations. The electric field magnitudes of the reflected Gaussian beams along $x = 0$ at these two different incident angles are plotted in Fig. 2-5. The change of GH lateral shift direction can be clearly observed from the figures, and the amount of shift can be verified by evaluating Eq. (2.3) from the values plotted in Fig. 2-4.

Like in the previous cases, this shifting property can be related to the value of C, i.e. to the ratio of amplitudes of the growing and decaying evanescent waves inside the slab. As mentioned before, when the decaying evanescent waves dominate inside the slab, the value of C is very small in magnitude and within the range $[C_1, C_2]$. From Eq. (2.8), it is clear that the GH shift is always unidirectional, namely RHM slabs give a positive shift and LHM slabs give a negative shift. Therefore, we expect a change of GH shift direction to be accompanied by a change of the value of C from within $[C_2, C_1]$ to outside this range. This is indeed the case as illustrated in Fig. 2-4(d): as the incident angle varies, the value of C varies from within $[C_2, C_1]$ to $(-\infty, C_2)$. When the incident angle θ_i is close to grazing

angle, the value of C is within $[C_2, C_1]$ and the GH lateral shift is negative. As θ_i gets closer to the critical angle, C grows in magnitude and moves into $(-\infty, C_2)$, and the GH lateral shift direction becomes positive. Therefore when the GH lateral shift direction changes with different incident angles, the values of C changes from one range to another, with the range boundaries specified by C_1 and C_2.

2.2.3 Configurations With Three Regions of Alternated GH Lateral Shift Directions

In the previous section, We have identified two regions of incident angles yielding different directions of GH lateral shift. In this section, three regions of incident angles with different GH lateral shift directions are identified.

The configuration used in this case is similar to the one reported in [44] where a "giant" negative lateral GH shift has been predicted. In [44], only unidirectional lateral GH shifts are discussed with medium #3 being LHM and media #1 and #2 being RHM. In our case, instead, the LHM is located in medium #2 (i.e. the slab) and the RHMs are used for media #1 and #3, to be consistent with the configurations we studied so far.

As mentioned in Section 2.2.1, when the LHM slab (or medium #2) is not matched with medium #3, the GH lateral shift is negative in general. It has been shown that for such cases, the value of C is small and in the range $[C_2, C_1]$. However by examining Eq. (A.6),

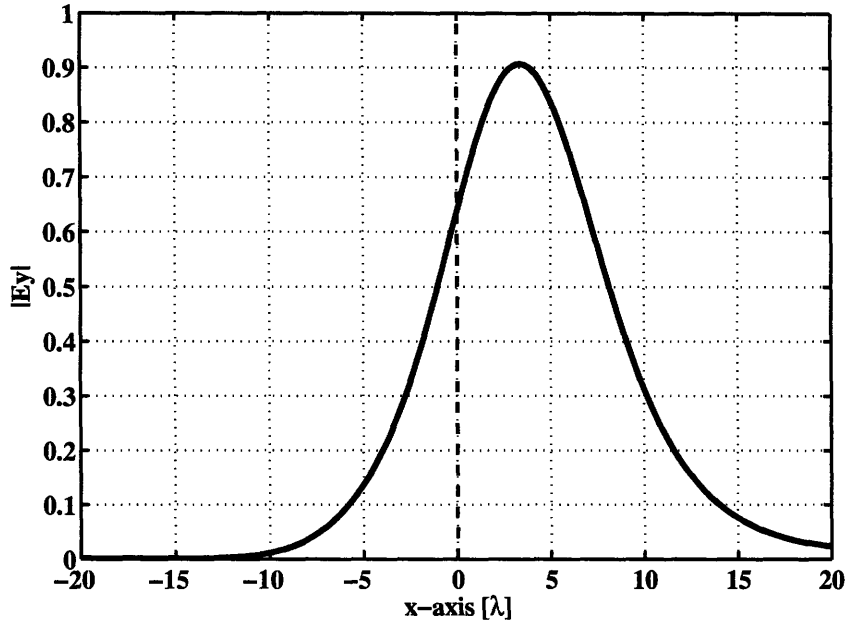

(a) Positive shift of 3.6λ observed at $35°$ incidence.

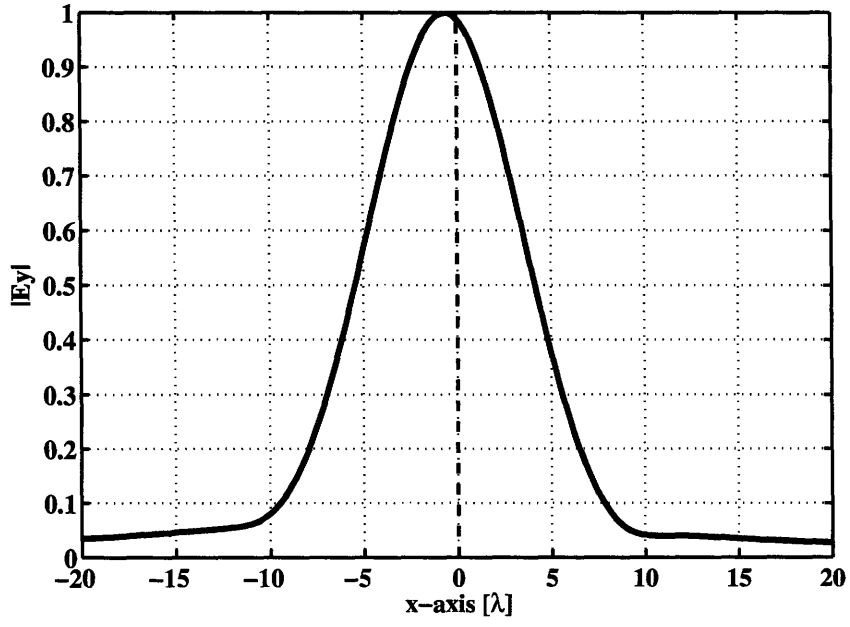

(b) Negative shift of -0.5λ observed at $70°$ incidence.

Figure 2-5: Reflected beam amplitude along the interface (x axis) where both positive and negative lateral shifts are observed with the same LHM slab at different incident angle. The first medium is free-space, the second medium has $\mu_{2r} = \epsilon_{2r} = -0.51$ and a thickness of 3 cm, and the third medium has $\mu_{3r} = \epsilon_{3r} = 0.5$. The incident is a TE polarized Gaussian beam at 10 GHz.

it is seen that C can still be infinite (i.e. p_{23}=-1) for a single specific incident angle even when the LHM slab is not matched to medium #3. In this scenario, the GH lateral shift becomes positive in the region around this incident angle, while in the other regions of incident angles the GH shifts remain negative. Therefore, this defines three regions with alternated GH shift directions. In order to illustrate this phenomenon, we choose the constitutive parameters as $\mu_{1r} = 1$, $\epsilon_{1r} = 1$, $\mu_{2r} = -1$, $\epsilon_{2r} = -0.6$, $\mu_{3r} = 0.6$, $\epsilon_{3r} = 1.24$. The phase plot of the reflection coefficient R is shown in Fig. 2-6(a). The critical angle of this setup is at 59.6° so the incident angle are swept from 60° up in order to remain above the critical angle. It is clear from Fig. 2-6(a) that the slope of the phase is positive except in the region between 64° and 67° where the slope becomes negative. Therefore it can be predicted that the GH lateral shifts are negative from 60° to around 64° and from around 67° to 85°, and positive from 64° to 67°. In order to validate the predictions of this phenomenon, field calculations have been done using the method presented in [27] to calculate the reflected beam's amplitude along the interface. From Fig. 2-7, it can be seen that indeed, at 65.5° the GH lateral shift is positive, while at 62° and 75° incident the GH shift is negative. Hence this defines three regions of alternated GH shift directions.

This phenomenon can also be explained by examining the change of C compared with C_1 and C_2 at different incident angles. As plotted in Fig. 2-6(b), starting from 60° incident, C is within $[C_2, C_1]$ which predicts a negative shift. As the incident angle increases to above 64°, C moves into the region of $(C_1, +\infty)$, which suggests a positive shift. Note that a discontinuity occurs at around 64.6° and C flips to a negative value and falls within $(-\infty, C_2)$ which again corresponds to a positive shift. As the incident angle extends be-

yond 67°, C moves back into $[C_2, C_1]$ and the GH lateral shift becomes negative. This is consistent with the observation from the phase plot of R in Fig. 2-6(a). The discontinuity of C at 64.7° incident is due to the fact that C is infinite (as the result of $p_{23} = -1$) at this specific incident angle so that only growing evanescent waves exist inside the slab. This is also called the resonant excitation of surface polaritons in [43] [44].

2.3 Finite Difference Time Domain Simulation of GH Shifts

The numerical simulation tools can be valuable means for the concept study or experimental designs. Due to the recent rapid advancements in computer technology, unattainable problems in the past are now solved routinely by computers. In the area of electromagnetics, the popular numerical methods include the Method of Moments (MoM), Finite Element methods (FEM) and Finite Difference Time Domain method (FDTD).

The Method of Moments is an Integral equation based method in which the unknowns (usually current distributions or charges in each discritized area) are approximated by basis functions (which are orthogonal functions). Green's functions (i.e. the kernel for the Integral Equations) are used to calculate the fields from the source. With the incident fields given, the boundary conditions are utilized to form a set of linear equations. The final step that is still needed is to invert the matrix and obtain the unknown. Compared with other methods, the Method of Moments provides better physical insight to the the problem at hand since the current distribution of the setup will be revealed after solving. However, the method also suffers from the requirement for the knowledge of the kernels (Green's

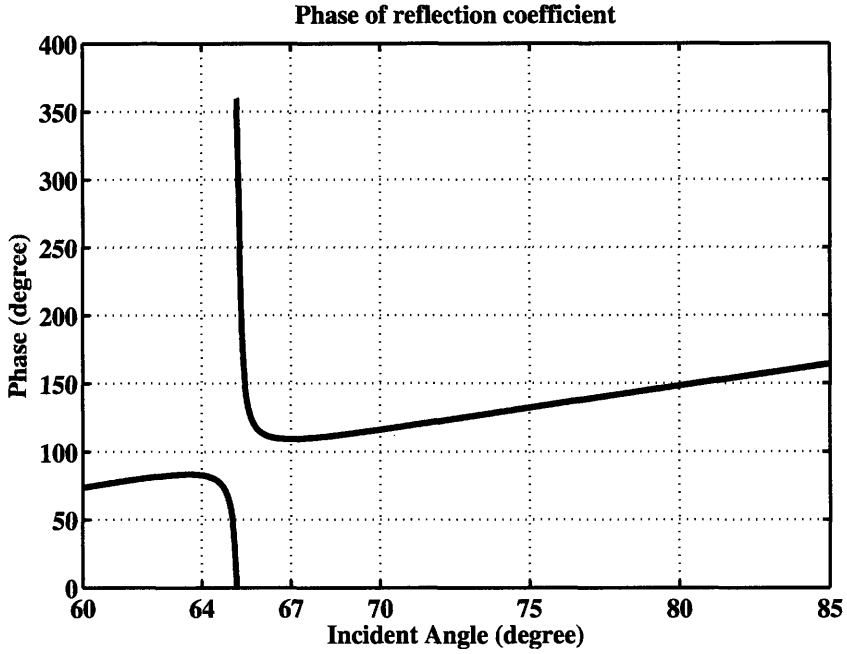

(a) Phase of the reflection coefficient.

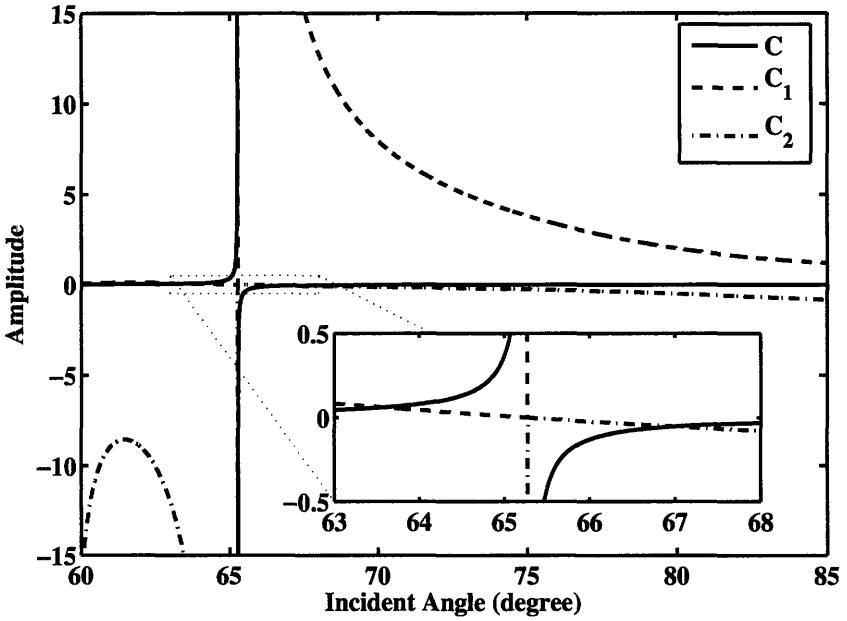

(b) Calculated value of C.

Figure 2-6: Plot of the phase of R and the values of C for the LHM configuration with the slab thickness of 3 cm and $(\mu_{1r}, \epsilon_{1r}) = (1, 1)$, $(\mu_{2r}, \epsilon_{2r}) = (-1, -0.6)$, $(\mu_{3r}, \epsilon_{3r}) = (0.6, 1.24)$. The incident wave is TE polarized at 10 GHz.

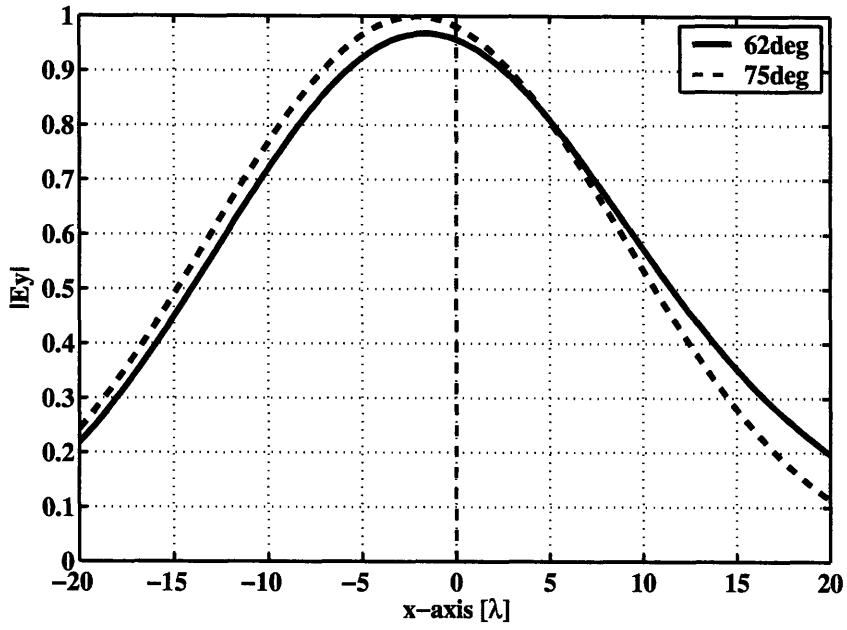

(a) Negative shifts of -1λ and -2λ at 62° and 75° respectively.

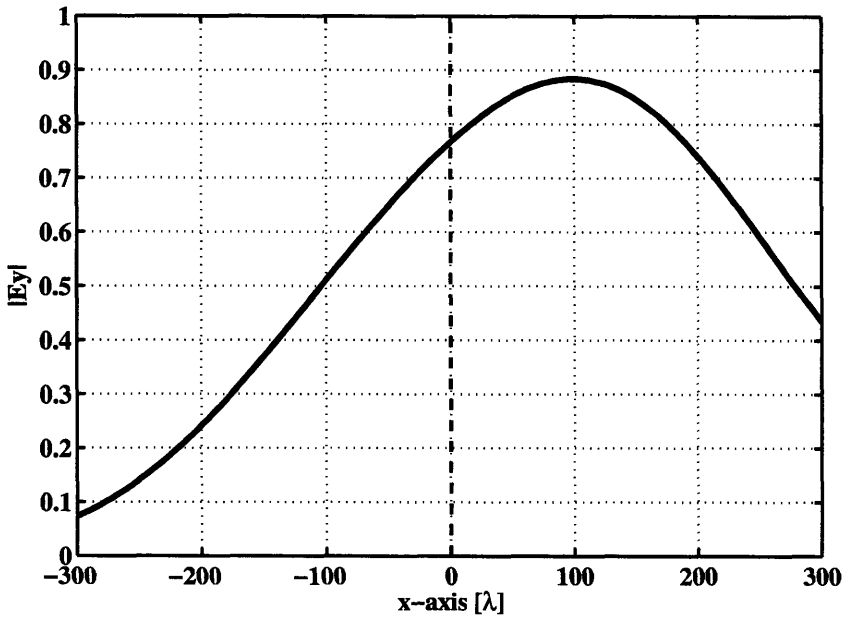

(b) Positive shift of 108λ at 65.5°.

Figure 2-7: Reflected beam amplitude along the interface (x axis) where different lateral shift directions are observed for the configuration of Fig. 2-6.

functions) of the problem, which is often impossible for a practical configuration. Despite this disadvantage, some commercial electromagnetic solver are based on MoM. The popular one is Agilent's Momentum for Integrated Circuit simulations in layered media environment.

Compared with MoM, the Finite Element method is more adapt to complex geometries. The FEM is also a frequency domain based method, like MoM. Instead of using the Integral Equations, FEM takes the differential form of the Maxwell's equations and applies the numerical difference method at the discritized grids (usually tetrahedral). The problem geometry can be of any arbitrary shape as long as the discretization scheme can be implemented. The accuracy of the solution depends on the finiteness of the discretization and the field changes. The popular commercial software based on FEM is HFSS from Ansoft.

The method we use for modeling the LHMs is FDTD. As the only time domain method, FDTD is a direct numerical solver of Maxwell's equations, either in differential form or integral form. The method has been proved to be efficient in solving problems with complex geometries. Since the frequency dispersive models have to be used to implement LHM, the readiness of converting these models into a differential form in time domain makes FDTD the ideal candidate for the simulation.

The simulation is setup in TE mode so the fields to be solved are E_y, H_x, H_z. The dispersive material is modeled by introducing polarization currents in the Maxwell's equa-

tions [45].

$$\epsilon(\omega) = \epsilon_o \left(1 - \frac{\omega_{pe}^2}{\omega(\omega + i\Gamma_e)}\right)$$
$$\mu(\omega) = \mu_o \left(1 - \frac{\omega_{pm}^2}{\omega(\omega + i\Gamma_m)}\right) \tag{2.14}$$

The dispersive permittivity can be treated as the result of polarization current with the form of

$$\overline{D} = \epsilon_o \overline{E} + \overline{P} = \epsilon(\omega)\overline{E} \Rightarrow \overline{P} = -\epsilon_o \frac{\omega_{pe}^2}{\omega(\omega + i\Gamma_e)} \overline{E} \tag{2.15}$$

Converting the frequency domain expression to time domain, we have

$$\frac{\partial^2 \overline{P}}{\partial t^2} + \Gamma_e \frac{\partial \overline{P}}{\partial t} - \epsilon_o \omega_{pe}^2 \overline{E} = 0 \tag{2.16}$$

Let $J_e = \partial P / \partial t$, Eq. (2.16) can be inserted into Maxwell's equations so we have

$$\nabla \times \overline{H} = \frac{\partial \overline{D}}{\partial t} = \epsilon_o \frac{\partial \overline{E}}{\partial t} + \frac{\partial \overline{P}}{\partial t} = \epsilon_o \frac{\partial \overline{E}}{\partial t} + \overline{J_e}$$
$$\frac{\partial \overline{J_e}}{\partial t} + \Gamma_e \overline{J_e} = \epsilon_o \omega_{pe}^2 \overline{E}$$

A similar approach can be applied to $\mu(\omega)$. After the manipulation, we have a set of

update equations for FDTD for TE mode:

$$\frac{\partial H_x}{\partial t} = \frac{1}{\mu_o}(\frac{\partial E_y}{\partial z} - J_{mx})$$
$$\frac{\partial H_z}{\partial t} = \frac{1}{\mu_o}(\frac{\partial E_y}{\partial x} - J_{mz})$$
$$\frac{\partial E_y}{\partial t} = \frac{1}{\epsilon_o}(\frac{\partial H_x}{\partial z} - \frac{\partial H_z}{\partial x} - J_{ey})$$
$$\frac{J_{mz}}{\partial t} + \Gamma_m J_{mz} = \mu_o \omega_{pm}^2 H_z$$
$$\frac{J_{mx}}{\partial t} + \Gamma_m J_{mx} = \mu_o \omega_{pm}^2 H_x$$
$$\frac{J_{ey}}{\partial t} + \Gamma_e J_{ey} = \epsilon_o \omega_{pe}^2 E_y$$

Note that the J_m are at the same location as H_z but get updated at the same time step as E_y. vis versa, J_e are at the same location as E_y but get updated at the same time step as H_z.

The above update equations are implemented in the standard FDTD second order accurate central difference scheme. To validate the simulation results, we consider first a RHM slab in vacuum. The RHM has the property of $[\mu_r = 0.5, \epsilon_r = 0.5]$. In the FDTD setup, PML is used for the absorbing boundary condition which truncates the computation domain to a finite size. The RHM slab is modeled as a finite slab with a length of 20λ. The incident Gaussian beam is at 50° to the center of the slab. The beam width is chosen as $2\lambda_o$. The fields calculated in FDTD are the total fields including both the incident beam and the reflected beam, so an extraction method needs to be used to separate the reflected fields from the incident ones. This is done by calculating the incident beam using analytical formulations simultaneously while FDTD is updating the total field. Therefore, the values of

incident field and the total fields are synchronized. Once the simulation reaches the steady state, the total fields is subtracted from the incident field to obtain the reflected fields. The resulting reflected fields are in the time domain , therefore the amplitude of the fields are readily available.

The result for the RHM slab is shown in Fig. 2-8 Three curves are obtained from three different meethods. Both results from Drude Model and non-dispersive model is from FDTD simulation. The non-dispersive model use the values of μ_r and ϵ_r directly without any dispersive model. The analytical result is for the infinite slab. It can be seen that the results from three methods agree very well, which means the implementation of Drude Model is accurate and the size of the slab is long enough to be considered as infinite.

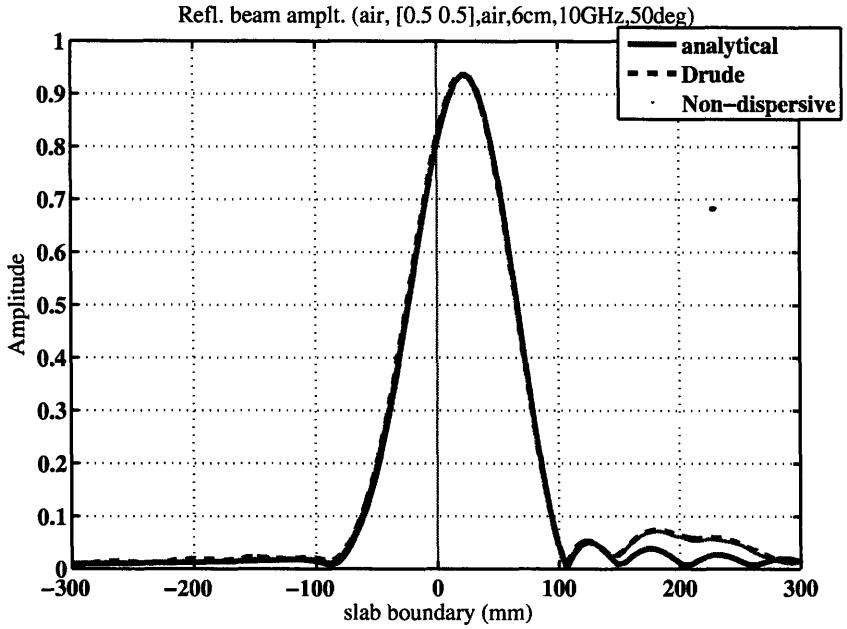

Figure 2-8: Reflected beam amplitude along the interface. the slab is with $\mu_r = \epsilon_r = 0.5$ and a thickness of 3cm. The TE incident beam is at 50°. The frequency is 10 GHz.

The second example is to replace the RHM slab with LHM slab. The LHM slab is setup to have the property of $(\mu_r = -0.5, \epsilon = -0.5)$. Only Drude Model can be used for LHM in

FDTD and is compared with the analytical result, which is shown in Fig. 2-9 As predicted, the shift is in the negative direction.

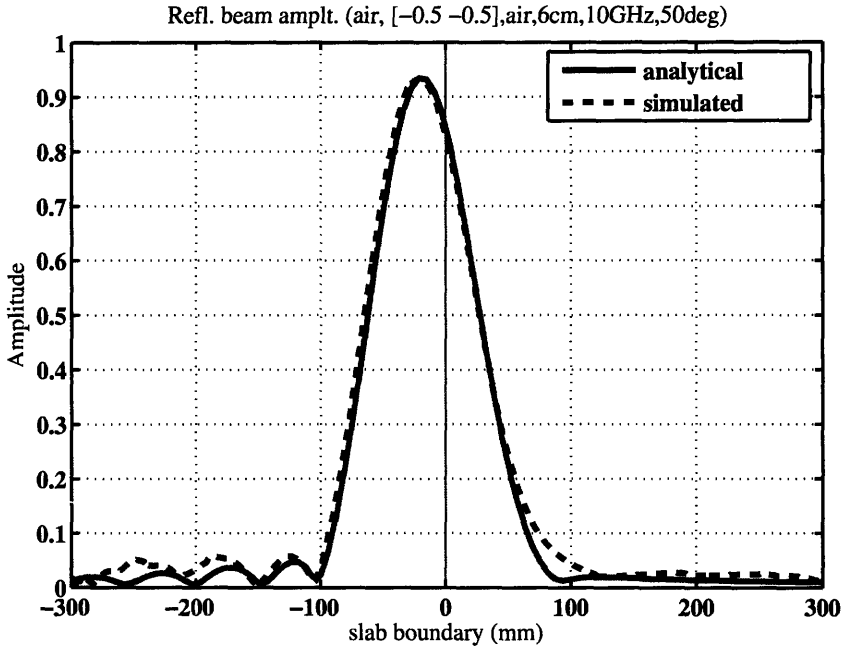

Figure 2-9: Reflected beam amplitude along the interface. the slab is with $\mu_r = \epsilon_r = -0.5$ and a thickness of 3cm. The TE incident beam is at 50°. The frequency is 10 GHz.

The third example is an interesting case in which the half space of vacuum is replace by half space of material with $(\mu_r = \epsilon_r = 0.5)$. So the material is matched with slab. The shift is now in the positive direction as shown in Fig. 2-10

Again the agreement between the simulation and the analytical result is excellent. These results show that FDTD method can be a useful tool to model accurately the GH shift phenomena.

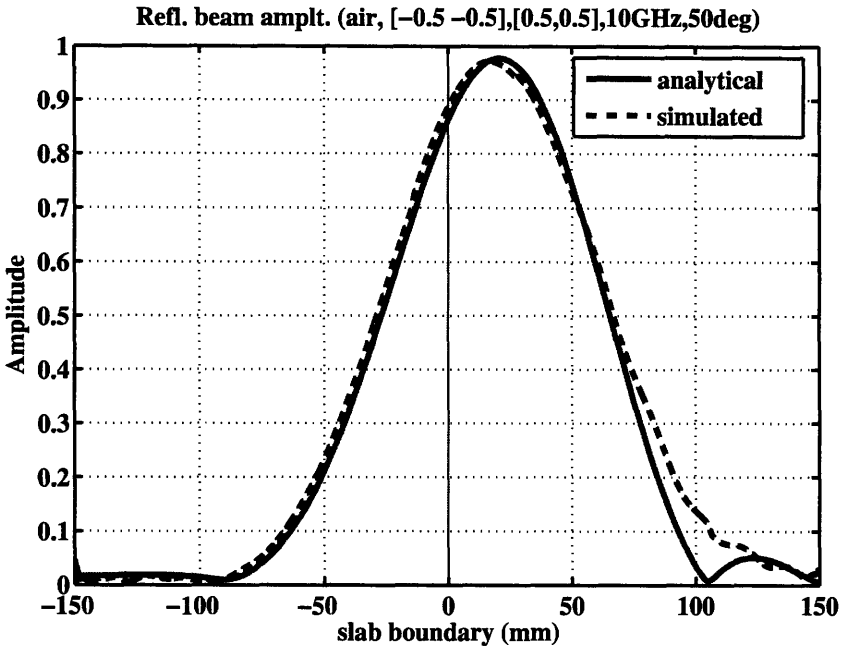

Figure 2-10: Reflected beam amplitude along the interface. the slab is same as in Fig. 2-9, and it backed with matched LHM with $\mu_r = \epsilon_r = 0.5$. The TE incident beam is at 50°. The frequency is 10 GHz.

2.4 Energy Flux With LHM Slabs

It has been shown in the previous sections that the existence of a *simultaneous* positive and negative GH shift at different angles is due to the fact that the GH shifts can change directions as the LHM slab thickness becomes smaller. The changes of GH shift directions at different slab thicknesses can be understood intuitively. For a very thin LHM slab (relative to the wavelength), the presence of the slab has little effect on the waves and the total internal reflections are mainly due to the third medium resulting in positive GH shifts. For an electrically thick LHM slab, however, the total internal reflections are mainly due to the LHM slab, yielding a negative GH shift. In between these two extremes, there exist *simultaneous* positive and negative GH shifts. In addition, a unique property of the LHM slab is that depending on the constitutive parameters, a slab can be electrically thick but

still yield a positive GH shift as if the slab were electrically thin. As an extreme example, when the LHM slab is exactly matched to the third medium, the GH shift is always positive regardless of the slab thickness. The physical reason for this effect is related to the energy flux pattern inside the slab, which is addressed subsequently.

With the total electric and magnetic fields in all three media calculated using the formulas in [9], the time averaged Poynting vector $< \overline{S} >$ can be calculated by evaluating $< \overline{S} >= \frac{1}{2} Re\{\overline{E} \times \overline{H}^*\}$ and the flux lines can be obtained using $dz/dx = S_z/S_x$. For the purpose of illustration, a slab configurations of ($\mu_{1r} = \epsilon_{1r} = 1$), ($\mu_{2r} = \epsilon_{2r} = -0.5$) and ($\mu_{3r} = \epsilon_{3r} = 0.507$) is used. This choice yields d=30 mm (one wavelength at the beam's frequency of 10 GHz) for zero GH shift at 50° incident angle. In order to observe a negative GH shift at 50° incident, we choose the slab thickness to be 50 mm. The energy flux lines in all three media are plotted in Fig. 2-11(a). It can be seen that vortex-like energy flux line loops are formed at both RHM/LHM interfaces, which has also been confirmed in LHM waveguides [46]. For a large slab thickness d, the coefficients A_2 and B_2 of E_{2y} (the electric field inside the slab) can be approximated as:

$$A_2 \approx \frac{2}{1+P_{12}} e^{\alpha_{2z} d} = T_{12} e^{\alpha_{2z} d}$$
$$B_2 \approx \frac{2R_{23}}{1+P_{12}} e^{-\alpha_{2z} d} \approx 0$$

Therefore around the first interface, E_{2y} can be approximated using only the decaying evanescent waves (associated with the coefficient A_2) when the thickness d is very large. At the second interface, which is between media #2 and #3, the ratio of the two evanescent

wave magnitudes is

$$\left|\frac{B_2 e^{\alpha_{2z}d}}{A_2 e^{-\alpha_{2z}d}}\right| = |R_{23}| > 1 \tag{2.17}$$

which is independent of the slab thickness d. Hence at the second interface, independent of the slab thickness, the growing evanescent waves dominate the decaying evanescent waves. To visualize this result, energy flux lines are plotted in Fig. 2-11(b) for decaying evanescent waves only (with the coefficient A) and in Fig. 2-11(c) for growing evanescent waves only (with the coefficient B). It is obvious that decaying evanescent wave flux lines resemble the total flux lines at the first interface while the growing evanescent wave flux lines resemble the total flux lines at the second interface. Since the observation of the GH shift effect is at the first interface, the flux lines at the first interface determine the shift direction. Furthermore it can be seen that with only decaying evanescent waves, as in Fig. 2-11(b), the flux line pattern is similar to the half space configuration as shown in [47]. These flux lines are in the negative direction and therefore, give a negative GH shift. As the slab thickness decreases, the flux line pattern at the second interface does not change, however, the pattern at the first interface does. Fig. 2-12(a) shows the Poynting vectors and flux line pattern for a zero GH shift (at d=30mm), while Fig. 2-12(b) shows the Poynting vectors and flux line pattern for a positive GH shift with a thinner slab thickness. It can be observed that as the second boundary moves closer to the first boundary (i.e. the slab becomes thinner), the growing evanescent wave flux line pattern gradually becomes prominent at the first interface. For positive GH shift, the growing evanescent wave pattern completely dominates the first interface. Therefore, the GH shift direction change is due to the energy flux pattern change inside the LHM slab, which is the consequence of the ratio change between the two

different evanescent wave amplitudes inside the slab. This relation is precisely expressed mathematically as Eq. (2.8).

2.5 Conclusion

We have shown theoretically that the GH lateral shift of a Gaussian beam can be both positive and negative at different incident angles with a single LHM slab. This phenomenon can be presented mathematically by the expression given in this chapter, and be explained physically by considering the energy flux line pattern changes inside the slabs. Furthermore, we have also shown that the unique ability of LHM slabs to amplify evanescent waves, already used for the design of a perfect lens, is responsible for the GH shift direction change.

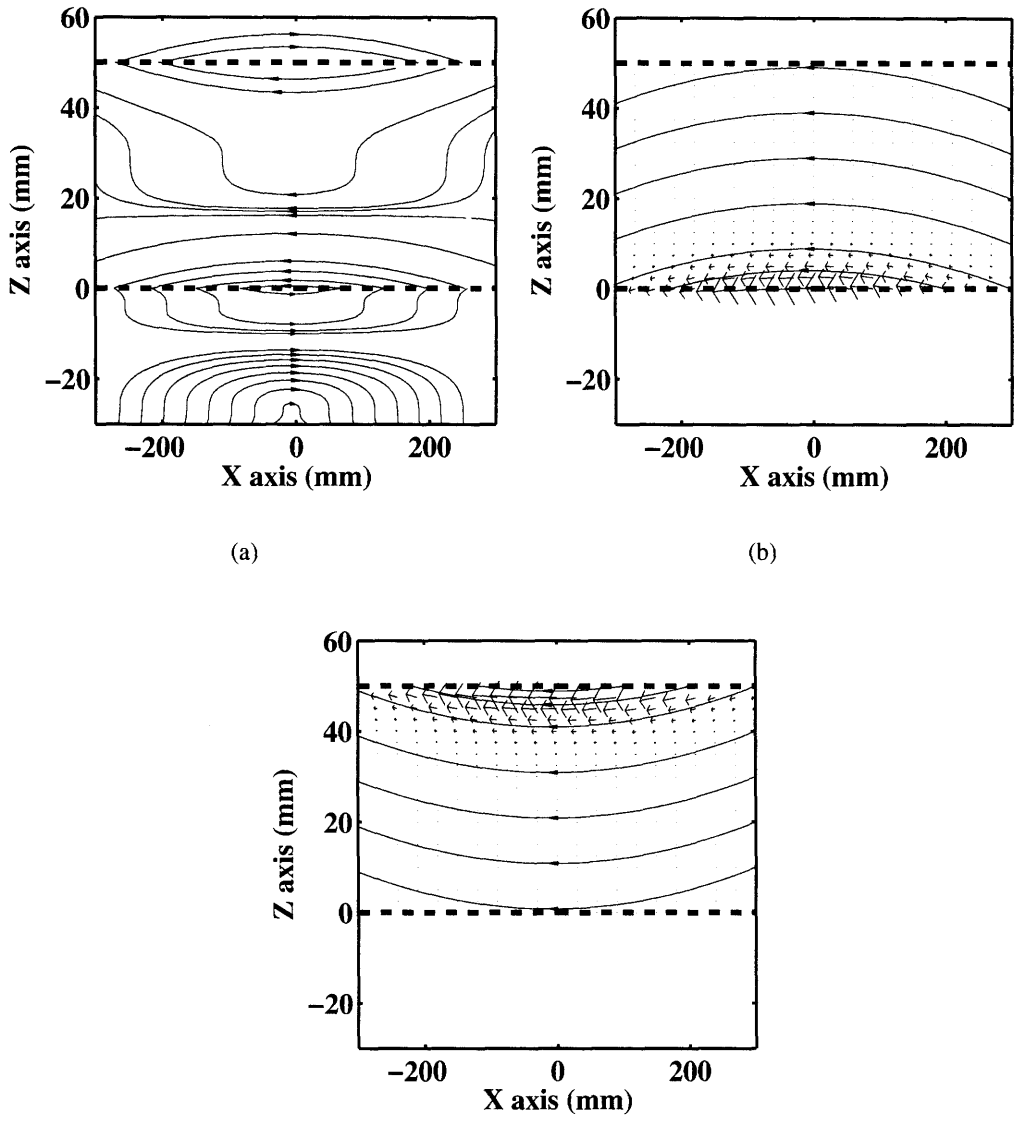

Figure 2-11: Energy flux patterns for a negative GH shift. The arrows represent the time-averaged Poynting power's magnitudes and directions. The Gaussian beam is incident at 50° from -$\hat{z}$ with its center at the origin. The beam's frequency is 10 GHz. The slab of thickness 50 mm is indicated by the dashed lines. The parameters of the three media are: $(\mu_{1r}, \epsilon_{1r}) = (1, 1)$, $(\mu_{2r}, \epsilon_{2r}) = (-0.51, -0.51)$, $(\mu_{3r}, \epsilon_{3r}) = (0.507, 0.507)$. (a)Total energy flux pattern. (b)Energy flux pattern with decaying evanescent waves only (inside the slab). (c)Energy flux pattern with growing evanescent waves only (inside the slab).

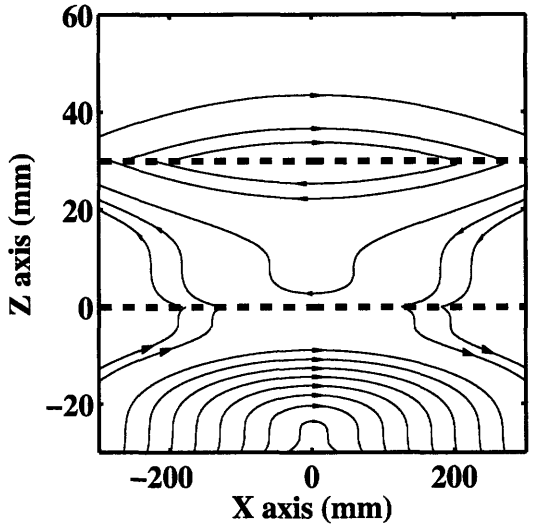

(a) Zero GH shift with a slab of 30 mm thickness.

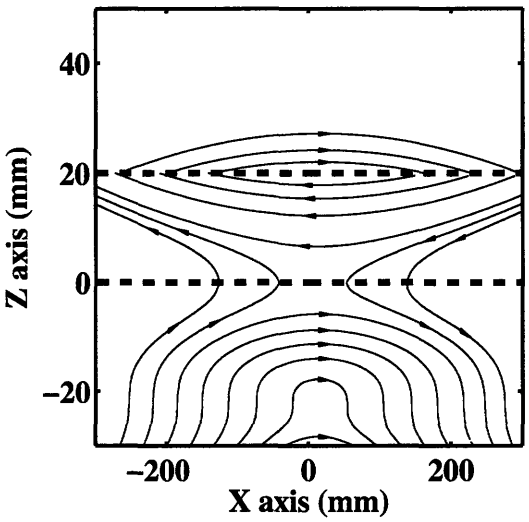

(b) Positive GH shift with a slab of 20 mm thickness.

Figure 2-12: Energy flux patterns for different GH shifts with different slab thickness. The incident beam and constitutive parameters are the same as in Fig. 2-11.

Chapter 3

Imaging Properties of LHM Slabs

3.1 Simulation of LHM Slab Imaging

3.1.1 Introduction

Since the conceptual introduction of the perfect lens imaging [14], the study of subwavelength imaging via both numerical simulations and experiments has been an active research topic. The illustration of the LHM lens can be seen from Fig.4 in [1]. As shown in Ref. [14], a perfect lens can be theoretically achieved with a left-handed material (LHM) slab perfectly matched to the surrounding right-handed material (RHM), e.g. an LHM slab with its relative permittivity and permeability both equal to -1 located in vacuum. The theoretical concept of a flat LHM slab lens was verified using the Finite-Different Time-Domain (FDTD) method in Ref. [45]. Using a similar technique, the subwavelength resolution imaging was demonstrated in Ref. [48] and the effect of finite size slab was studied in Ref. [19]. Later, the Pseudospectral Time-Domain method (PSTD) was used for the subwave-

length imaging study with one line source [16] and with two line sources [18]. In all these numerical studies, the refractive index of the LHM slabs are assumed to have a real part of exactly -1 while the imaginary part is considered to be the limiting factor for the image resolution. However, it was observed in simulations that the image resolution cannot be improved by reducing the material losses [48], which seems contradictory to the perfect lens theory. Several possible reasons, including the perturbation of the refractive index of the LHM, were mentioned in Ref. [48] without being studied in details.

The limitations of the FDTD to model a perfect LHM lens is studied, with a special emphasis on the maximum resolution that can be simulated. In order to do so, we first describe a different field averaging scheme implemented in our FDTD method. Second, an analytical formula for the constitutive parameters of the LHM material is derived and illustrates the mismatch due to the time discretization. Finally, we show that for lossless LHM slabs, the image resolution limit is mainly determined by the mismatch in the real part of the constitutive parameters, which is an inherent limiting factor in FDTD simulations.

3.1.2 FDTD Simulations

In our study, a 2D FDTD scheme is used in which we assume the non-zero fields to be E_y, H_x and H_z. The electric fields are setup at the grid centers while the magnetic fields are setup at the grid edges. A sinusoidal line source $E_y(x,z,t) = \delta(x)\delta(z)\sin(\omega_o t)f(t)$, where $f(t)$ is a smooth ramp function with a rise time of 30 wave periods, is located at (0,0) and the LHM slab is located at z=$d/2$ with a thickness of d in $\hat{z}$ and a length of L

(from $-L/2$ to $L/2$) in $\hat{x}$. The grid size is chosen initially as $\lambda/100$ where λ is the free space wavelength at the line source frequency ω_o. The size of the simulation domain is 1024 by 220 grids in $\hat{x}$ and $\hat{z}$, respectively. In order to avoid the ambiguity of studying subwavelength imaging from periodic line sources, a finite LHM slab is used instead of a infinite slab which requires periodic boundary conditions. Hence PML are used at all the boundaries to absorb the radiated fields. The length of the slab L is chosen to be 10λ for all the simulation results, and has been verified to be long enough to minimize edge effects.

The permeability μ and permittivity ϵ of the frequency dispersive LHM are both taken to obey a Drude mode, which is implemented using the Auxiliary Differential Equation (ADE) method [45] [49], where the electric and magnetic polarization currents are introduced to achieve the dispersive constitutive parameters. However, instead of setting up both discretized electric and magnetic polarization current densities at the center of grid as in Ref. [45], we keep the current densities to be aligned with the corresponding field quantities and implement a different field averaging scheme based on the integral form of the Maxwell's equations. At the LHM and air boundary, the field averaging is done by applying the integral equation:

$$\oint \overline{E} \cdot d\bar{l} = -\frac{\partial}{\partial t} \oint d\bar{s} \cdot \overline{B} - \oint d\bar{s} \cdot \overline{M} \tag{3.1}$$

where $\overline{B}$ and $\overline{M}$ are the magnetic flux and the magnetic polarization current density at the edges of the boundaries. For example, if the boundary is along $\hat{z}$, Eq. (3.1) is discretized

in the finite-difference scheme as

$$E_y^{n+1/2}(I,K) - E_y^{n+1/2}(I-1,K) = -\frac{\Delta x \mu_o}{\Delta t}[H_z^{n+1}(I,K+1/2) - H_z^n(I,K+1/2)]\frac{\Delta x}{2}M_z^{n+1/2}(I,K) \quad (3.2)$$

where I and K are the grid locations in $\hat{x}$ and $\hat{z}$, n is the time step, Δx is the grid size in x and Δt is the time step size. Reorganizing the terms, it is straightforward to obtain the update equation for H_z as

$$H_z^{n+1}(I,K) = H_z^n(I,K) - \frac{\Delta t}{2\mu_o}M_z^{n+1/2}(I,K) - \frac{\Delta t}{\Delta x \mu_o}(E_y^{n+1/2}(I,K) - E_y^{n-1/2}(I-1,K)) \quad (3.3)$$

while the update equations for E_y and H_x are left unchanged, and the update equations at other boundaries can be obtained similarly. The implementation of the above field averaging technique avoids the averaging of the polarization current on every grid inside the LHM slab and also clearly defines the material boundary.

3.1.3 LHM Material Implementation

As mentioned above, the ADE method introduces auxiliary polarization current densities to describe the dispersive constitutive parameters of the LHM slab. Typically, the frequency dispersive permittivity is implemented using the following partial differential equations:

$$\nabla \times \overline{H} = \frac{\partial}{\partial t}\epsilon_0 \overline{E} + \overline{J}_e = \frac{\partial}{\partial t}\epsilon_o \epsilon_r \overline{E} \tag{3.4}$$

$$\frac{\partial \overline{J}_e}{\partial t} + \Gamma_e \overline{J}_e = \epsilon_0 \omega_{pe}^2 \overline{E} \tag{3.5}$$

where ϵ_r is the relative permittivity, $\overline{J}_e$ is the electric polarization current, ω_{pe} and Γ_e are the electron plasma frequency and collision frequency respectively. In this study, we choose the electric plasma frequency to be the same as the magnetic one so the relative permittivity and permeability have a same value. After discretizing Eq. (3.5) and substituting J_e from Eq. (3.5) into Eq. (3.4) (see Appendix B for details), we obtain the numerical ϵ_r as:

$$\epsilon_r = 1 - \frac{\omega_{pe}^2}{4\sin(\omega_o \Delta t/2)/(\Delta t)^2} \tag{3.6}$$

It is clear that Eq. (3.6) approaches the Drude model $\epsilon_r = 1 - \omega_{pe}^2/\omega_o^2$ in the limit of $\Delta t \to 0$, which gives a value of -1 when $\omega_{pe} = \sqrt{2}\omega_o$. However, for a finite Δt used in an actual simulation, ϵ_r presents a slight deviation from exactly -1 at the same ω_{pe}. As an example, the value of ϵ_r from Eq. (3.6) is about -1.0003 for a typical grid size of $\lambda/100$, which is also the value of the refractive index since we choose here a magnetic plasma frequency identical to the electric one. This small perturbation does not affect the propagating waves significantly. However, the resolution of a subwavelength imaging system is critically dependent on the reconstruction of the evanescent waves, or part of the evanescent wave spectrum, by the LHM slab. This reconstruction is in turn critically dependent on the slab's constitutive parameters [15], and the slight mismatch of 0.03% in the real part has

an important impact on the resolution of the image as we shall see hereafter. It is important to note that this small perturbation in the real part of the constitutive parameters has often been overlooked and the imaginary parts with a value in the same order are typically considered to be the main contributor for limiting the image resolution.

3.1.4 Numerical Examples

To further illustrate the influence of the perturbed material properties on the image resolution in simulations, a lossless LHM slab with a thickness $d = 0.2\lambda$ is used to image a line source located at $d/2$ away from its interface. The analytical calculation is carried out using the method outlined in Ref. [50] for an infinite slab with μ_r and ϵ_r equal to -1.0003. The calculated and simulated electric field magnitudes at the image plane (located at $z = 2d$) are compared and the results are shown in Fig. 3-1. It can be seen that both results have a similar peak profile, which indicates that the image resolution computed from the simulation is in agreement with the one predicted analytically. The small differences between the results away from the main peak can be attributed to the difference between the infinite slab used in the analytical calculation and the finite slab used in the simulation. However, these differences have a negligible effect on the image resolution. In addition, it is clear that because of the introduced mismatch, both results differ from the electric field magnitude of a perfect image, which has an infinitely small width of the peak.

The imaging ability of the LHM slab can also be quantified by looking at the spectrum representation of the fields at the image plane. This is shown in Fig. 3-2 where the normalized spectrum of the simulated electric field of Fig. 3-1 is compared with the spectrum

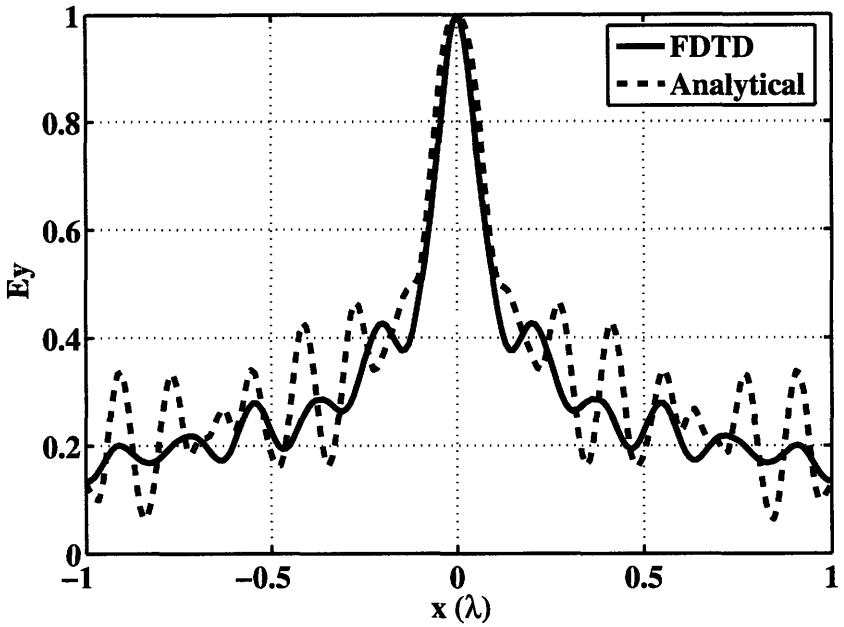

Figure 3-1: Comparison of $|E_y|$ at the image plane from the FDTD simulation and the analytical calculation for an LHM slab with a thickness of 0.2λ. The grid size used in the simulation is $\lambda/100$. The analytical calculation considers an LHM slab of $\mu_r = \epsilon_r = -1.0003$ in vacuum.

obtained analytically (by plotting the transmission coefficient of the LHM slab from the source plane to the image plane). The two spectra extend up to around $7k_o$ before the cut-off, which suggest that the resolution of the image is about $\lambda_o/7$. In addition, it can be seen that the two spectra agree well both qualitatively and quantitatively, which confirms that the analytical calculations using the mismatched values predict the image resolution obtained from the simulation. The sharp peak in the analytical spectrum due to the singularity of the pole from the LHM slab's transmission coefficient [9], [42], [50] is well predicted in the simulated spectrum.

It is known that the image resolution is determined by the maximum transverse wave number (maximum k_x) that can be restored at the image plane, and it was pointed out in Ref. [50] that the image resolution is related to the location of the pole in the transverse

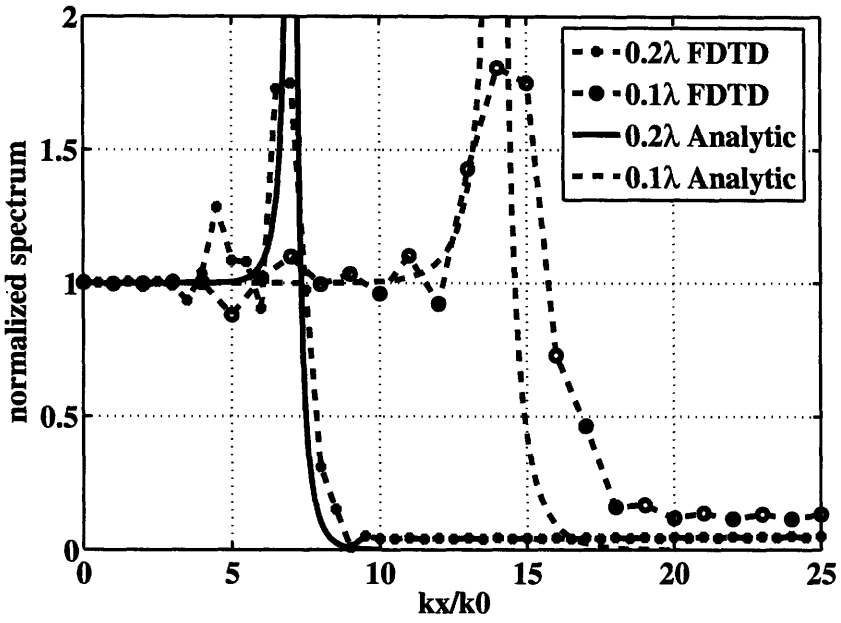

Figure 3-2: Comparison of E_y spectra at the image plane from the FDTD simulations and the analytical calculations for two slab configurations: one with a thickness of 0.2λ and the other with a thickness of 0.1λ. Both slabs are simulated with a same grid size of $\lambda/100$.

wavenumber spectrum. From Fig. 3-2, it is shown that the maximum restored transverse wave numbers are close to the location of the singularity, which again confirms the observation in Ref. [50]. In addition, Fig. 3-2 shows the same comparison study for a slab thickness of $d = 0.1\lambda$. Again, the analytical and simulated spectra are in good agreement with the image spectrum which extends to about $14k_o$. The comparison between the results from these two slab thicknesses show that the image resolution is approximately improved by a factor two when the LHM slab thickness is reduced by one half, which is consistent with the theoretical prediction [15][50].

The subwavelength resolution of the LHM slab can be directly visualized by considering the case of two line sources separated by 0.2λ and located 0.1λ away from the slab

interface. The time-averaged Poynting power densities at the image plane from the simulations and analytical calculations are compared in Fig. 3-3, where the two peaks are clearly recognizable and the features agree well between simulation and the analytical calculation. The results from the above study suggest that the simulated resolution in FDTD is limited mainly by the mismatch between the real part of constitutive parameters of the LHM slabs and the ones of the surrounding vacuum.

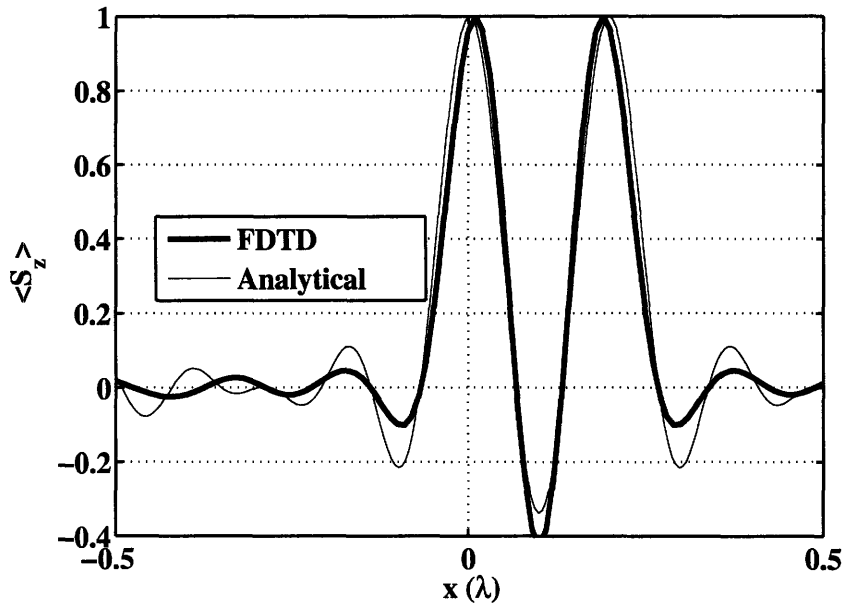

Figure 3-3: Comparison of time averaged Poynting power densities $< S_z >$ at the image plane from the FDTD simulation and the analytical calculation for the two line source imaging. The LHM slab is the same as in Fig. 3-1. The line sources are separated by 0.2λ.

According to Eq. (3.6), the accuracy of ϵ_r is related to the time step size rather than the grid size. To illustrate this, the LHM slab used in Fig. 3-1 is simulated again using a different grid size while keeping the same time step size. The results are shown in Fig. 3-4 where two grid sizes are used, namely $\lambda/200$ and $\lambda/100$, but with an identical time step size. The resolution limits from these two results are almost identical and both are improved slightly (from $7k_o$ to about $7.5k_o$) from the resolution shown in Fig. 3-2 due to the reduction

of time step size.

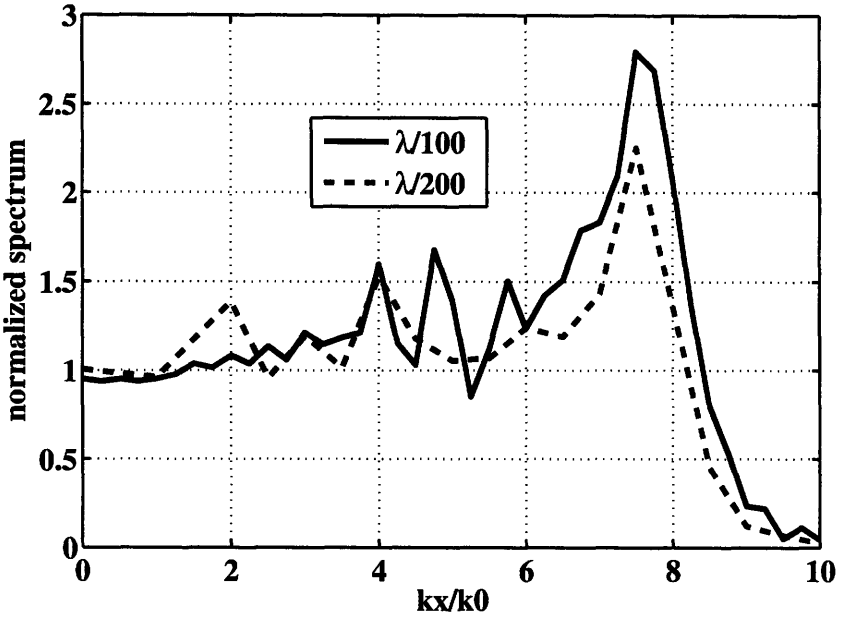

Figure 3-4: Comparison of E_y spectrum at the image plane from the FDTD simulations using different grid sizes. The time step size is calculated from Courant's criterion based on the grid size of $\lambda/200$ and is adopted for the simulation using the grid size of $\lambda/100$ as well. The LHM slab is the same as in Fig. 3-1.

3.1.5 Summary

A study of the LHM slab's constitutive parameters in the FDTD implementation is presented. It is shown that there exist a mismatch between the slab and its surrounding medium due to the time discretization rather than space discretization. By comparing the simulation results and analytical calculations, we demonstrate that the simulated image resolution of an LHM perfect lens is mainly limited by this mismatch. In other applications such as the simulation study of surface plaritons at LHM/RHM interfaces where the matching condition is required, the understanding of this limitation in FDTD can also be very important.

3.2 Imaging Properties of Finite LHM Slabs

3.2.1 Introduction

In practical systems [5] [21] the slab's size is finite. However, there have been only a few studies, either theoretically, numerically or experimentally, on the effect of the finiteness of the LHM slabs on the resolution power of the lens. Among the properties of the finite-size slabs people have come to know, an interesting one is that the image quality is not sensitive to the size of the finite slab [5], which is contrary to the properties of a conventional lens. In addition, a peculiar property that negative energy streams can appear at the image plane with finite-size slab was discovered [19]. Yet, no satisfactory explanations of these properties have been reported in the literature. We address this need by analyzing these properties using analytical methods combined with numerical simulations, which allow us to provide a series of physical explanations to the imaging properties of finite-size LHM slabs. First, The equivalent current sheet method from Huygens' principle is applied to study the imaging capability of the finite-size slabs. The main features in the image spectrum due to the slab's finite length are explained by considering the changes in fields at the LHM slab boundary. Next, the energy stream at the image plane is investigated by decomposing a line source into plane waves, *i.e.* propagating and evanescent waves, and evaluating the energy contributions from the wave interactions. In doing so, we show that the negative energy stream is a not only a property of finite-size LHM slabs but also a property of infinite LHM slabs.

3.2.2 Image Spectrum In the Finite LHM Slab Imaging system

In order to evaluate an imaging system, the knowledge of image spectrum is important. For an infinite LHM slab, the image spectrum can be obtained analytically, therefore the resolution can be found readily by locating the maximum wavenumber in the spectrum. When the LHM slabs become finite, it has been found that the image resolution is not affected noticeably, although the image spectrum has changed [5]. In the first part, we analyze how the image spectrum changes with the slab's length and how the maximum wavenumber is affected, thus providing an explanation to the observation reported in [5]. Since a finite size slab does not have a geometry that can define a coordinate system in which the Maxwell's equations can be easily expanded (*e.g.* like spheres, cylinders etc), we resort to an approximation method which consists in studying the electric and magnetic fields at the slab's second boundary (image side) instead. From Huygens' principle, the fields at the slab's boundary can be converted into equivalent current sheets which can in turn be used to find the fields at the image plane. By observing the fields at the slab boundary, the changes in the image fields can be found, and subsequently the spectrum can be determined.

We shall first start with an infinite slab. The setup of the LHM slab imaging system is shown in Fig. 3-5: a line source (infinite in $\hat{y}$) is placed at $x = d_1$ in the x-z plane; a slab along $\hat{z}$ with thickness d_s is located between the coordinates $x = 0$ and $x = d_2 = -d_s$. For simplicity, we choose $d_1 = -3d_s/2$ so that the image plane is at $x = d_3 = d_s/2$. The length L depicted in Fig. 3-5 is infinite in this case.

The electric fields from a line source can be expressed in the plane wave representation

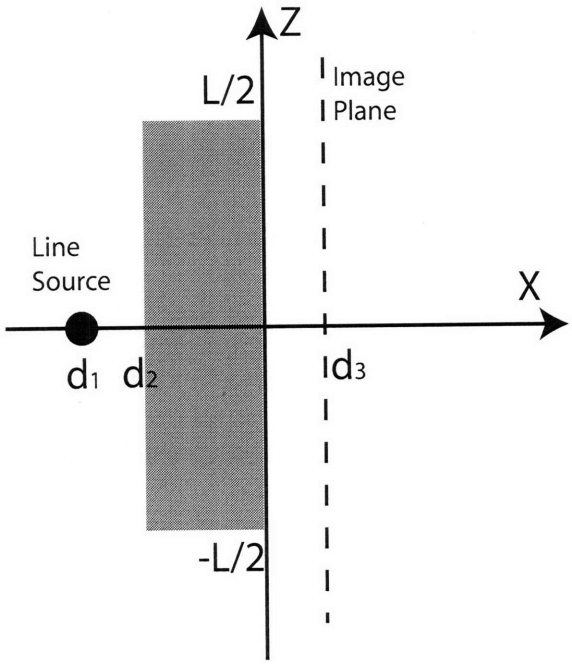

Figure 3-5: Geometry of the LHM slab imaging system.

as

$$\overline{E}_{ln}(x,z) = \hat{y}\frac{-\omega\mu_o}{4}H_0^{(1)}(k_o|\rho-\rho'|) = \hat{y}\frac{-\omega\mu_o}{4\pi}\int_{-\infty}^{\infty}\mathrm{d}k_z\frac{1}{k_x}e^{ik_x(x-d_1)}e^{ik_z z} \tag{3.7}$$

After the transmission through the slab, the tangential fields at the slab's second boundary are

$$E_y(z) = \frac{-\omega\mu_o}{4\pi}\int_{-\infty}^{\infty}\mathrm{d}k_z\frac{T(k_z)}{k_x}e^{-ik_x d_1}e^{ik_z z} \tag{3.8}$$

$$H_z(z) = \frac{-1}{4\pi}\int_{-\infty}^{\infty}\mathrm{d}k_z T(k_z)e^{-ik_x d_1}e^{ik_z z} \tag{3.9}$$

where $T(k_z)$ is the transmission coefficient of the slab, $k_o^2 = k_x^2 + k_z^2 = \omega^2\mu_o\epsilon_o$ is the free space wave vector. The fields at the image plane are then obtained from those at the slab boundary. Applying Stratton-Chu formula [42], the field beyond the slab's boundary

$(x > 0)$ can be written as:

$$\begin{aligned}\overline{E}(x,z) &= \int_{z'} \mathrm{d}z' \left\{ i\omega\mu_o[\hat{n} \times \overline{H}(\overline{r}')]g(\overline{r},\overline{r}') \right. \\ &\left. +[\hat{n} \cdot \overline{E}(\overline{r}')]\nabla' g(\overline{r},\overline{r}') + [\hat{n} \times \overline{E}(\overline{r}')] \times \nabla' g(\overline{r},\overline{r}') \right\} \qquad (3.10)\end{aligned}$$

where the usual surface integral has been replaced by a line integral along $\hat{z}$ because of the invariance of the geometry along $\hat{y}$. $\overline{E}(\overline{r}'), \overline{H}(\overline{r}')$ are the fields at the slab's second boundary which are expressed in Eq. (3.8) and Eq. (3.9), $\hat{n} = \hat{x}$ is the normal of the boundary. The Green's function is $g(\overline{r},\overline{r}') = (i/4)H_0^{(1)}(k_o|\overline{\rho}-\overline{\rho}'|)$ and the integration is along z. Plugging in the expression of the fields, we find

$$\begin{aligned}\overline{E}(x,z) &= \hat{y}\int_{-\infty}^{\infty} \mathrm{d}z' \frac{i\omega\mu_o}{4\pi} \int_{-\infty}^{\infty} \mathrm{d}k_z T(k_z) e^{-ik_x d_1} e^{ik_z z'} \\ &\quad \frac{i}{4} H_0^{(1)}(k_o\sqrt{(z-z')^2+x^2}) \\ &+ \hat{y}\int_{-\infty}^{\infty} \mathrm{d}z' \frac{-\omega\mu_o}{4\pi} \int_{-\infty}^{\infty} \mathrm{d}k_z \frac{T(k_z)}{k_x} e^{-ik_x d_1} e^{ik_z z'} \\ &\quad \frac{\partial}{\partial x'} \frac{i}{4} H_0^{(1)}(k_o\sqrt{(z-z')^2+(x-x')^2})|_{x'=0} \\ &= \hat{y}E_1 + \hat{y}E_2 \qquad (3.11)\end{aligned}$$

where E_1 and E_2 are the two integrals respectively. It is straightforward to show that $E_1 = E_2$, indicating that the fields generated from the electric current sheet are the same as the ones from the magnetic current sheet. Finally, the spectrum of the image is obtained

by applying the inverse Fourier transform of $E(x = d_3, z)$, from which we get

$$\begin{aligned} E(k_z) &= \int_{-\infty}^{\infty} \mathrm{d}z \, 2E_1(x = d_3, z) e^{-ik_z z} \\ &= \frac{-\omega\mu_o}{4\pi} \frac{e^{ik_x d_3}}{k_x} T(k_z) e^{-ik_x d_1} \qquad (3.12) \\ &= \frac{-\omega\mu_o}{4\pi} \frac{e^{ik_x d_3}}{k_x} T_1(k_z) \qquad (3.13) \end{aligned}$$

where $T_1(k_z) = T(k_z)\exp(-ik_x d_1)$. It can be seen that the spectrum of the image can be interpreted as the spectrum of the line source multiplied by the slab's transmission coefficient with a phase propagation term.

With the procedure established for the infinite slab, we purse with the study of the finite size slab. For the general discussion, we write the field equation at the finite slab boundary as

$$\overline{E}_f(z) = \hat{y} \frac{-\omega\mu_o}{4\pi} f(z) \int_{-\infty}^{\infty} \mathrm{d}k_z \frac{T(k_z)}{k_x} e^{-ik_x d_1} e^{ik_z z} \qquad (3.14)$$

where the function $f(z)$ represents the change in the field due to the finite size when compared to the infinite slab case. In what follows, we make the approximation $f(z) = 0$ for $z < -L/2$ or $z > L/2$, which indicates that the current sheet can be viewed as from an aperture of size equal to the size of the slab.

This assumption has been validated by observations from numerical simulations which show that the fields at the slab's boundary are much stronger than the fields in free space. As an example, we consider a slab of thickness d_s = 0.2 λ and of length L = 2 λ, which yields an aspect ratio similar to those used in practical applications. In Fig. 3-6, we com-

pare the fields at the image plane from the full wave numerical simulation and the fields calculated using the equivalent currents from only the fields at the slab's boundary (*i.e.* with the finite aperture effect). It is evident that the contributions from only the fields at the slab's boundary is almost equivalent to the contribution of the total field. The difference in the peak magnitudes does not affect the image resolution since the 3 dB width of the fields from both results are very close.

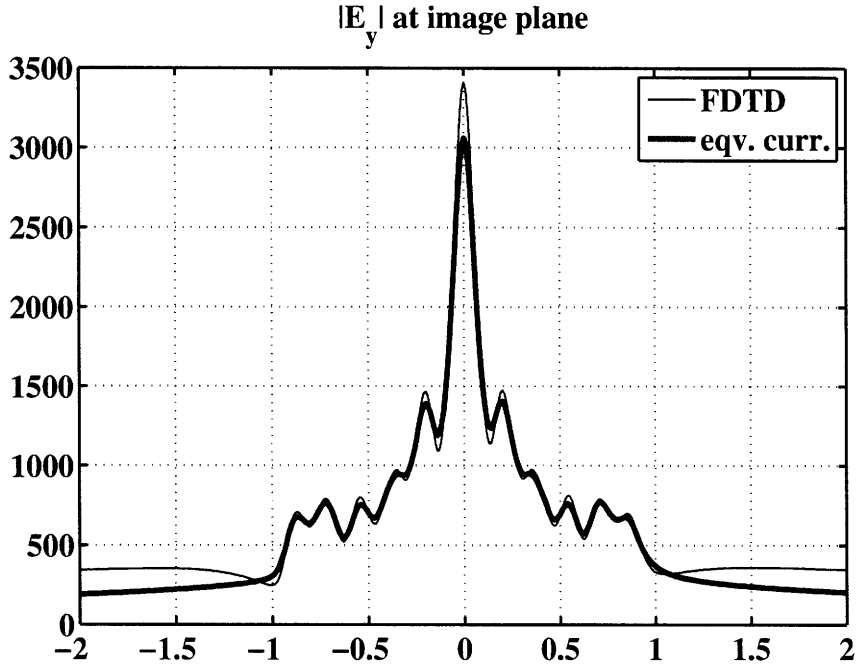

Figure 3-6: E field at the image plane approximated by the current sheet compared with E field from FDTD (without approximation). The current sheet is from only the aperture of the finite slab. The slab has thickness $d_s = 0.2\lambda$ and a length of $L = 2\lambda$. The property of the slab is $\mu_r = \epsilon_r = -1.0003$. It can be seen that the current sheet method is a valid approximation method for estimating the fields at image plane.

Following the same procedure as those used to obtain Eq. (3.11), the electric field at the

image plane ($x = d_3$) is obtained as

$$E(z) = \frac{-\omega\mu_o}{8\pi^2}\int_{-\infty}^{\infty} \mathrm{d}k_z' T(k_z') e^{-ik_x' d_1} \int_{-\infty}^{\infty} \mathrm{d}k_z'' \frac{e^{ik_x'' d_3}}{k_x''} e^{ik_z'' z} F(k_z' - k_z'') \quad (3.15)$$

where $F(k_z)$ is the Fourier transform of $f(z)$. The spectrum of the electric field at the image plane can be evaluated as

$$\begin{aligned} E(k_z) &= \frac{-\omega\mu_o}{8\pi^2}\int_{-\infty}^{\infty} \mathrm{d}k_z' T(k_z') e^{-ik_x' d_1} \int_{-\infty}^{\infty} \mathrm{d}k_z'' \frac{e^{ik_x'' d_3}}{k_x''} F(k_z' - k_z'') 2\pi\delta(k_z'' - k_z) \\ &= \frac{-\omega\mu_o}{4\pi}\frac{e^{ik_x d_3}}{k_x}\int_{-\infty}^{\infty} \mathrm{d}k_z' T(k_z') e^{-ik_x' d_1} F(k_z' - k_z) \\ &= \frac{-\omega\mu_o}{4\pi}\frac{e^{ik_x d_3}}{k_x}\{T_1(k_z) \otimes F(k_z)\} \end{aligned} \quad (3.16)$$

where the $\otimes$ is the convolution operator. Detailed derivations of above equations can be seen in Appendix C. Eq. (3.16) indicates that the image spectrum from a finite-size slab can be approximated by the convolution of the transmission coefficient and the Fourier transform of $f(z)$ multiplied by the line source spectrum. Since the image resolution is closely tied to the spectrum, Eq. (3.16) is also useful for the study of image resolution. The next important step is to determine what function to be used for $f(z)$.

Since $f(z)$ relates to the field changes at the slab's boundary, we plot in Fig. 3-7 and Fig. 3-8 the electric field's amplitude and phase at the boundary from the infinite slab and the finite slab, respectively. The field from the infinite slab is obtained by evaluating Eq. (3.8) while the field from the finite slab is obtained by numerical simulation using FDTD. Both slabs have a thickness d_s = 0.2λ and the finite slab has a length of L =2 λ.

In choosing the material properties for the infinite slab, we make use of our previous effort [20] which points out the inherent mismatch in material due to the finite discretization in FDTD for implementing a frequency dispersive model (e.g. Drude model). Hence we use $\mu_r = \epsilon_r = -1.0003$ for the slab which is equivalent to the LHM slab implemented in FDTD using $\Delta = \lambda/100$ and the corresponding time step.

Examining both amplitudes in Fig. 3-7 and Fig. 3-8, one can observe that in the case of the finite slab, the fields taper off at the edge of the slab while in the case of infinite slab the fields maintain a constant but small oscillation. Checking the phase of these two cases, one can realize that the phases are almost identical within the slab's length. This is not a coincidence. In the case of the infinite slab, studies [50] show that the field at the slab's boundary is dominated by the contribution from the pole in the transmission coefficient $T(k_z)$ as the result of the contour integration in the complex plane for Eq. (3.8). The wavenumber where the pole occurs approximately corresponds to the resolution of the slab . Since the pole contributes to a single dominating surface wave propagating at the slab boundary, the phase of the field is determined by this surface wave mode. In the case of the finite slab, the contribution from the pole is still significant at the boundary so that the phase propagation remains almost the same. By taking the ratio of the fields, one can find the exact function for $f(z)$, which is shown in Fig. 3-9 for both the amplitude and the phase. In the region of the slab's length, the tapering amplitude and near zero phase can be readily seen. In addition, we can obtain the image spectra (normalized to the line source spectrum) from both slabs, and the comparison is shown in Fig. 3-10. We see that the position of the main peak (due to the pole) remains unchanged except for a smaller ampli-

tude in the finite slab case. Furthermore, there are oscillations in the band for the finite slab.

In order to understand these changes in the spectrum, we shall now proceed with the approximation of $f(z)$. This is a necessary step to reveal the physical interpretation of the finite slab's image spectrum. Based on the above discussion, we propose to approximate $f(z)$ as a real function with Gaussian tapered amplitude $\exp(-z^2/g^2)$ but truncated at the slab boundary. The plot of the approximated $f(z)$ is shown by the dash line in Fig. 3-9. After the approximation, Eq. (3.16) can be used to evaluate the image spectrum without the aid of numerical simulation. The proposed $f(z)$ approximation has two features, *i.e.* a Gaussian amplitude and a truncation at the slab's edge. We study the effect of these features independently. Fig. 3-11 shows the image spectrum with $f(z)$ as a Gaussian function with and without the truncation. Compared with the spectrum from the infinite slab, the Gaussian approximation produces the same shape with a lower peak amplitude and wider peak width. This is well expected as the consequence of convolution operation with a Gaussian function. Notice that no oscillations is introduced into the spectrum. With $f(z)$ approximated as truncated Gaussian function, the spectrum exhibits additional oscillations in the spectrum as shown in the figure and the periodicity agrees with the one obtained from the simulations (Fig. 3-8). It can therefore be concluded that the periodicity comes from the length of the slab. The differences in amplitudes between the approximated spectrum and the actual one are due to the simplification of the actual $f(z)$. However these differences do not prevent us from observing the main features in the image spectrum. By reducing the length of the slab from infinite to finite, the image spectrum is changed with a lower main peak amplitude and an oscillation within the band. But these changes do not reduce

the maximum wavenumber in the image spectrum. Hence the size of the LHM slabs has little effect on the image resolution. The experimental observation that subwavelength imaging can be achieved by small size slabs and that increasing the slab's size does not make significant improvements in the image resolution [21] is thus explained.

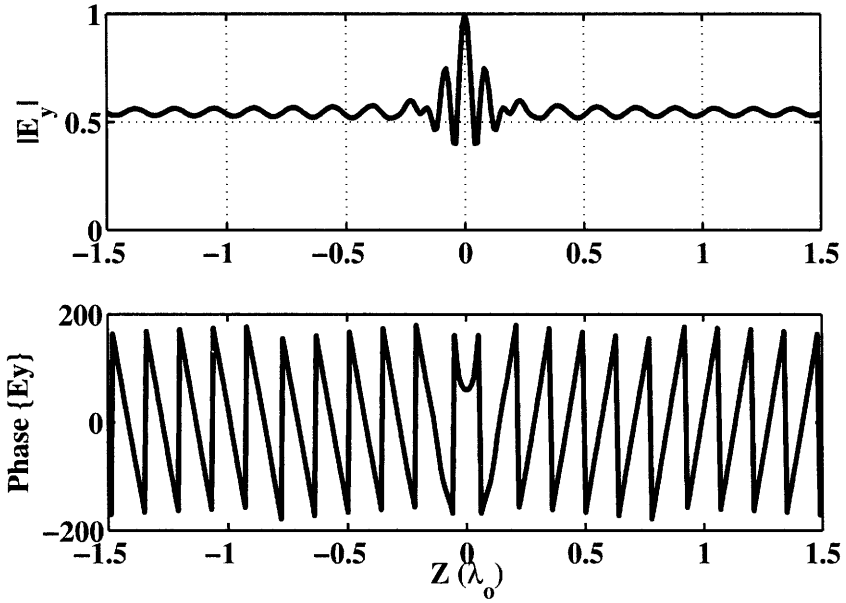

Figure 3-7: Amplitude and phase of E field at the infinite slab boundary. The slab has a thickness of $d_s = 0.2\lambda$.

3.2.3 Negative Energy In the LHM Slab Imaging

In addition to the property of preserving the image resolution as discussed in the previous section, another unique property reported with LHM slabs is the negative energy stream at the image plane. This property has been emphasized in the case of finite slabs in [19]. For a conventional lens imaging system, the energy at the image plane is always in the positive direction, *i.e.* in the propagating direction of the waves emitted from the source. For LHM flat lens imaging systems, however, there exist regions at the image plane where the energy

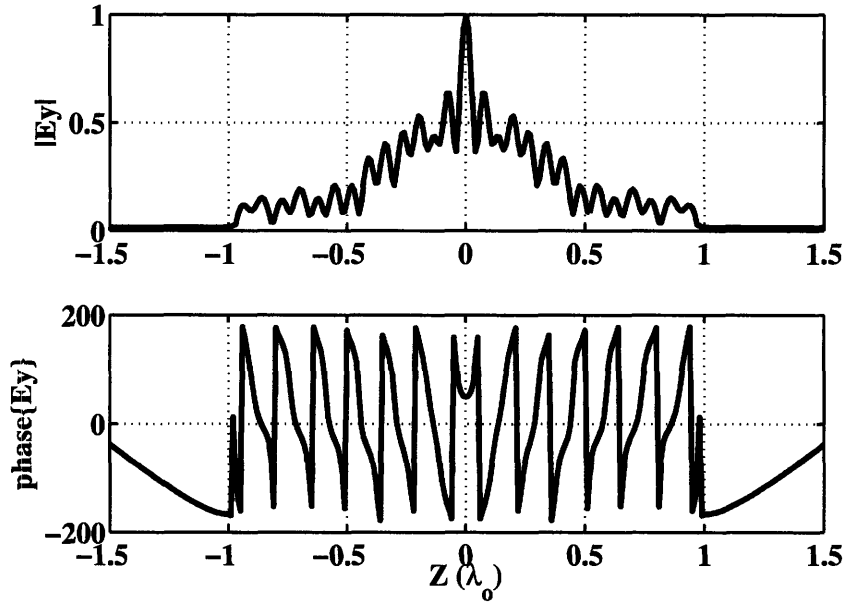

Figure 3-8: Amplitude and phase of E field at the finite slab boundary. The slab has a thickness of $d_s = 0.2\lambda$ and a length of $L = 2\lambda$.

streams are in the negative direction, even though the energy is positive at the focal point. We show here that not only this phenomenon is not peculiar but also it is still present in the case of infinite slabs. In order to facilitate the discussion, we shall analyze the infinite slab case first, then continue on discussing the case of the finite LHM slabs.

Eq. (3.7) shows that a line source consists of propagating waves as well as evanescent waves. It is also known that each individual propagating wave carries power in the forward direction after transmitting through the slab, while evanescent waves carry no power in the forward direction. Therefore it is obvious that the negative energy stream cannot be explained by just considering each individual wave component. Considering the interactions between the waves, there exist three different cases of interaction (i) interaction between propagating waves, (ii) between evanescent waves, (iii) between propagating and evanescent waves.

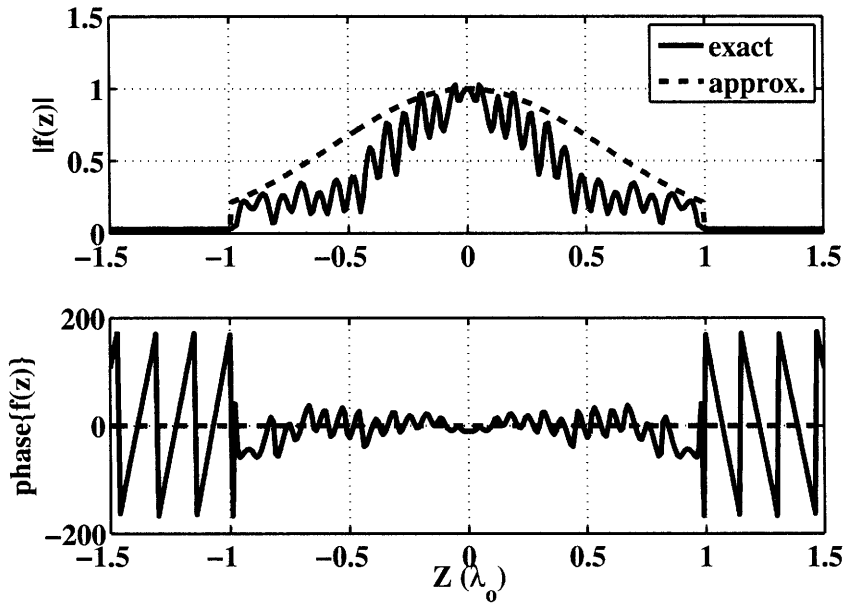

Figure 3-9: Amplitude and phase of function f(z). The exact f(z) is from FDTD simulation, and the approximated f(z) is a truncated Gaussian function.

For the first case, taking two propagating waves (TE polarized) as $E_{y\eta} = E_o \exp\{ik_{x\eta}x + ik_{z\eta}z\}$, where $\eta = a, b$ for the two waves and $k_\eta^2 = k_{x\eta}^2 + k_{z\eta}^2 = \omega^2\mu_1\epsilon_1$, the total time-averaged Poynting power in $\hat{x}$, which is the forward direction of the imaging system, can be written as:

$$\langle S_x \rangle = \frac{1}{2}E_o^2 \left\{ \left(\frac{k_{xa}}{\omega\mu_1} + \frac{k_{xb}}{\omega\mu_1}\right)\left(1 + \cos[(k_{xa} - k_{xb})x + (k_{za} - k_{zb})z]\right) \right\} \tag{3.17}$$

where $\langle . \rangle$ indicates the time average. It is clear that $\langle S_x \rangle > 0$ which means that the interactions between propagating waves always contribute to a positive power. For the second case, taking two evanescent waves with $E_{y\eta} = \exp\{ik_{z\eta}z - \alpha_{x\eta}x\}$, we get

$$\langle S_x \rangle = \sin[(k_{za} - k_{zb})z] e^{-(\alpha_{za} + \alpha_{zb})z} \left(\frac{\alpha_{xa}}{\omega\mu_1} - \frac{\alpha_{xb}}{\omega\mu_1}\right) \tag{3.18}$$

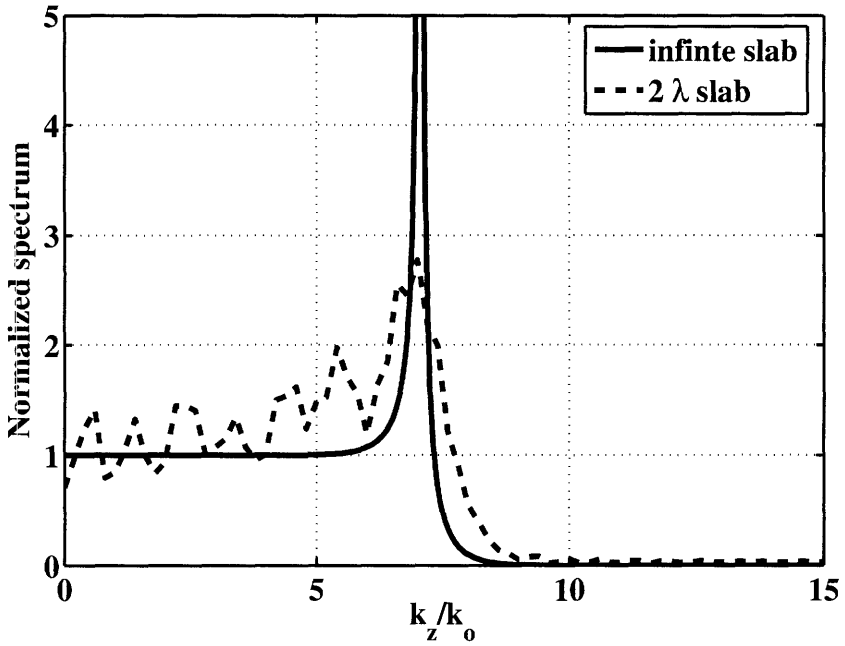

Figure 3-10: Spectrum of the E field at the image plane from an infinite slab and a finite slab. In both cases, slabs have a thickness of $d_s = 0.2\lambda$. The finite slab s has a length of $L = 2\lambda$. The spectrum is normalized to the line source spectrum.

In such case, the power density $\langle S_x \rangle$ decays exponentially in $\hat{x}$ but oscillates between positive and negative values along $\hat{z}$ due to the sinusoidal function. Although this might seem to be the reason for the negative energy stream to appear at the image plane, this is still not the case upon considering the contributions from all the evanescent waves from a line source, we find that no negative power is generated at the image plane. In order to see this, we take the field at the image plane (same as Eq. (3.8) and Eq. (3.9) with an extra $\exp(-i2k_x d_1)$ term in the integrand), and consider only the evanescent waves. Taking advantage of k_x being an even function of k_z, we write the fields produced by the evanescent waves only

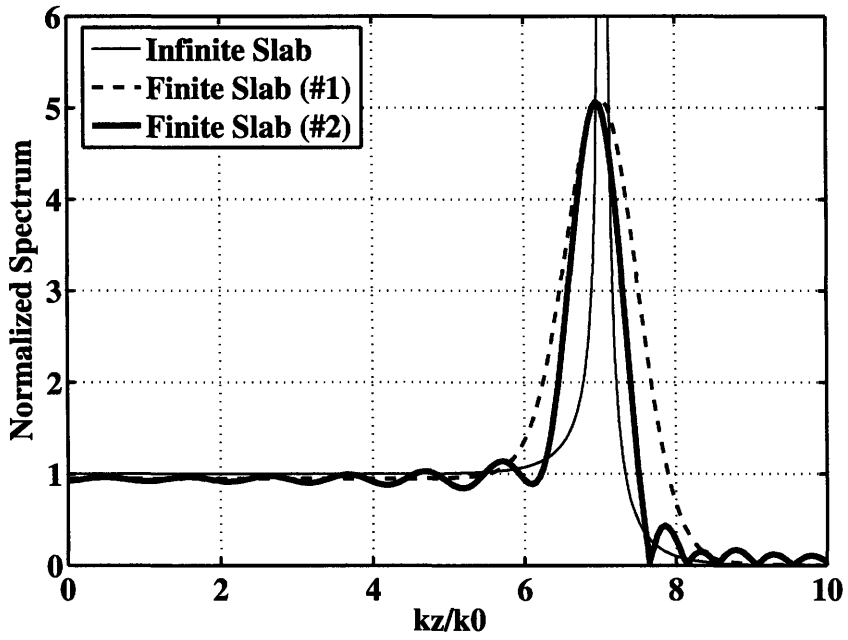

Figure 3-11: Spectrum of E field at the image plane from an infinite slab and the approximated spectrum from a finite slab. The slabs are the same as in Fig. 3-10. Approximation method #1 is to use the Gaussian function for the current sheet. Method #2 is to used the Gaussian function truncated to the slab aperture.

as:

$$E_{y,evan}(z) = \frac{-\omega\mu_o}{2\pi}\int_{k_o}^{\infty} \mathrm{d}k_z \frac{T(k_x)}{k_x} e^{i2k_x(d_2-d_1)} \cos k_z z \tag{3.19}$$

$$H_{z,evan}(z) = \frac{-1}{2\pi}\int_{k_o}^{\infty} \mathrm{d}k_z T(k_x) e^{i2k_x(d_2-d_1)} \cos k_z z \tag{3.20}$$

For $k_z > k_o$, we have k_x=$\sqrt{(k_o^2 - k_z^2)}$=$i\alpha_x$. Therefore, the term $T(k_x)e^{i2k_x(d_2-d_1)} \cos k_z z$ is real. Hence, $E_{y,evan}(z)$ is purely imaginary while $H_{z,evan}(z)$ is purely real, yielding no real power. A different way to see this is to examine Eq. (3.18) and to note that $\langle S_x \rangle$ is an odd function of $(k_{za} - k_{zb})$. After integrating over the symmetric spectrum of a line source, the integration of an odd function becomes zero.

The last case that remains to be considered is the interaction between evanescent waves

and propagating waves. Again, starting from two waves with E_{ya} as a propagating wave and E_{yb} as an evanescent wave, the power along $\hat{x}$ is

$$\begin{aligned}\langle S_x \rangle &= (1/2)\left\{\frac{k_{xa}}{\omega\mu_1} + \frac{k_{xa}}{\omega\mu_1}\exp\{-\alpha_{xb}x\}\cos[(k_{za}-k_{zb})z + k_{xa}x]\right. \\ &\left. + \frac{\alpha_{xb}}{\omega\mu_1}\exp\{-\alpha_{xb}x\}\sin[(k_{za}-k_{zb})z + k_{xa}x]\right\} \end{aligned} \tag{3.21}$$

which is no longer a simple odd function of $(k_{za} - k_{zb})$ as in Eq. (3.18). In addition, it can be seen that $\langle S_x \rangle$ can have negative values if $\exp(-\alpha_{xb}x)$ is compensated by the evanescent wave amplitude, which is made possible by LHM slabs. As a matter of fact, one of the interesting properties of LHM is to precisely to amplify evanescent waves. For the purpose of illustration, we setup an incident propagating wave and an evanescent wave at the line source location (Fig. 3-12), both with unit amplitude, to observe the power at the image plane. The wavevector in $\hat{z}$ for the propagating wave is $k_{za} = 0.5k_o$ (where k_o is the free space wavenumber), while the one for the evanescent wave is $k_{zb} = 3k_o$. The fields of the slab configuration are solved analytically, and the amplitude of E_y is shown in Fig. 3-12(a). At the slab's second boundary, large E_y amplitudes can be observed, which is due to the evanescent wave amplification inside the LHM slab. The oscillation in the field amplitude can be seen with a periodicity slightly greater than $\lambda/3$ which is close to the difference in the wavenumbers of the two incident waves. Fig. 3-12(b) shows a zoom-in view of the field and the time-averaged Poynting vectors in one spatial period along the z axis. Together with the field amplitude oscillations, the Poynting power is also oscillating between positive and negative value in $\hat{x}$. Therefore, Fig. 3-12 illustrates that negative Poynting power can be obtained by the interactions between a propagating and an evanes-

cent wave.

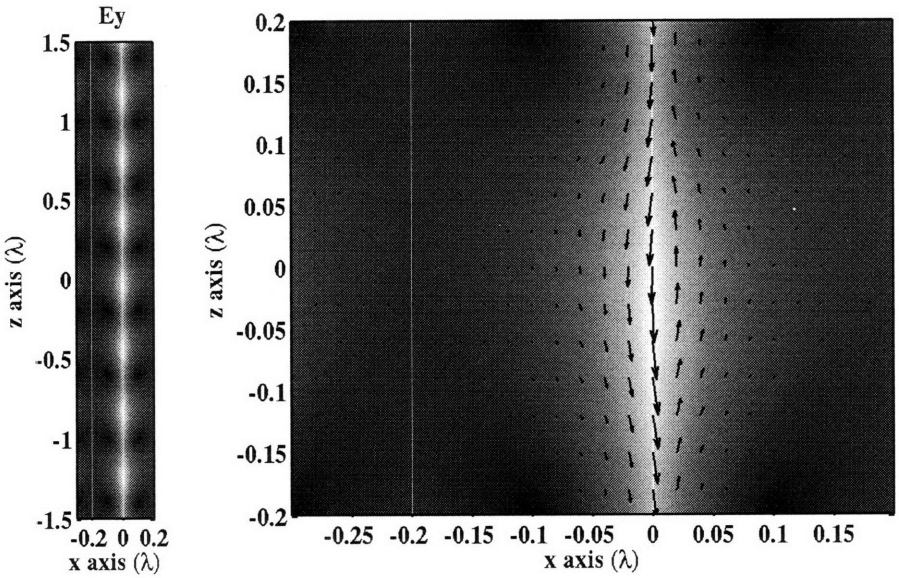

(a) field pattern

(b) field and energy flux pattern (zoomed in)

Figure 3-12: Field and energy flux pattern of the interaction between a propagating wave and an evanescent wave from a LHM slab. The slab with a thickness of 0.2λ is between the white lines . The incident wave front is at 0.1λ in front of the slab. The plot shows that the negative energy flux exist near the slab's second boundary after the evanescent wave is amplified by the LHM slab.

Further validation can be done in the case of a line source. The time-averaged Poynting power at the image plane from an infinite slab (d_s = 0.2 λ) is shown in Fig. 3-13(a). It can be seen that away from the central peak, the power oscillates between positive and negative values with a decaying amplitude. Decomposing the fields into propagating and evanescent waves, the contributions due to wave interactions can be evaluated, as it is shown in Fig. 3-13(b). As expected, the propagating waves only contribute to the power in the positive

direction, while the negative energy stream comes from the interactions between propagating and evanescent waves. It also shows that the power due to the interaction of evanescent waves is zero.

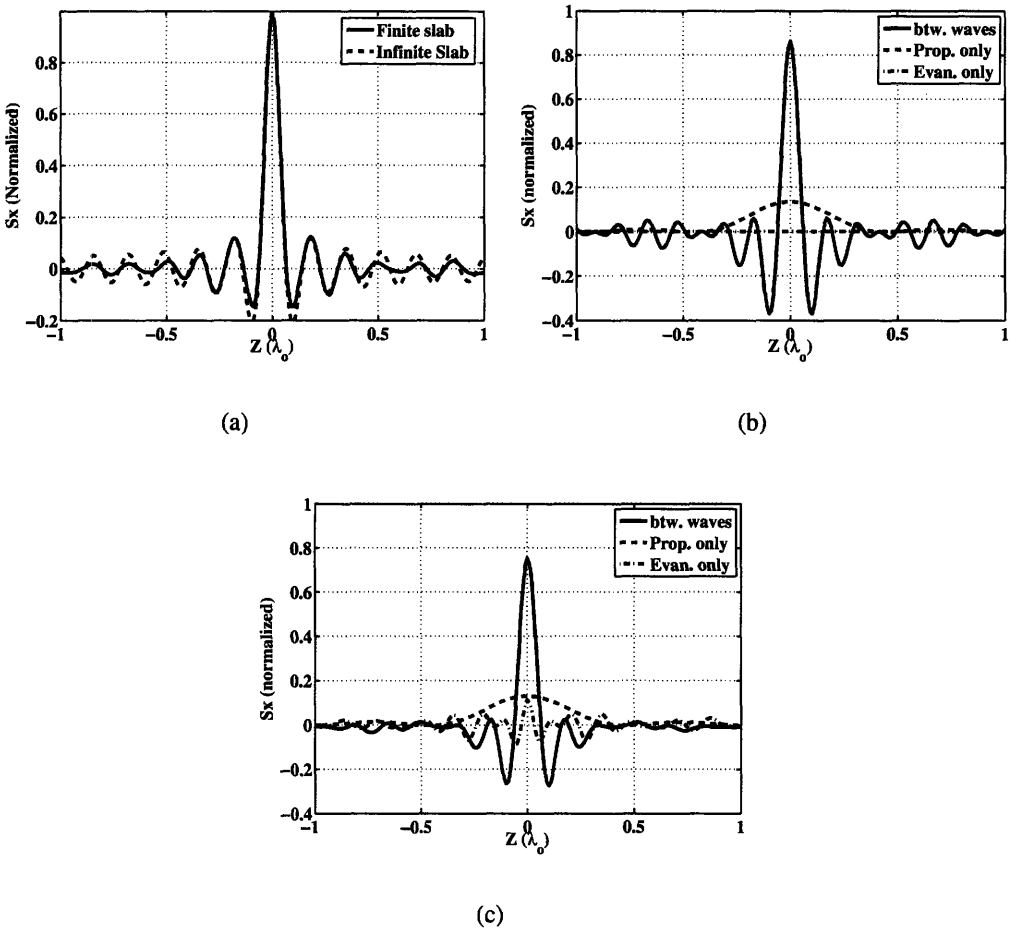

Figure 3-13: Explanation of negative energy streams in the LHM slab imaging. (a) Energy flux at the image plane from both an infinite slab and a finite slab. Negative energy stream can be seen in both cases. (b) Contributions to energy flux from wave interactions for the infinite slab. The fields are obtained analytically. (c) Contributions to energy flux from wave interactions for the finite slab. The fields are calculated from FDTD simulation. In (b) and (c), solid line: interactions between propagating waves and evanescent waves; dashed line: propagating waves only; dot-dashed line: evanescent waves only.

Returning to the case of the finite-size slabs, we show that the same conclusion holds.

The Poynting power at the image plane from the same finite-size slab used in the previous section (d_s=0.2 λ, L=2 λ) is shown in Fig. 3-13(a). Similar to the results from the infinite slab, negative time-averaged Poynting power can be observed. In order to study the contributions from the wave interactions, the time domain field data at the image plane obtained from FDTD simulations are first Fast-Fourier-transformed (FFT) into the frequency domain to verify the convergence. The data at the source frequency are then FFT from the spatial domain into the k space and a window function is applied to extract the propagating and evanescent waves. After being transformed back to the spatial domain by inverse FFT again, the wave interactions can be evaluated and the results are shown in Fig. 3-13(c). The contribution to the Poynting power from the evanescent waves is not exactly zero in this case, but it is much smaller compared to the contributions from other wave interactions. Similarly, the propagating waves only contribute to positive energy while the interactions between propagating and evanescent waves results in energy in the negative direction.

We emphasize again that the important reason for the negative energy stream to be prominent at the image plane is the amplification of the evanescent waves inside the LHM slabs which restores their amplitudes. Therefore, this phenomenon does not happen to right-handed material (RHM) slabs since the negligible evanescent wave energy due to the decay is overpowered by the energy from the propagating waves.

3.2.4 Summary

Imaging properties of finite-size LHM slabs are analyzed. In particular, we use an approximate analytical method to study the effect of the finite size by considering only the

aperture. It is shown that the approximated current sheet with a Gaussian shape truncated at the aperture reproduces the key features of the image spectrum. Hence the method can be used as a fast alternative to numerical simulations, although the simulations are still needed for a better accuracy. Furthermore, we explain that the negative energy stream at the image plane come from the inherent spectrum of the source, and more precisely from interactions between propagating waves and amplified evanescent waves from LHM slabs. This phenomenon does not depend on the finite size of the slab. We show that once again the capability of amplifying evanescent waves by LHM slabs make possible this unique property.

3.3 Conclusion

In this chapter, the transmission property, in particular the imaging property of LHM slabs are studied in detail. FDTD is used to simulate the LHM imaging capability. It is shown that the inherent mismatch in material properties limits the maximum resolution of the image. This mismatch is caused by the numerical implementation of the LHM slabs, therefore it is the limitation of FDTD method. An analytical expression is derived for the LHM slab properties, from which the limitation becomes clear. Numerical examples are also provided for the validation. With the better understanding of the simulation, we can now simulate the properties of LHM slab imaging. We show the unique property of the negative energy stream at the image plane. This property is further explained as the interaction between the waves from the point source after transmitting from the LHM slabs. Finally the property of finite-size LHM slabs are studied. It is demonstrated that the image resolution is not

sensitive to the slab size. Using the equivalent current sheets at the slab's boundary, we explain this property in an analytical expression which agrees well with the simulation results.

Chapter 4

Antenna Isolation Study Using Stratified Media Including LHMs

4.1 Introduction

This chapter deals with multi-layered media properties, in particular for the application of antenna isolations. The configuration is two horn antennas separated by a distance of 10 λ and with the antenna openings at the surface of the ground plane. In the past, RHM slabs have been used to improve the isolation between the antennas. With the introduction of LHM, MNG and ENG materials, it opens the door for new designs. Recent publications [30] [51] have studied the surface wave modes in the grounded slab configuration with all possible isotropic materials. However the actual field coupling level from different configurations, which are important for the estimation of the effectiveness of the isolation, are not readily available in the literatures. In this chapter, we calculate the actual coupling levels from dipole antennas which are then used as a figure of merit to compare different

designs. We start with general considerations for a stratified media configuration. The formulations for field evaluation in layered media including all isotropic material types are first presented. Secondly the asymptotic formulations are derived to predict field values at at the observation distance. The accuracy of the asymptotic formulation is compared with the field values obtained from the rigorous spectral Green's function method. Thirdly, the application setup for the antenna isolation is introduced, and the analogy to a dipole source is drawn to simplify the analysis. The design using a grounded single layer for isolation is carried out by two independent methods, with one using the asymptotic formulation and the other using Genetic Algorithm method together with the spectral Green's function approach. Both methods yield the same result. Finally, the GA method is used for the 5-layered media design for antenna isolation. It is noted that photonic band gap [52] materials use metallic structures [53] [54] have also been used for the antenna isolation applications. The sizes of this type of the structures are usually comparable with the wavelength [55] [56] therefore are usually large in size. In addition, the forbidden band is narrow which is undesirable in applications. These limitations can be avoided by using composited materials proposed in this chapter.

4.2 Field Evaluation In Layered Media

Since the isolation study is to find means to reduce the coupling level between dipole antennas, the method to evaluate fields inside layered media needs to be devised. There are two popular approaches to solve for fields due to dipoles in layered media. One approach [42] is to expand fields from a dipole in plane wave presentations by using Sommerfeld's

identity. The k vectors of these plane waves can be readily determined in each layer. The unknowns are then the field amplitudes associated with forward and backward propagating plane waves inside each layer. So each layer has only two unknowns to solve for either E or H fields except the last layer on either end. After applying the phase matching at the layered boundaries, the unknowns can be solved from a set of linear equations. As result, the unknowns can be solved in iterative formulations suitable for computer programming.

Another approach is the spectral Green's function method. This method applies 2D Fourier transformation to the Maxwell's equations and obtain the Green's functions due to dipoles in the spectral domain. Therefore, the field values can be calculated in spectral domain as well. The inverse Fourier transformation is applied to transform the fields back to the space domain to complete the procedure. The details in the implementation of this method is further illustrated in the following subsections.

4.2.1 Spectral Green's Functions

Spectral Green's function method is a well-established method [57] [58] for stratified media. The treatment in this section is similar to those in the published literatures [59] [60]. The slight difference is the simplification in obtaining the Green's functions which makes use of longitudinal Green's function components and the duality.

It is more convenient to obtain the Green's functions in spectral domain due to their simplicity. With the stratified media setup in $\hat{z}$ direction, the transformation between the

space and spectral domain can be established by the following Fourier transformation:

$$G(k_x, k_y) = \frac{1}{2\pi} \int_{-\infty}^{\infty} \int_{-\infty}^{\infty} G(x, y) e^{-ik_x x} e^{-ik_y y} dx dy \tag{4.1}$$

$$G(x, y) = \frac{1}{2\pi} \int_{-\infty}^{\infty} G(k_x, k_y) e^{ik_x x} e^{ik_y y} dk_x dk_y \tag{4.2}$$

Note that we don't use other symbols or notations for spectral domain values. The actual representations of the symbols shall be clear from their corresponding independent variables. Applying the above transformation to Maxwell's equations and noting that:

$$\frac{\partial}{\partial x} \rightarrow ik_x \quad \frac{\partial}{\partial y} \rightarrow ik_y$$

we have Maxwell's equations as

$$\nabla \times \overline{E} = i\omega\mu\overline{H} - \overline{M} \tag{4.3a}$$

$$\nabla \times \overline{H} = -i\omega\mu\overline{E} + \overline{J} \tag{4.3b}$$

where

$$\nabla = \nabla_t + \frac{\partial}{\partial z}\hat{z} = (ik_x\hat{x} + ik_y\hat{y}) + \frac{\partial}{\partial z}\hat{z}$$

By separating the fields into longitudinal and transverse components, Eq. (4.3) can be

rewritten as :

$$\nabla_t \times \overline{E}_t = (i\omega\mu H_z - M_z)\hat{z} \tag{4.4a}$$

$$\nabla_t \times \overline{H}_t = (-i\omega\epsilon E_z + J_z)\hat{z} \tag{4.4b}$$

$$\frac{\partial \overline{E}_t}{\partial z} - \nabla_t E_z = (i\omega\mu \overline{E}_t - \overline{M}_t) \times \hat{z} \tag{4.4c}$$

$$\frac{\partial \overline{H}_t}{\partial z} - \nabla_t H_z = (-i\omega\epsilon \overline{E}_t + \overline{J}_t) \times \hat{z} \tag{4.4d}$$

Further simplification due to Felsen and Marcuvitz [61] can be done to express tangential components by longitudinal components as

$$k_\rho^2 \overline{H}_t = (-i\omega\epsilon E_z + J_z)(\nabla_t \times \hat{z}) + \nabla_t \frac{\partial H_z}{\partial z} + \frac{i}{\omega\mu}\nabla_t(\nabla_t \cdot \overline{M}_t) + \frac{i}{\omega\mu}\nabla_t \frac{\partial M_z}{\partial z} \tag{4.5a}$$

$$k_\rho^2 \overline{E}_t = (i\omega\mu H_z - M_z)(\nabla_t \times \hat{z}) + \nabla_t \frac{\partial E_z}{\partial z} + \frac{i}{\omega\epsilon}\nabla_t(\nabla_t \cdot \overline{J}_t) + \frac{i}{\omega\epsilon}\nabla_t \frac{\partial J_z}{\partial z} \tag{4.5b}$$

In general, the problem of stratified media can be solved by finding two scaler potentials. In the example of Eq. (4.5), the two potentials are the longitudinal fields, *i.e* E_z and H_z. The potentials from Lorentz gauge are also used in other methods. In the source free region, Eq. (4.5) becomes

$$E_x = \frac{1}{k_\rho^2}(ik_x \frac{\partial E_z}{\partial z} - \omega\mu k_y H_z) \tag{4.6a}$$

$$E_y = \frac{1}{k_\rho^2}(ik_y \frac{\partial E_z}{\partial z} + \omega\mu k_x H_z) \tag{4.6b}$$

$$H_x = \frac{1}{k_\rho^2}(ik_x \frac{\partial H_z}{\partial z} + \omega\epsilon k_y E_z) \tag{4.6c}$$

$$H_y = \frac{1}{k_\rho^2}(ik_y \frac{\partial H_z}{\partial z} - \omega\epsilon k_x E_z) \tag{4.6d}$$

This set of equations is very handy when solving for the Spectral Green's functions. What we only need to find are just the longitudinal Green's functions. After that, Eq. (4.6) can be used to solve for the remaining ones. Therefore the unknowns for all the possible excitations are (both electric and magnetic excitations)

$$\begin{aligned}
\text{Electric Excitation TM case:} \quad & G_{EJ}^{zx}, G_{EJ}^{zy}, G_{EJ}^{zz} \\
\text{Electric Excitation TE case:} \quad & G_{HJ}^{zx}, G_{HJ}^{zy} \\
\text{Magnetic Excitation TM case:} \quad & G_{EM}^{zx}, G_{EM}^{zy} \\
\text{Magnetic Excitation TE case:} \quad & G_{HM}^{zx}, G_{HM}^{zy}, G_{HM}^{zz}
\end{aligned}$$

where Green's function's subscript stands for field and excitation and the superscript is the corresponding direction. For example, G_{EJ}^{zy} is the Green's function for Electric field in $\hat{z}$ due to an electric current source in $\hat{y}$. In the subscript, H is for magnetic field and M is for magnetic current source. TE mode refers to setting $E_z = 0$ and TM mode setting $H_z = 0$. Furthermore, using the duality theorem, we need only to find the Green's function due to electric excitations, which will be shown in the later sections. The method to solve for these fundamental Green's function is to utilize the transmission line analogy which is presented in the next section.

4.2.2 Transmission Line Analogy

The connection between the transmission line's voltages and currents and the fields in stratified media has been well-established [61] . Intuitively, the reasoning behind this analogy

can be understood as that the fields in spectral domain are only z dependent after the transformation, which resembles the voltage and currents in transmission line. So the undertaken task is to solve for the expressions for the fundamentals Green's functions and represent them in a form similar to the following transmission line equations:

$$\frac{\partial V(z,z')}{\partial z} = -jk_z Z_c I(z,z') + v\delta(z-z') \tag{4.7a}$$

$$\frac{\partial I(z,z')}{\partial z} = -jk_z \frac{1}{Z_c} V(z,z') + i\delta(z-z') \tag{4.7b}$$

The process will become clear from the following examples as we start to derive the Green's functions from this analogy.

For each excitation direction, generally there are two resulting fundamental Green's functions, except the case of longitudinal excitations. It is convenient to solve them one at the time, therefore the equations for the total fields are separated into TE and TM mode - two sets of equation. TE mode refers to setting $E_z = 0$ and TM mode setting $H_z = 0$. The procedure used to obtain fundamental Green's functions follows closely the derivation in [59]. This redundancy is necessary in order to give a complete picture of how the Green's functions are obtained.

G_{HJ}^{zx}, G_{HJ}^{zy} From Transverse Electric Excitation (TE case)

For this case, we have $E_z = 0$, $\overline{M} = 0$ and $\overline{J} = \overline{J}_t$, where the subscript 't' means transverse direction. From the source definition, we can write

$$\overline{J}_t = \delta(\overline{r} - \overline{r}')\hat{s}, \quad \hat{s} \in \hat{x}, \hat{y}$$

which can be transformed to the spectral domain as

$$\overline{J}_t = \frac{1}{2\pi}\delta(z-z')\hat{s}$$

Inserting the source condition into Eq. (4.5) and Eq. (4.4), the equations associated with the unknown Green's functions can be easily obtained as

$$\frac{\partial \overline{H_t}}{\partial t} = -\frac{k_z^2}{k_\rho^2}\nabla_t H_z - \frac{1}{k_\rho^2}(\hat{z}\times\nabla_t)(\nabla_t\cdot\overline{J_t}) - (\hat{z}\times\overline{J_t}) \tag{4.8}$$

$$\nabla_t \frac{\partial H_z}{\partial_z} = k_\rho^2 \overline{H_t} \tag{4.9}$$

Assuming $\overline{J_t} = \hat{x}J_x = \hat{x}\frac{1}{2\pi}\delta(z-z')$, Eq. (4.8) can be separated into two equations from its components:

$$\frac{\partial H_x}{\partial z} = -\frac{k_z^2}{k_\rho^2}ik_x H_z - \frac{k_x k_y}{k_\rho^2}J_x \tag{4.10a}$$

$$\frac{\partial H_y}{\partial z} = -\frac{k_z^2}{k_\rho^2}ik_y H_z - \frac{k_y^2}{k_\rho^2}J_x \tag{4.10b}$$

Rearranging Eq. (4.10) as

$$\frac{\partial}{\partial z}\left(\frac{k_\rho^2}{-k_x k_y}H_x\right) = -jk_z\frac{k_z}{\omega\mu}\left(\frac{\omega\mu}{k_y}H_z\right) + J_x \tag{4.11}$$

$$\frac{\partial}{\partial z}\left(\frac{\omega\mu}{k_y}H_z\right) = -jk_z\frac{1}{k_z/\omega\mu}\left(\frac{k_\rho^2}{-k_x k_y}H_x\right) \tag{4.12}$$

Note that i is replace by $-j$ in the expressions in order to be consistent with traditional transmission line equations. Comparing these two equations with Eq. (4.27) and Eq. (4.28),

it is easy to find

$$G_{HJ}^{zx} = \frac{k_y}{\omega\mu} V_j^{TE} \tag{4.13}$$

By the same token, we can find the contribution from $\overline{J} = \hat{y} J_y == \hat{x} \frac{1}{2\pi} \delta(z - z')$ as

$$G_{HJ}^{zy} = \frac{k_x}{\omega\mu} V_j^{TE} \tag{4.14}$$

In addition, the physical insights of this analogy is illuminated from this example. We can establish the one-to-one correspondence between the layer structure and the transmission line as

$$(d_i, \epsilon_{ri}, \mu_{ri}) \rightarrow (h_i, Z_{ci}, K_{zi})$$

where the connections are

$$h_i = d_i$$

$$k_{zi} = \sqrt{k_o^2 \epsilon_{ri} \mu_{ri} - k_\rho^2}$$

$$Z_c^{TE} = \frac{\omega \mu_o \mu_{ri}}{k_{zi}}$$

G_{EJ}^{zx}, G_{EJ}^{zy} From Transverse Electric Excitation (TM case)

Inserting the source condition into Eq. (4.5) and Eq. (4.4), we can write out the equation from the unitary source

$$\frac{\partial E_t}{\partial z} = \frac{k_z^2}{k_\rho^2} i k_s E_z \tag{4.15}$$

$$-ik_z \frac{\partial E_z}{\partial z} = k_\rho^2 E_t + \frac{1}{i\omega\epsilon} i k_s i k_{s'} \frac{1}{2pi} \delta(z - z') \tag{4.16}$$

where the s' refers to the excitation direction. In order to match the form of transmission line, we multiply Eq. (4.15) by $-k_\rho^2/k_s k_{s'}$ and Eq. (4.16) by $-i\omega\epsilon/k_s k_{s'}$. Upon replacing i by $-j$, we obtain

$$\frac{\partial}{\partial z}(-\frac{k_\rho^2}{k_s k_{s'}}E_t) = -jk_z\frac{k_z}{\omega\epsilon}(-\frac{\omega\epsilon}{k_{s'}}E_z) \tag{4.17}$$

$$\frac{\partial}{\partial z}(-\frac{\omega\epsilon}{k_{s'}}E_z) = -jk_z\frac{\omega\epsilon}{k_z}(-\frac{k_\rho^2}{k_s k_{s'}}E_t) + \frac{1}{2\pi}\delta(z-z') \tag{4.18}$$

It becomes clear from the analogy that we have

$$G_{EJ}^{zs'} = -\frac{k_{s'}}{\omega\epsilon}I_J^{TM} \tag{4.19}$$

From the TM cases, we can establish the one-to-one correspondence between the layer structure and the transmission line as

$$(d_i, \epsilon_{ri}, \mu_{ri}) \rightarrow (h_i, Z_{ci}, k_{zi})$$

where the connections are

$$\begin{aligned} h_i &= d_i \\ k_{zi}^{TM} &= \sqrt{k_o^2\epsilon_{ri}\mu_{ri} - k_\rho^2} \\ Z_c^{TM} &= \frac{k_{zi}}{\omega\epsilon_o\epsilon_{ri}} \end{aligned}$$

G_{EJ}^{zz} From Longitudinal Electric Excitation (TM case)

In developing the equations for the transmission line analogy, one will notice that the term $\partial^2 E_z/\partial^2 z$ exists in the equations. Consequently, the second order derivative form of the transmission line equation should be used which has the form of

$$\frac{\partial V^2}{\partial z^2} + k_z^2 V = \frac{\delta(z-z')}{\partial z} \tag{4.20}$$

Following the similar procedure, we can get

$$G_{EJ}^{zz\ TM} = -\frac{k_\rho^2}{\omega^2 \epsilon \epsilon'} I_J^{TM} \tag{4.21}$$

Thus, the longitudinal Green's functions due to electric excitations are all determined.

G_{EM}^{zy},G_{EM}^{zx},G_{HM}^{zx}, G_{HM}^{zy},G_{HM}^{zz} From Duality

To find the Green's function for magnetic current excitations, the simple way is to use duality theorem. In addition to the standard substitutions for E and H, J and M, μ and ϵ,

the duality needs to be applied to V and I as well. So the replacements for duality become

$$
\begin{aligned}
G_{EJ} &\rightarrow G_{HM} \\
G_{HJ} &\rightarrow -G_{EM} \\
\mu &\rightarrow \epsilon \\
\epsilon &\rightarrow \mu \\
V^{TE} &\rightarrow I^{TM} \\
I^{TM} &\rightarrow V^{TE}
\end{aligned}
$$

Notice that there is no sign change for V and I replacement since the transmission line equations Eq. (4.7) are symmetric. Applying above the replacement to Green's functions from electric excitations, we immediately get [59]

$$G_{HM}^{zx} = -\frac{k_x}{\omega\mu} V_M^{TE} \tag{4.22}$$

$$G_{HM}^{zy} = -\frac{k_y}{\omega\mu} V_M^{TE} \tag{4.23}$$

$$G_{HM}^{zz} = -\frac{k_\rho^2}{\omega\mu\mu'} V_M^{TE} \tag{4.24}$$

$$G_{EM}^{zx} = \frac{k_y}{\omega\epsilon} I_M^{TM} \tag{4.25}$$

$$G_{EM}^{zy} = -\frac{k_x}{\omega\epsilon} I_M^{TM} \tag{4.26}$$

Complete Solution of Green's Functions

With the longitudinal Green's function components found, Eq. (4.6) can be used to quickly solve for the rest components. The treatment of the $\partial/\partial z$ is to use the transmission line

equation in source free region so

$$\frac{\partial V(z)}{\partial z} = -jk_z Z_c I(z) \tag{4.27}$$

$$\frac{\partial I(z)}{\partial z} = -jk_z \frac{1}{Z_c} V(z) \tag{4.28}$$

Applying directly to the Eq. (4.6), we can write out the rest of Green's function components for electric excitations [59]

$$G_{EJ}^{xx} = -\frac{1}{k_\rho^2}(k_y^2 V_J^{TE} + k_x^2 V_J^{TM}) \tag{4.29a}$$

$$G_{EJ}^{yx} = \frac{k_x k_y}{k_\rho^2}(V_J^{TE} - V_J^{TM}) \tag{4.29b}$$

$$G_{EJ}^{xy} = \frac{k_x k_y}{k_\rho^2}(V_J^{TE} - V_J^{TM}) \tag{4.29c}$$

$$G_{EJ}^{yy} = -\frac{1}{k_\rho^2}(k_x^2 V_J^{TE} + k_y^2 V_J^{TM}) \tag{4.29d}$$

$$G_{EJ}^{xz} = -\frac{k_x}{\omega\epsilon'} V_J^{TM} \tag{4.29e}$$

$$G_{EJ}^{yz} = -\frac{k_y}{\omega\epsilon'} V_J^{TM} \tag{4.29f}$$

$$G_{HJ}^{xx} = -\frac{k_x k_y}{k_\rho^2}(I_J^{TE} - I_J^{TM}) \tag{4.29g}$$

$$G_{HJ}^{yx} = -\frac{1}{k_\rho^2}(k_y^2 I_J^{TE} + k_x^2 I_J^{TM}) \tag{4.29h}$$

$$G_{HJ}^{xy} = \frac{1}{k_\rho^2}(k_x^2 I_J^{TE} + k_y^2 I_J^{TM}) \tag{4.29i}$$

$$G_{HJ}^{yy} = \frac{k_x k_y}{k_\rho^2}(I_J^{TE} - I_J^{TM}) \tag{4.29j}$$

$$G_{HJ}^{xz} = \frac{k_y}{\omega\epsilon'} I_J^{TM} \tag{4.29k}$$

$$G_{HJ}^{yz} = -\frac{k_x}{\omega\epsilon'} I_J^{TM} \tag{4.29l}$$

and for magnetic excitations [59]

$$G_{EM}^{xx} = -\frac{k_x k_y}{k_\rho^2}(V_M^{TE} - V_M^{TM}) \tag{4.30a}$$

$$G_{EM}^{yx} = \frac{1}{k_\rho^2}(k_x^2 V_M^{TE} + k_y^2 V_M^{TM}) \tag{4.30b}$$

$$G_{EM}^{xy} = -\frac{1}{k_\rho^2}(k_x^2 V_M^{TE} + k_y^2 V_M^{TM}) \tag{4.30c}$$

$$G_{EM}^{yy} = \frac{k_x k_y}{k_\rho^2}(V_M^{TE} - V_M^{TM}) \tag{4.30d}$$

$$G_{EM}^{xz} = \frac{k_y}{\omega\mu'}(V_M^{TE}) \tag{4.30e}$$

$$G_{EM}^{yz} = \frac{k_x}{\omega\mu'}(V_M^{TE}) \tag{4.30f}$$

$$G_{HM}^{xx} = -\frac{1}{k_\rho^2}(k_x^2 I_M^{TE} + k_y^2 I_M^{TM}) \tag{4.30g}$$

$$G_{HM}^{yx} = -\frac{k_x k_y}{k_\rho^2}(I_M^{TE} - I_M^{TM}) \tag{4.30h}$$

$$G_{HM}^{xy} = -\frac{k_x k_y}{k_\rho^2}(I_M^{TE} - I_M^{TM}) \tag{4.30i}$$

$$G_{HM}^{yy} = -\frac{1}{k_\rho^2}(k_y^2 I_M^{TE} + k_x^2 I_M^{TM}) \tag{4.30j}$$

$$G_{HM}^{xz} = -\frac{k_x}{\omega\mu'} I_M^{TE} \tag{4.30k}$$

$$G_{HM}^{yz} = -\frac{k_y}{\omega\mu'} I_M^{TE} \tag{4.30l}$$

(4.30m)

For convenience, the Green's functions are summarized in Table 4.1 and Table 4.2.

4.2.3 Transformation to Space Domain

With the knowledge of spectral domain Green's function, the fields can be solved in the spectral domain. It is necessary to transform the fields back to spatial domain. This trans-

Table 4.1: Spectral Green's functions due to electric excitations [59]

Electric Excitations	
$G_{EJ}^{xx} = -\frac{1}{k_\rho^2}(k_y^2 V_J^{TE} + k_x^2 V_J^{TM})$	$G_{HJ}^{xx} = -\frac{k_x k_y}{k_\rho^2}(I_J^{TE} - I_J^{TM})$
$G_{EJ}^{yx} = \frac{k_x k_y}{k_\rho^2}(V_J^{TE} - V_J^{TM})$	$G_{HJ}^{yx} = -\frac{1}{k_\rho^2}(k_y^2 I_J^{TE} + k_x^2 I_J^{TM})$
$G_{EJ}^{zx} = -\frac{k_x}{\omega\epsilon} I_J^{TM}$	$G_{HJ}^{zx} = -\frac{k_y}{\omega\mu} V_J^{TE}$
$G_{EJ}^{xy} = \frac{k_x k_y}{k_\rho^2}(V_J^{TE} - V_J^{TM})$	$G_{HJ}^{xy} = \frac{1}{k_\rho^2}(k_x^2 I_J^{TE} + k_y^2 I_J^{TM})$
$G_{EJ}^{yy} = -\frac{1}{k_\rho^2}(k_x^2 V_J^{TE} + k_y^2 V_J^{TM})$	$G_{HJ}^{yy} = \frac{k_x k_y}{k_\rho^2}(I_J^{TE} - I_J^{TM})$
$G_{EJ}^{zy} = -\frac{k_y}{\omega\epsilon} I_J^{TM}$	$G_{HJ}^{zy} = -\frac{k_x}{\omega\mu} V_J^{TE}$
$G_{EJ}^{xz} = -\frac{k_x}{\omega\epsilon'} V_J^{TM}$	$G_{HJ}^{xz} = \frac{k_y}{\omega\epsilon'} I_J^{TM}$
$G_{EJ}^{yz} = -\frac{k_y}{\omega\epsilon'} V_J^{TM}$	$G_{HJ}^{yz} = -\frac{k_x}{\omega\epsilon'} I_J^{TM}$
$G_{EJ}^{zz} = -\frac{k_\rho^2}{\omega\epsilon\epsilon'} I_J^{TM}$	$G_{HJ}^{zz} = 0$

formation only applies to $\hat{x}$ and $\hat{y}$ and eventually reduces to one-dimentional due to the symmetry along the longitudinal axis. Defining [59]

$$\begin{aligned} S_n[A] &= \frac{1}{2}\int_{-\infty}^{\infty} H_n^{(2)}(k_\rho\rho) k_\rho^{n+1} A(k_\rho) \mathrm{d}k_\rho \\ &= \int_0^{\infty} J_n(k_\rho\rho) k_\rho^{n+1} A(k_\rho) \mathrm{d}k_\rho \end{aligned} \tag{4.31}$$

The transformation can be summarized in Table 4.3

4.2.4 Summary

The formulations to evaluate fields in layered media due to dipole excitations are completed. Green's function are first solved in spectral domain using the transmission line

Table 4.2: Spectral Green's functions due to magnetic excitations [59]

Magnetic Excitations	
$G_{EM}^{xx} = -\frac{k_x k_y}{k_\rho^2}(V_M^{TE} - V_M^{TM})$	$G_{HM}^{xx} = -\frac{1}{k_\rho^2}(k_x^2 I_M^{TE} + k_y^2 I_M^{TM})$
$G_{EM}^{yx} = \frac{1}{k_\rho^2}(k_x^2 V_M^{TE} + k_y^2 V_M^{TM})$	$G_{HM}^{yx} = -\frac{k_x k_y}{k_\rho^2}(I_M^{TE} - I_M^{TM})$
$G_{EM}^{zx} = \frac{k_y}{\omega\epsilon} I_M^{TM}$	$G_{HM}^{zx} = -\frac{k_x}{\omega\mu} V_M^{TE}$
$G_{EM}^{xy} = -\frac{1}{k_\rho^2}(k_x^2 V_M^{TE} + k_y^2 V_M^{TM})$	$G_{HM}^{xy} = -\frac{k_x k_y}{k_\rho^2}(I_M^{TE} - I_M^{TM})$
$G_{EM}^{yy} = \frac{k_x k_y}{k_\rho^2}(V_M^{TE} - V_M^{TM})$	$G_{HM}^{yy} = -\frac{1}{k_\rho^2}(k_y^2 I_M^{TE} + k_x^2 I_M^{TM})$
$G_{EM}^{zy} = -\frac{k_x}{\omega\epsilon} I_M^{TM}$	$G_{HM}^{zy} = -\frac{k_y}{\omega\mu} V_M^{TE}$
$G_{EM}^{xz} = \frac{k_y}{\omega\mu'}(V_M^{TE})$	$G_{HM}^{xz} = -\frac{k_x}{\omega\mu'} I_M^{TE}$
$G_{EM}^{yz} = \frac{k_x}{\omega\mu'}(V_M^{TE})$	$G_{HM}^{yz} = -\frac{k_y}{\omega\mu'} I_M^{TE}$
$G_{EM}^{zz} = 0$	$G_{HM}^{zz} = -\frac{k_\rho^2}{\omega^2\mu\mu'} V_M^{TE}$

analogy (the voltage and current in the expression for Greens' function). Once the spectral domain fields are obtained, transformation to spatial domain can be done utilizing the transformation in Table 4.3. This is typically done numerically for general layered media cases. However the numerical integration is not a trivial task. This is addressed in detail in the next section.

4.3 Sommerfeld Integrals

The previous section outlines the procedure to calculate the fields due to a source in layered media. The final step is to evaluate the integration with the form of Eq. (4.32), which is

Table 4.3: Formulations for Spectral to space domain transformation [59]

Spectral Domain	Space Domain
$G = A$	$G = S_0[A]$
$G = -ik_x A$	$G = -\cos(\phi) S_1[A]$
$G = -ik_y A$	$G = -\sin(\phi) S_1[A]$
$G = ik_x ik_x A$	$G = \frac{\cos(2\phi)}{\rho} S_1[A] - \cos^2(\phi) S_0[k_\rho^2 A]$
$G = ik_y ik_y A$	$G = -\frac{\cos(2\phi)}{\rho} S_1[A] - \sin^2(\phi) S_0[k_\rho^2 A]$
$G = ik_x ik_y A$	$G = -\frac{\sin(2\phi)}{\rho} S_1[A] - \frac{1}{2}\sin(2\phi) S_0[k_\rho^2 A]$

also called Sommerfeld-type integration.

$$\mathrm{I} = \int_0^\infty G(z, z'; \xi) J_v(\xi\rho) \xi \mathrm{d}\xi = \int_0^\infty f(\xi) \mathrm{d}\xi \tag{4.32}$$

The conventional way to evaluate such an integration in numerical means is the integration and summation procedure, namely to divide the integration range in small intervals and sum the integrand over the intervals for the total value. In the cases when the integration range goes to infinity, the strategy is to assume the integrand will decay fast enough so that only a small range is needed for the integration.

However, this approach cannot be directly applied to Sommerfeld-type integration. One can see that immediately by examining the asymptotic form of the Bessel functions as its integration variable becomes large. The Bessel function oscillates as function of cosine but decays only as $1/\sqrt{(\xi)}$.

$$J_n(\xi) \approx \sqrt{\frac{2}{\pi\xi}} \cos(\xi - n\pi/2 - \pi/4) \tag{4.33}$$

Such a slowly convergent oscillatory behavior [62] can post serious burden on the computational effort. In other words, without optimizing the numerical method for the integration, the convergence is very slow and the integration needs to be extended to an impractical range for the variable [63]. Another feature of the integrand, typically associated with the layered media problem [64] [65] is that there may exist singularities on the integration path. The popular method to get around this problem is to separate the integration into two parts. The first part is to deform the integration path in the third quadrant into a half elliptical shape to avoid the guided wave poles and the branch points. The second part is to integrate the tail till infinity.

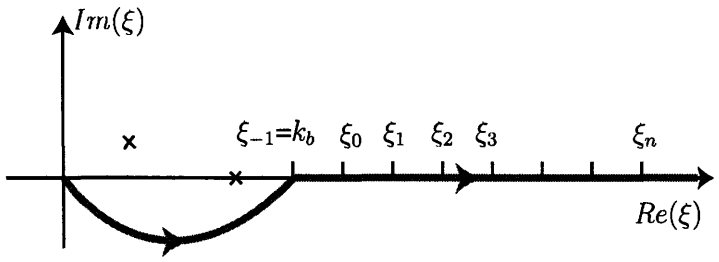

(a)

Figure 4-1: Illustration of Sommerfeld integration path. The "x" indicates pole locations.

For the second part of the integration, namely Sommerfeld tail integration, there are many research work [66] [67] [68] published on this subject. An excellent review article on this is [69]. We choose the weighted-averages method [69] due to its simplicity and accuracy over a wide range of integrands. For the Sommerfeld integration tail. If we assume that the integrand $f(\xi)$ can be written as

$$f(\xi) = g(\xi)p(\xi) \tag{4.34}$$

where $g(\xi)$ possesses a property of

$$g(\xi) = \frac{e^{-\zeta\xi}}{\xi^{\alpha}} \tag{4.35}$$

and $p(\xi)$ is a periodic function with a periodicity of $2q$, that is

$$p(\xi + q) = -p(\xi) \tag{4.36}$$

In order to use weighted-averages method, we first calculate the integration up to nth intervals with the interval equal to half of the periodicity of the integrand. So we have

$$S_n = \sum_{i=0}^{n} u_i \tag{4.37}$$

where

$$u_i = \int_{\xi_{i-1}}^{\xi} f(\xi)\mathrm{d}\xi \tag{4.38}$$

where n is a finite number with a value between 10 to 15 usually. Once S_n is calculated , an integrative procedure using weighted-averages method [70] [71] can be applied to obtain the final integration result. The procedure can be expressed as

$$S_n^{(k+1)} = \frac{S_n^{(k)} + \eta_n^{(k)} S_{n+1}^{(k)}}{1 + \eta_n^{(k)}} \tag{4.39}$$

where k is the iteration number and $\eta_n^{(k)}$ is the iteration coefficient. With a series of n+1 terms, the first iteration reduces the series to n terms, the second iteration to n-1 terms and

so forth. After n iterations, only one term is left which is $S_o^{(n)}$. This is the extrapolated result for the integration [72] [73]. The essence of weighted-averages method is in the prediction of the iteration coefficient. Since the asymptotic form of the integration can be obtained. it can be shown that a proper expression for $\eta_n^{(k)}$ can be found as

$$\eta_n^{(k)} = e^{q\xi}(\frac{\xi_{n+1}}{\xi_n})^{\alpha+pk} \tag{4.40}$$

4.3.1 Numerical Validation

The first example illustrates the importance of using accelerated numerical methods such as weighted-averages method to evaluate slowly converging functions. Eq. (4.41) is a sum of a series.

$$\sum_{n=0}^{\infty} \frac{(-1)^n}{\sqrt{n+1}} \tag{4.41}$$

The exact value is 0.604898643421630, and the summation up to 10^7 terms is 0.605056. If we define the figure of merit as

$$\text{Number of Significant Digits} = -\log_{10}\left|\frac{f_{cal} - f_{ex}}{f_{ex}}\right| \tag{4.42}$$

where the f_{cal} is the calculated value through integration, f_{ex} is the exact value. Then number of significant digits is only 3 after 10^7 terms. On the other hand, if weighted-averages method is used (the result is shown in Fig. 4-2), the number of significant digits can be improved to around 14 with only ten terms, and it is better than Iterated Aitken's method [74]. It is obvious that the improvement is very significant from this example. The

parameter used in the integration are $p = 2$, $\zeta = 0$, $\alpha = 0.5$, $q = 0$ for Eq. (4.40).

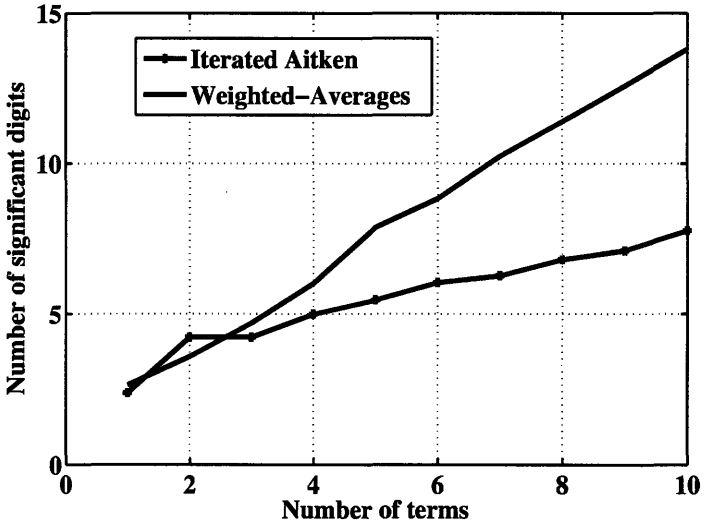

Figure 4-2: Evaluation of Eq. (4.41) using weighted-averages method. Results from Iterated Aitken's method is also included for comparison.

The second example is to evaluate Sommerfeld identity as

$$\int_0^\infty \frac{e^{-jk_z|z|}}{jk_z} J_0(\xi\rho)\xi \mathrm{d}\xi = \frac{e^{-jk_0 r}}{r} \tag{4.43}$$

with $k_z = \sqrt{k_0^2 - \xi^2}$. The slow convergence characteristics of the Bessel function justifies the usage of weighted-averages method. The test is done at z=0, which is the worse case since the decay of the integration is $1/\xi^{1/2}$. The only pole is at $\xi = k_0$. The wavevector $k_0 = \omega\sqrt{\mu\epsilon}$ with $\mu = \mu_o$ and $\epsilon = (16 + i0.1)\epsilon_o$. The integration can be done by two parts as illustrated in Fig. 4-1. The first part is to integrate to k_b using half-elliptical path. The value of k_b is chosen as $(\sqrt{\text{real}(\epsilon)/\epsilon_o} + 1)k_o$ but with a maximum of $0.5k_o$, while the value for the minor axis is $k_a = 0.5k_o/(\rho k_o/(2\pi))$, where k_o is the free space wavenumber. The second part is to integrate the tail using weighted-averages method. The interval is chosen as π/ρ.

Total number of intervals are 20. While the integration of the first part is trivial, it is found that Gaussian Quadrature method can improve the integration accuracy with only much less points. The number of points used in Gaussian integration for this example is 1000. The parameters for the weighted-averages method are $p = 1$, $\zeta = |z|$, $\alpha = 0.5$, $q = \pi/\rho$. The result is shown in Fig. 4-3. When ρ is less than $10\lambda_o$ ($\log_{10}(k_\rho\rho) < 1$), the number of significant digits can be maintained above 6. However there is a visible trend which shows that the accuracy decreases as ρ increases. This trend continues in Fig. 4-4 and starts to become a problem when ρ is greater. The integration becomes invalid at $\rho_o = 50\lambda$. In order to understand this result, we need to go back to the asymptotic form of the Bessel function Eq. (4.33). It can be seen that as ρ increases, the integrand oscillates faster due to $\cos(k_\rho\rho)$. However, the overall decay of the integrand is still as $1/\sqrt{k_\rho}$ which is not changed. Since the intervals are corresponding to the oscillation periodicity, keeping the number of intervals the same means less and less coverage on the k_ρ axis. The weighted-averages method works the best when the series form the integration over the intervals reflects the overall decay of the integrand. At large ρ, due to the small coverage on k_ρ axis, this information about the overall decay is lost and the method yields poor results as consequence.

The third example is shown in Eq. (4.44), which is to evaluate the derivative of Sommerfeld identity.

$$\int_0^\infty \frac{e^{-jk_z|z|}}{jk_z} J_1(\xi\rho)\xi^2 \mathrm{d}\xi = (1 + jkr)\frac{\rho e^{-jkr}}{r^3} \tag{4.44}$$

A unique feature of this integral is that its integrand diverges as $\xi^{1/2}$ as ξ goes to ∞, even though the integral itself converges. Although the development of weighted-averages

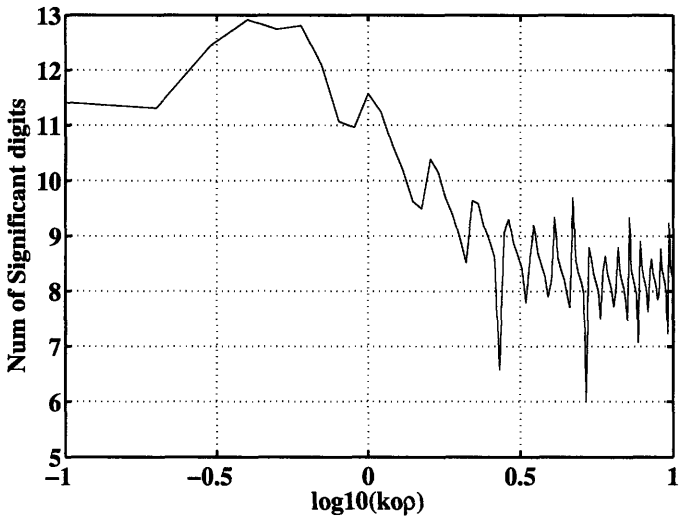

Figure 4-3: Evaluation of Eq. (4.43) using weighted-averages method. The observation is at $z = 0$ in the range of $k_o\rho$ from 0.1 to 10.

method is based on the converging integrand, the result shown in Fig. 4-5 suggests that the method can still produce accurate results in such case. The half-elliptical integration's parameters are the same as the ones used in the previous example. The interval is chosen as π/ρ and the total number intervals is increased to 100. The number of points used in Gaussian Quadrature is 1000. The parameters for weighted-averages method are $p = 1$, $\zeta = |z|$, $\alpha = -0.5$, $q = \pi/\rho$ for Eq. (4.40). Again the same trend of losing accuracy as ρ increases still exist. At $\rho = 50\lambda_o$, the integration result is invalid. Note that the above integration results are based on the parameters chosen for the integration. Certainly the accuracy can be improved by increasing the number of intevals because the asymptotic behavior can be better represented by using more terms.

The above examples show that Weighted-averages method is very efficient in evaluating slowly converging integrations as along as the asymptotic behavior of the integrand is known. A potential issue with the application to Sommerfeld integrals is the accuracy

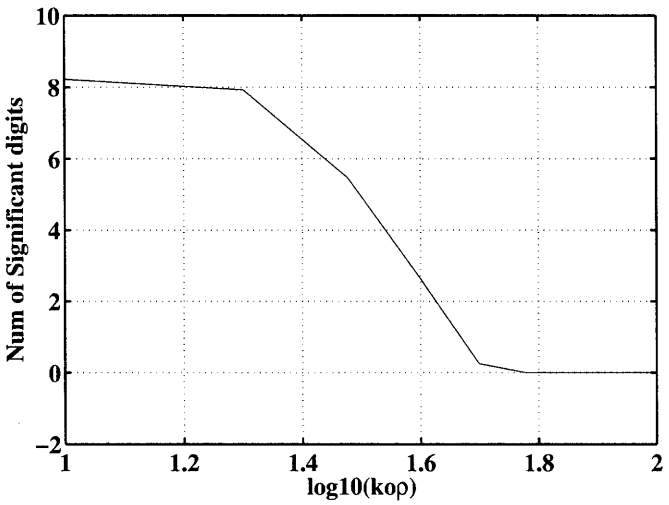

Figure 4-4: Evaluation of Eq. (4.43) using weighted-averages method. The observation is at $z = 0$ in the range of $k_o\rho$ from from 10 to 100.

degrades quickly as ρ increases beyond $50\lambda_o$.

Finally, in order to valid the Green's function presented in the previous sections and to use weighted-averages method to perform the integral transformation back to spatial domain, an example [59] of the multi-layered media with dipole excitations is presented. The multilayer structure is setup above a ground plane. The material of the first layer (closest to the ground plane) is ($\mu_{1r} = 1, \epsilon_{1r} = 5$). Other materials are ($\mu_{2r} = 1, \epsilon_{2r} = 7$), ($\mu_{3r} = 1, \epsilon_{3r} = 2$), ($\mu_{4r} = 1, \epsilon_{4r} = 4$). The thickness of the layers are 1mm, 2mm, 0.7mm, and 1.3mm for layer one to four respectively. The five layer is half space with air. This setup resembles a multi-layered structure in an integrated circuit design. The source is placed at z=0.5mm. The observation is along z axis at three different locations at y direction. The dipole is considered as horizontal dipole excitation. The result is shown in Fig. 4-7. The results are in very good agreement with the referenced data [59].

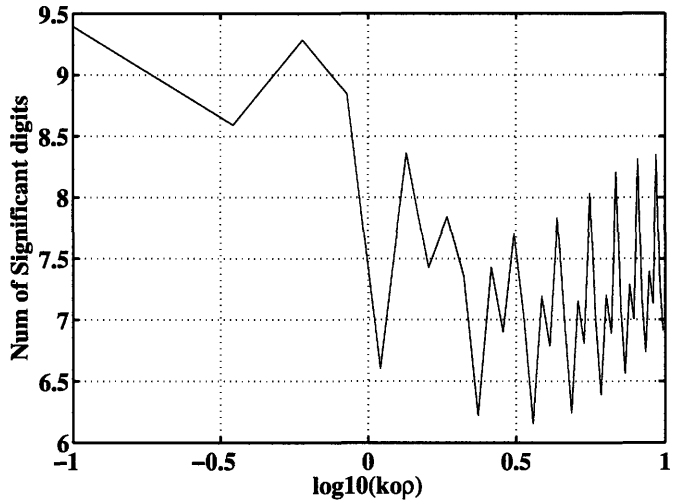

Figure 4-5: Evaluation of Eq. (4.44) using weighted-averages method. The observation is at $z = 0$ in the range of $k_o\rho$ from 0.1 to 10.

4.4 Antenna Isolation In Grounded Slabs

4.4.1 Position Of the Problem

In this section, we intend to use the available four different types of materials, *i.e.* RHM, LHM, MNG, ENG, to design a grounded slab that offers the best isolation for the antennas. The LHM materials used for isolation has been studied in the literatures [46] [75] [76] [77], but the studies have mainly been focused on the guidance conditions only. The geometry of the setup is shown in Fig. 4-8, where a finite slab is used in between two horn antennas for the isolation. Fig. 4-8(b) shows the field coupling between the antennas in two directions (for both TE and TM modes). The coupling is mainly contributed by E_z field (in $\hat{x}$ direction) so the TM mode is dominant. To further validate the TM mode coupling, the field propagation through the grounded slab with and without TM mode suppressions are shown in Fig. 4-9. The effect of the suppression can clearly be seen.

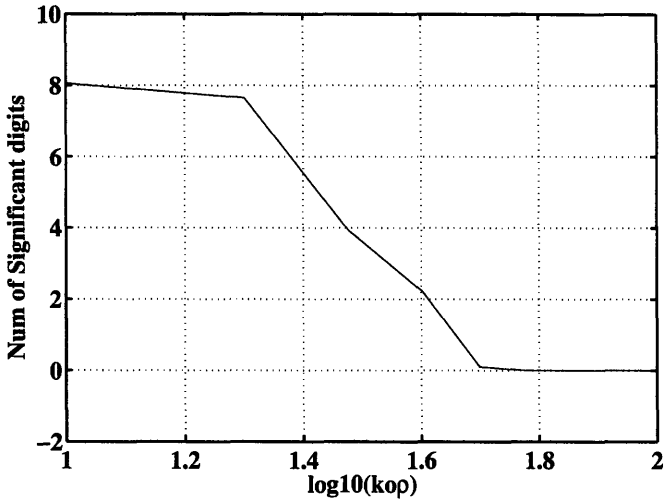

Figure 4-6: Evaluation of Eq. (4.44) using weighted-averages method. The observation is at $z = 0$ in the range of $k_o\rho$ from 10 to 100.

With this information, we approximate the configuration as dipole antenna coupling in infinite grounded slabs. The dipole that best represents the actual configuration is a $\hat{z}$ directed dipole. Therefore the problem undertaken is to design slab parameters for the best isolation between $\hat{z}$ directed VEDs.

The first step is to study the guidance condition of the grounded slab so that the surface wave propagation inside the slab can be eliminated by carefully choosing the material parameters. The Green's function approach is used to evaluate the fields in grounded slabs, for which we extend the application to include LHM, MNG and ENG in addition to RHM. We study the Vertical Eclectic Dipole (VED) since it resembles the setup we are considering. With the code that can evaluate the fields inside the grounded slab for any type of isotropic materials. Genetic algorithm (GA) is used to optimize the design. To validate the GA results, asymptotic formulations for the fields due to VED are also obtained. It is found that both methods yield the same design for the problem at hand.

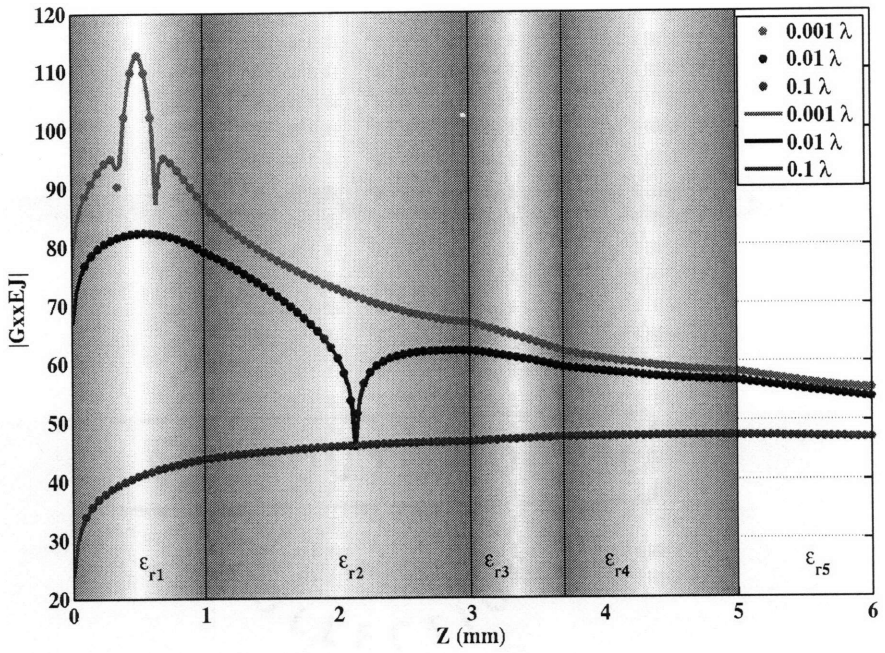

Figure 4-7: Fields due to dipole in a 5-layered media. $\mu_r = 1$ for all the layers. The permittivity of all the layers are $\epsilon_{1r} = 5$, $\epsilon_{2r} = 7$, $\epsilon_{3r} = 2$, $\epsilon_{4r} = 4$ and $\epsilon_{4r} = 1$. The data with dots are taken from the reference, while the solid lines are calcualted from this work.

4.4.2 Guidance Conditions

There are mainly three methods [78] to find the guidance conditions for the grounded slab. The simplest method is to use the transmission line analogy as mentioned in Section 4.2.2. The layer of air, slab and ground plane forms a resonant circuit which is equivalent to the guidance condition at resonance. The second method is to derive the expressions for the fields inside the slab. Usually the expression of the fields can be turned into an integral representation. The singularity of the integrand, if exists, corresponds to the surface wave mode which can be used to obtain the guidance condition.The third method, which gives the physical intuition, is to consider the guidance condition as the constructive interference of the waves insider the slab. The mathematical expression of the third method can be

(a) Setup of CST simulation

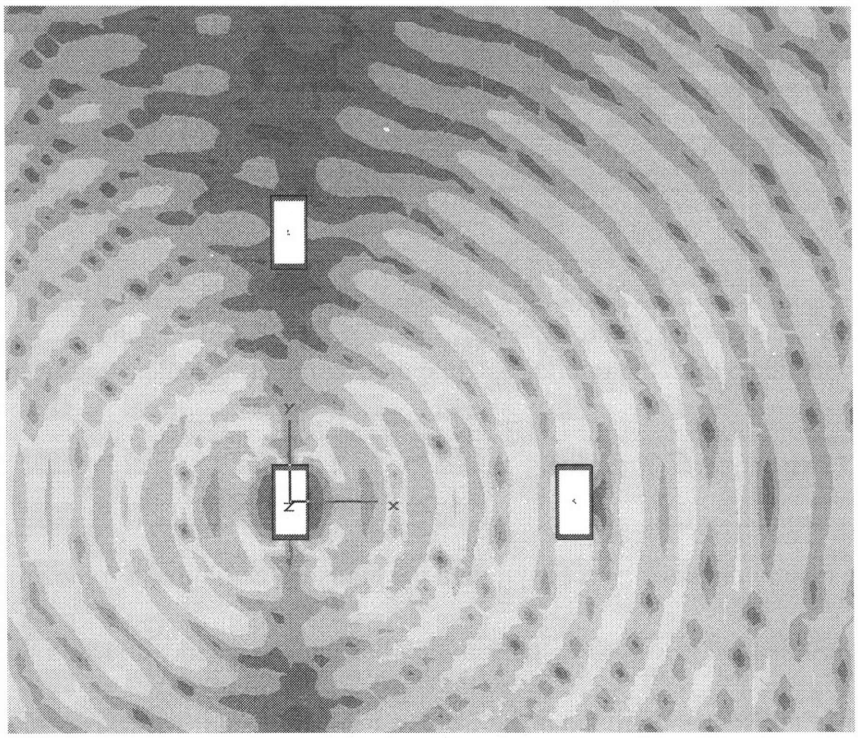

(b) Fields from the antenna

Figure 4-8: Antenna isolation study setup using finite slabs in CST. (a) the CST setup with waveguide ports. (b) E_z field from the waveguide port which is used to simulate transmitting antenna. Other two ports are for the measurement of isolation efficiency. (Courtesy of Dr. Hongsheng Chen)

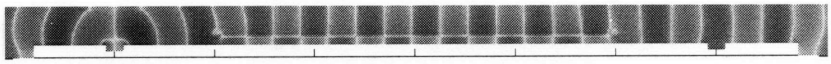

(a) With surface wave modes

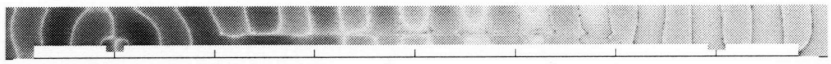

(b) Without surface wave modes

Figure 4-9: Fields in finite grounded slab. (a) The slab is ($\mu_r = -0.1$, $\epsilon_r = -2$) with a thickness of 4 mm. (b) The slab is ($\mu_r = -0.1$, $\epsilon_r = -0.1$) with a thickness of 4 mm. (Courtesy of Dr. Hongsheng Chen)

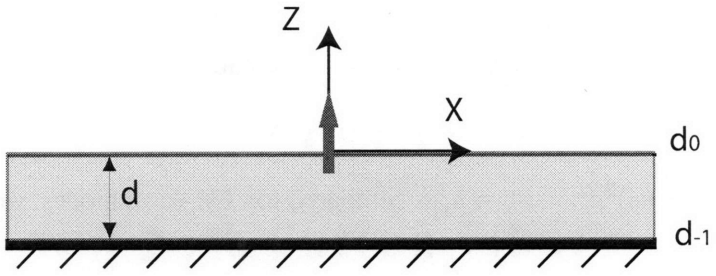

(a)

Figure 4-10: Setup of grounded stub with $\hat{z}$ directed electric dipole. Genetic Algorithm is used to optimize the slab parameters for the best antenna isolation.

written as [42]

$$R_+ R_- = 1 \tag{4.45}$$

where R_+ and R_- are the reflection coefficients looking into each side of the slab from any reference point inside the slab. For the grounded slab case, the convenient choice for the reference point is at the ground plane interface. So we have

$$R_+ = \frac{1 - p_{10}}{1 + p_{10}} e^{i2k_z d} \quad R_- = -1 \tag{4.46}$$

First we consider the slab to be RHM. For TE wave modes, we have [42]

$$p_{01} = \frac{i\mu_1 \alpha_{0z}}{\mu_0 k_z} \tag{4.47}$$

Plugging into Eq. (4.45), we can easily find the guidance condition as [42]

$$\sqrt{\Delta^2 - x^2} = \frac{-1}{\mu_r} x\text{ctan}(x) \tag{4.48}$$

where $\Delta^2 = (k_1 - k_0)^2 d^2, \quad x^2 = k_z^2 d^2$ Similarly, for TM wave modes, we use

$$p_{01} = \frac{i\epsilon_1 \alpha_{0z}}{\epsilon_0 k_z} \tag{4.49}$$

And the guidance condition can be written as [42]:

$$\sqrt{\Delta^2 - x^2} = \frac{1}{\epsilon_r} x\tan(x)$$

We also call these guided surface wave modes real wavenumber modes since the longitudinal wavenumber (k_z) inside the slab is real. The solutions to these guidance conditions reveal the surface wave modes that can exist inside the grounded slab for a given slab configuration. Typically a graphic solution is used to show the solutions to these equations. An example is shown in Fig. 4-11 for both TE and TM modes. For TM modes, the surface waves always exist since there is at least one intersection points. For TE modes, the cutoff for the surface wave modes happens at $\alpha_{0z}d < \pi/2$.

If LHM is used for the slab, the surface wave modes can have real wavenumbers as well as imaginary wavenumbers. The expression for the TE modes with real wavenumbers is [9]

$$\sqrt{\Delta^2 - x^2} = \frac{-1}{\mu_r} x\tan(x) \tag{4.50}$$

where $\Delta^2 = (k_1 - k_0)^2 d^2, \quad x^2 = k_z^2 d^2$. And for the TM modes is [9]

$$\sqrt{\Delta^2 - x^2} = \frac{1}{\epsilon_r} x\tan(x) \tag{4.51}$$

The graphic representation of these guidance conditions can be seen from Fig. 4-12. Due to the negative constitutive parameters, the cutoff conditions for the surface wave modes for LHM slabs are different from ones for RHM slabs. For TM modes, the cutoff exists which depends on the tangential intersection between the solid lines and dashed lines. For TE modes, however, there is no cutoff at zero frequency, but there exist a range in which the surface wave modes cannot propagate.

For grounded LHM slabs, it is also known that imaginary wavenumber surface wave

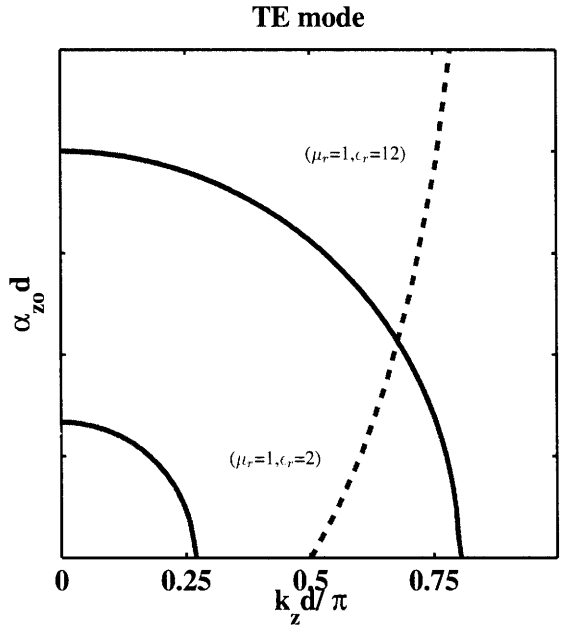

(a) TE surface wave modes

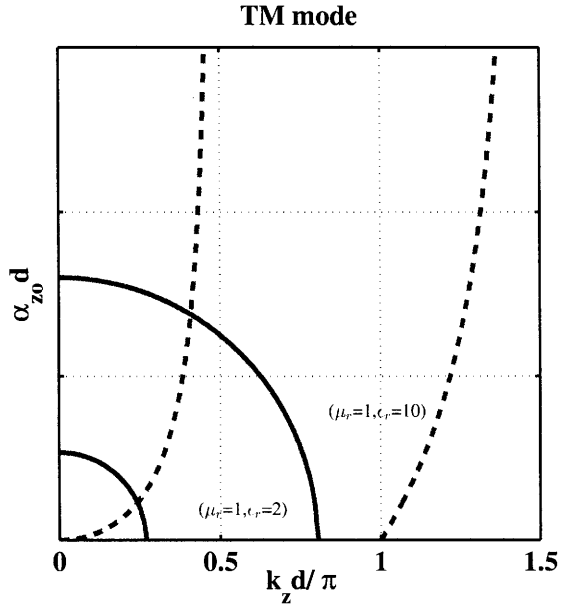

(b) TM surface wave modes

Figure 4-11: Guidance Condition for grounded RHM slab. The Dashed curves are for the right hand side of Eq. (4.48) and solid curves are the left hand side. The intersections indicate the existence of the modes.

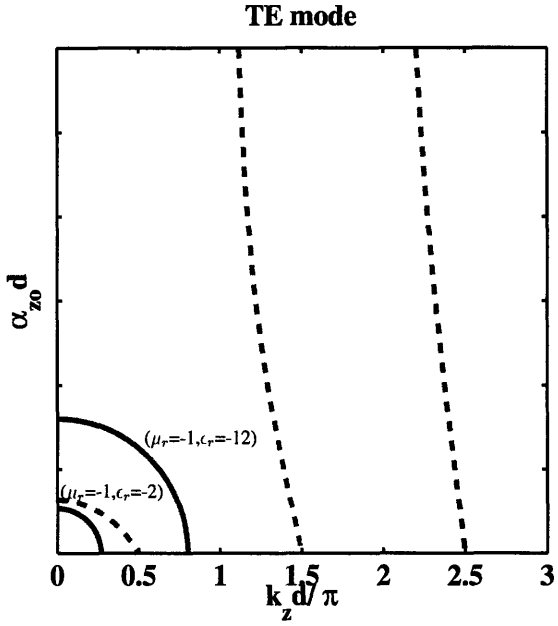

(a) TE mode with real wavenumbers

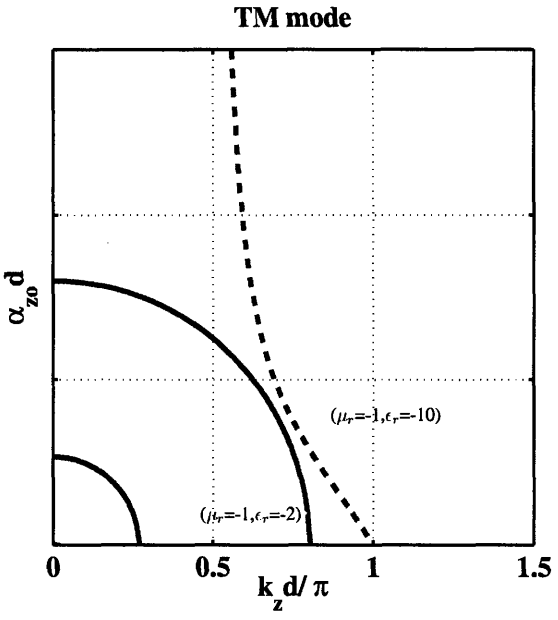

(b) TM mode with real wavenumbers

Figure 4-12: Guidance Condition for grounded LHM slab. The intersections indicate the existence of the modes. The modes are with real wave numbers.

modes can exist. The expression for TE modes can be obtained from Eq. (4.48) by changing k_z to α_z and it is written as [29]

$$-\alpha_z^2 d^2 + \frac{\alpha_z d^2}{\mu_r^2}\text{ctanh}^2(\alpha_z d) = (k_1^2 - k_0^2)d^2 \tag{4.52}$$

The expression for TM modes with imaginary wave numbers can be obtained in the similar way and it is written as [29]

$$-\alpha_z^2 d^2 + \frac{\alpha_z d^2}{\epsilon_r^2}\tanh^2(\alpha_z d) = (k_1^2 - k_0^2)d^2 \tag{4.53}$$

The graphic representation of these guidance conditions can be seen from Fig. 4-13. In the figure, solid curves become straight lines, and the values are associated with $(k_1^2 - k_0^2)$. Therefore by visual inspection, it can be seen that the surface wave modes can be eliminated by either increasing the value of k_1^2 or the slab thickness d. This is true for both TE and TM evanescent wave modes.

If the slab material becomes MNG, the real wavenumbers modes can no longer exist. So only the imaginary wavenumber modes need to be considered. A simple analysis can show that MNG can not satisfy the guidance condition for the TM evanescent wave modes therefore only TE evanescent wave modes can exist which is [29] [30]

$$\alpha_{0z} d = \frac{-\alpha_z d}{\mu_r}\text{ctanh}(\alpha_z d) \tag{4.54}$$

The graphical solution of this equation is shown in Fig. 4-14(a). The conditions for the cutoff are not straightforward.

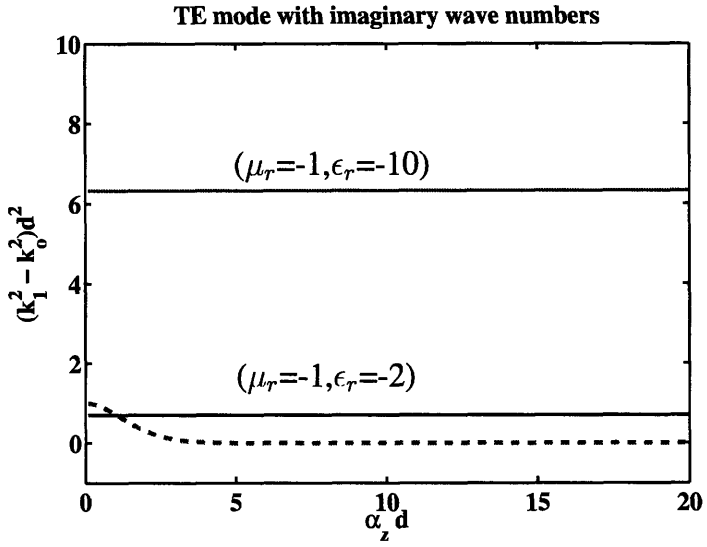

(a) TE mode with imaginary wave numbers

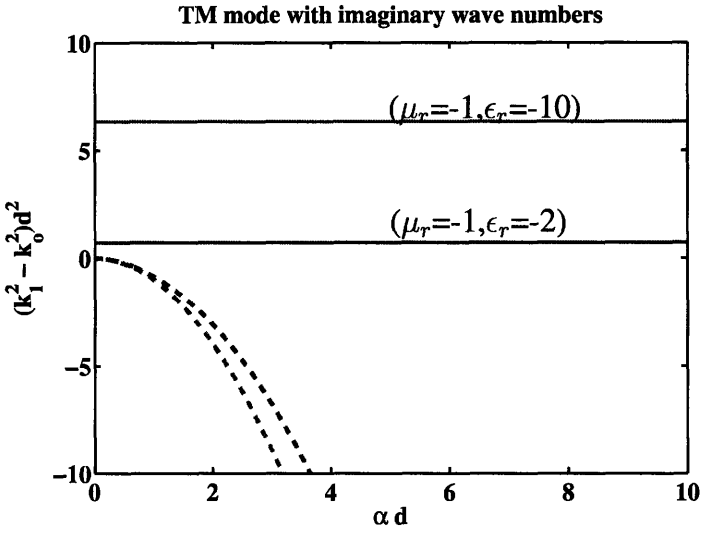

(b) TM mode with imaginary wave numbers

Figure 4-13: Guidance Condition for grounded LHM slab. The intersections indicate the existence of the modes. The modes are with imaginary wave numbers.

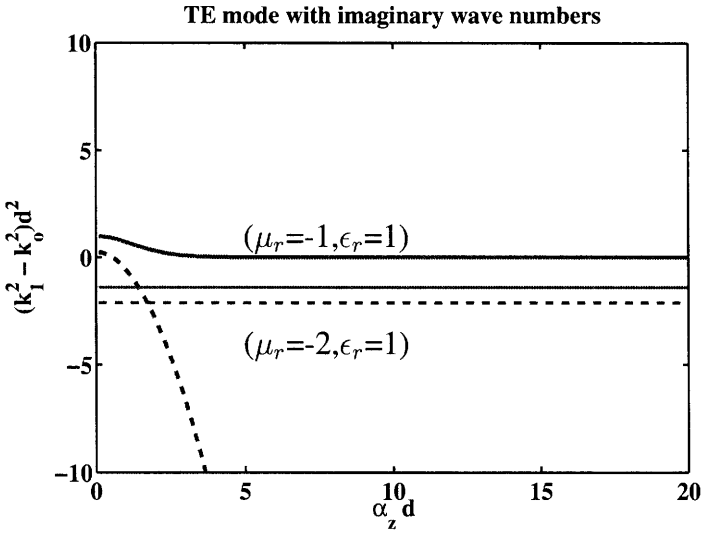

(a) TE modes in MNG slabs

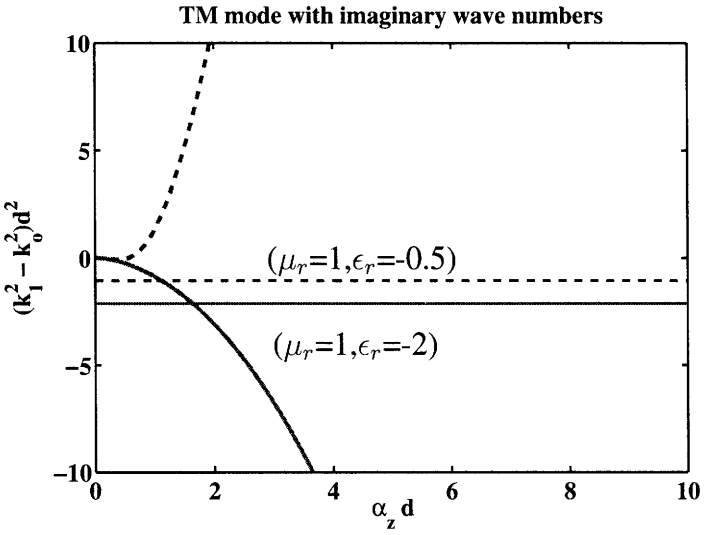

(b) TM modes in ENG slabs

Figure 4-14: Guidance Condition for grounded MNG slabs and ENG slabs. The intersections indicate the existence of the modes. The modes are with imaginary wave numbers.

The last case is ENG slab. With a similar analysis, it can be shown that the slab can only have TM evanescent wave modes which can be expressed as [79]

$$\alpha_{0z}d = \frac{-\alpha_z d}{\mu_r}\tanh(\alpha_z d) \tag{4.55}$$

The graphical solution of this equation is shown in Fig. 4-14(b).

In summary, the guidance conditions for the four different type of materials are tabulated in Table 4.4 and Table 4.5.

Table 4.4: Guidance condition for real wavenumber surface wave modes

	Real Wavenumber surface wave modes (propagating wave modes)	
	TE	TM
RHM	$\sqrt{\Delta^2 - x^2} = \frac{-1}{\mu_r}x\text{ctan}(x)$	$\sqrt{\Delta^2 - x^2} = \frac{1}{\epsilon_r}x\tan(x)$
LHM	$\sqrt{\Delta^2 - x^2} = \frac{-1}{\mu_r}x\text{ctan}(x)$	$\sqrt{\Delta^2 - x^2} = \frac{1}{\epsilon_r}x\tan(x)$
MNG	None	None
ENG	None	None

Table 4.5: Guidance condition for imaginary wavenumber surface wave modes

	Imaginary Wavenumber surface wave modes (evanescent wave modes)	
	TE	TM
RHM	None	None
LHM	$\alpha_{0z}d = \frac{-\alpha_z d}{\mu_r}\text{ctanh}^2(\alpha_z d)$	$\alpha_{0z}d = \frac{-\alpha_z d}{\epsilon_r}\tanh^2(\alpha_z d)$
MNG	$\alpha_{0z}d = \frac{-\alpha_z d}{\mu_r}\text{ctanh}^2(\alpha_z d)$	None
ENG	None	$\alpha_{0z}d = \frac{-\alpha_z d}{\epsilon_r}\tanh^2(\alpha_z d)$

4.4.3 Applications to LHM And Plasma Medium

In general, an isotropic medium can be one of the four types, namely RHM, LHM, ϵ Negative Material (ENG) or μ Negative Material (MNG). In the past, the formulations using Green's functions to evaluate fields in layered media have been applied to RHMs only. In this section, we will extend the application to include LHM, ENG and MNG. The formulations developed in previous sections are generic to isotropic materials, since there is no underline assumption in the derivations. However, the actual implementation of the formulations will be different for different materials. The main difference is on how to determine the extend of semi-elliptical integration range which needs to include all poles.

It is known that in layered media configuration, the singularities of the integrand correspond physically to the surface wave modes inside the layer. For RHM materials, since only the real wavenumber modes exist, the surface wave poles occurs in the range of $[k_o, k_{max}]$, where k_{max} is the maximum value of wave vectors in all the layers. k_o is the free space wave vector. Therefore the choice of the semi-elliptical integration range is very simple: to choose k_b to be greater than k_{max}. However this straightforward choice needs to be modified for other materials since evanescent wave modes can now exist.

For single layer medium backed by a ground plane, the guidance condition for MNG can be rewritten as [51]

$$\tanh(\sqrt{k_\rho^2 - k_1^2}d) = -\frac{\sqrt{k_\rho^2 - k_1^2}}{\mu_r\sqrt{k_\rho^2 - k_o^2}} \tag{4.56}$$

The solution of this equation for k_ρ determines the location for the pole. Since we only need to know the maximum possible value for the solution, the approximation can be made

to simplify the analysis. If we denote the left hand side of Eq. (4.56) as LHS_{MNG} and the right hand side as RHS_{MNG}, the general shape of the function can be shown in Fig. 4-15 Since we also know the following relationship exists (for $x > 0$):

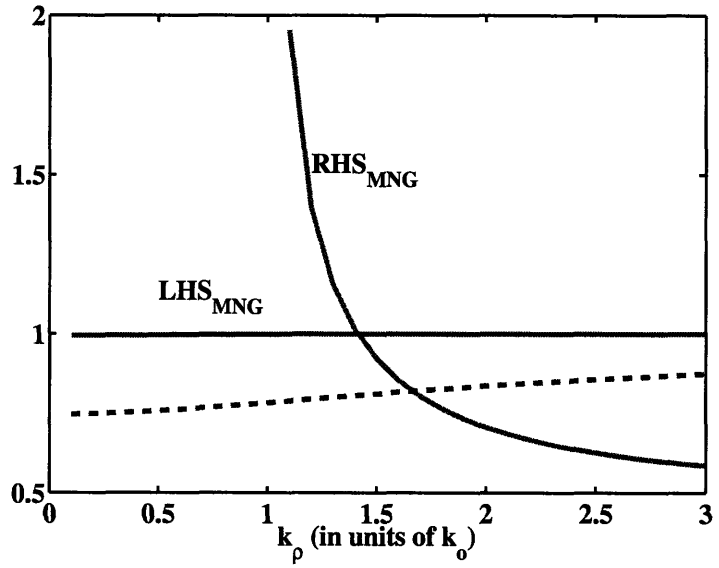

Figure 4-15: Illustration to show that the approximated function can be used to estimate the max k_p for the solution of Eq. (4.56). The dashed lines are the approximated functions for LHS of Eq. (4.56), while the solid lines are without the approximation.

$$\tanh(x) = \frac{e^{2x}-1}{e^{2x}+1} > \frac{1+2x-1}{1+2x+1} = \frac{x}{1+x} \tag{4.57}$$

We can approximate Eq. (4.56) as

$$\frac{\sqrt{k_\rho^2 - k_1^2}d}{\sqrt{k_\rho^2 - k_o^2 d + 1}} = \frac{\sqrt{k_\rho^2 - k_1^2}}{\mu_r \sqrt{k_\rho^2 - k_o^2}} \tag{4.58}$$

As shown in Fig. 4-15, the solution from the approximated Eq. (4.58) is greater than the the solution from Eq. (4.56). Upon solving Eq. (4.58), we can obtain the value for the estimated value for the pole k_p. In the actual implementation, we use $k_b = k_p + 1.2k_o$.

Similar procedure can be applied to ENG material. Rewriting the guidance condition as:

$$\tanh(\sqrt{k_\rho^2 - k_1^2}d) = -\frac{\epsilon_r\sqrt{k_\rho^2 - k_1^2}}{\sqrt{k_\rho^2 - k_o^2}} \tag{4.59}$$

we denote the left hand side of Eq. (4.59) as LHS_{ENG} and right hand side as RHS_{ENG}. The general shape of these values can be plotted out as shown in Fig. 4-16. Note that the

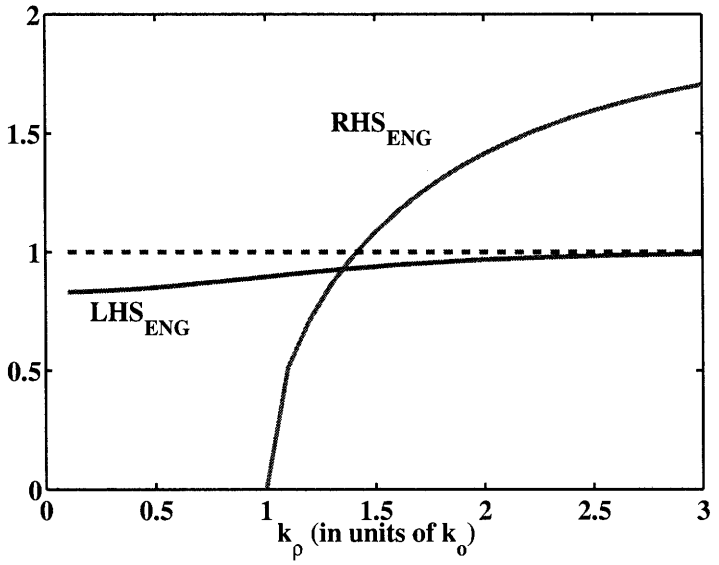

Figure 4-16: Illustration to show that the approximated function can be used to estimate the pole k_p for the solution of Eq. (4.59). The dashed lines are the approximated functions for LHS of Eq. (4.59), while the solid lines are without the approximation.

RHS_{ENG} is monotonically increasing with k_ρ which is different from the case of MNG. It is easy to see that if we approximate the LHS as 1, solution will have a value greater than the one from the original equation. Therefore the approximate equation becomes

$$1 = -\frac{\epsilon_r\sqrt{k_\rho^2 - k_1^2}}{\sqrt{k_\rho^2 - k_o^2}} \tag{4.60}$$

Upon solving, we get the approximate max k_ρ as

$$k_\rho \approx \frac{\sqrt{-k_1^2 - c_r^2 k_o^2}}{|c_r|^2 - 1} \tag{4.61}$$

For LHM slab, both TE and TM evanescent surface wave modes can exist. For TE mode we have the same equation as Eq. (4.56). THe left hand side and right hand side and the approximation as Eq. (4.58) can be plotted in Fig. 4-17 Notice that RHS can take two different shapes depending on the values of k_1^2. So both approximations need to be used to find k_p. The similar curves for TM evanescent modes are show in Fig. 4-18 The same situation happens in TM mode. So the solution will be to consider both approximations together in order to find the maximum k_p.

Once the half-elliptical path integration is determined, the remaining work is to evaluate the Sommerfeld tail integration. Referring to Fig. 4-1 for the illustration, the total number of intervals (ξ_i) is chosen as 10 with each interval equal to π/ρ. The number of integration points used in Gaussian Quadrature method in each interval is 200 (Better results can be obtained by using $(k_o\rho + 1)70$ as the number of points, which depends on the observation point.). The weighted-averages method is then used to extrapolate the final integration values. Referring to Eq. (4.40), the parameters values used are $p = 1$, $\zeta = |z_{obs} - z_{src}|$, $\alpha = 0.5$, $q = \pi/\rho$, where z_{obs} is the z axis value of the observation point and z_{src} is the z axis value of the source point.

In order to validate the above formulations, we calculate the fields due to HED on ground LHM slabs and compare the results with Microwave Studio (CST) simulation results. For the CST simulation, the slab domain has to be truncated so the fields are effec-

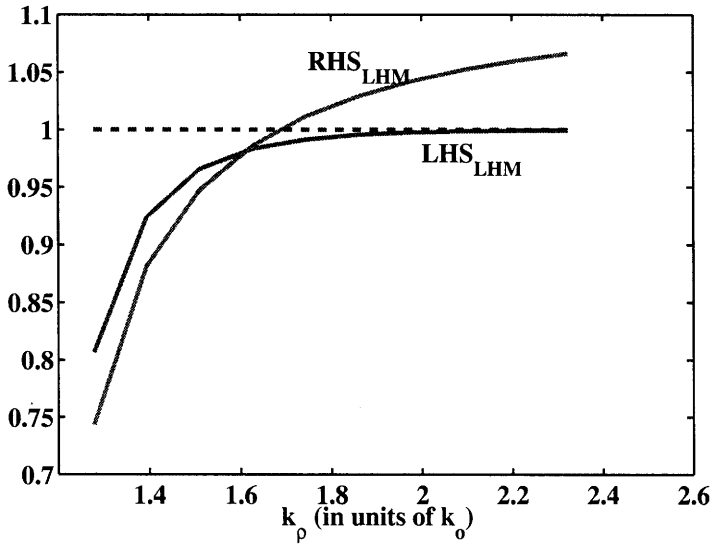

(a) Cases with $k_1^2 > k_o^2$

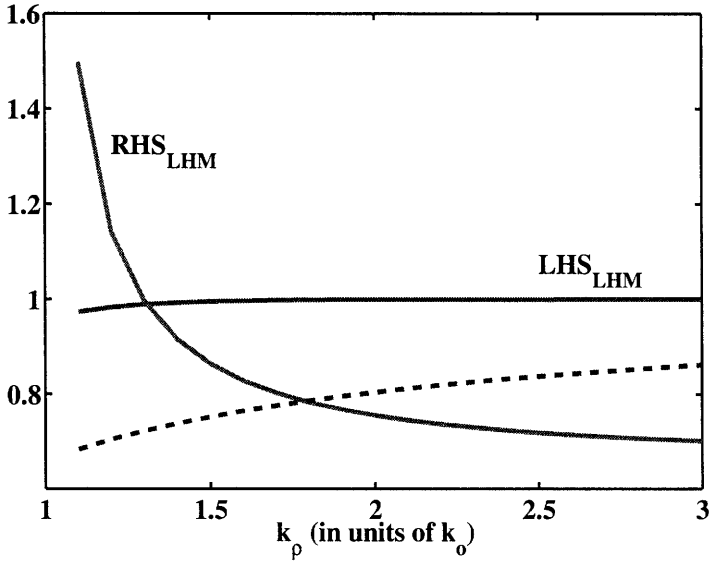

(b) Cases with $k_1^2 < k_o^2$

Figure 4-17: Illustration to show that the approximated solution of TE mode evanescent wave guidance condition for grounded LHM slabs. The dashed lines indicates the approximated solution, while the solid lines are for the actual solution.

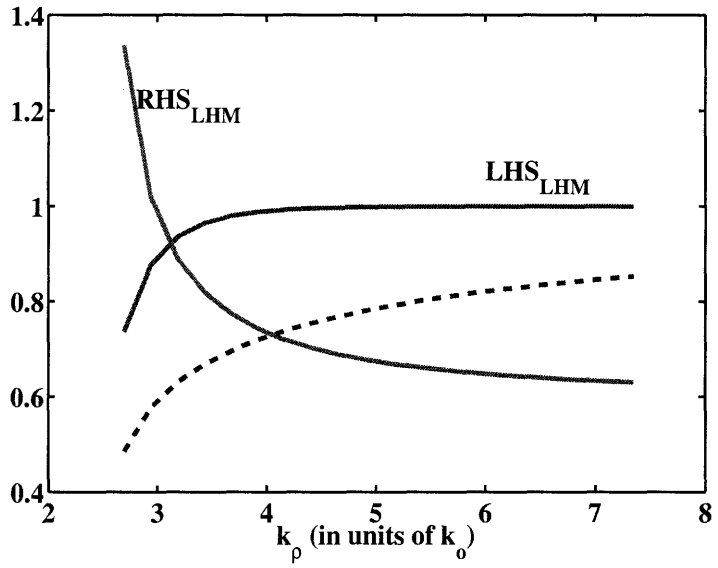

(a) Cases with $k_1^2 > k_o^2$

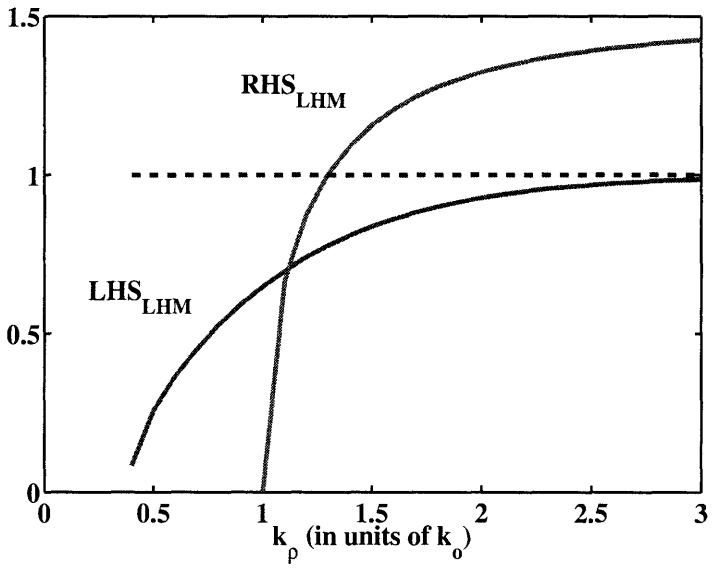

(b) Cases with $k_1^2 < k_o^2$

Figure 4-18: Illustration to show that the approximated solution of TM mode evanescent wave guidance condition for grounded LHM slabs. The dashed lines indicates the approximated solution, while the solid lines are for the actual solution.

tively due to finite slabs. By choosing the size of the slabs to be sufficiently large, it may be possible to obtain results close to the infinite slab's fields. As the first step, we compare the CST results and the analytical results with grounded RHM slabs which is shown in Fig. 4-19. Two cases are with and without TE surface wave modes since the TM modes always exist. It can be seen that two results are in good agreements .

We test the LHM slabs with the results shown in Fig. 4-20. Two cases in the two figures are one with TM surface wave modes and one with no surface wave modes. The effect of the modes can be seen at the higher field values at the same distance. Good agreements in the results validate the formulations we developed in this section.

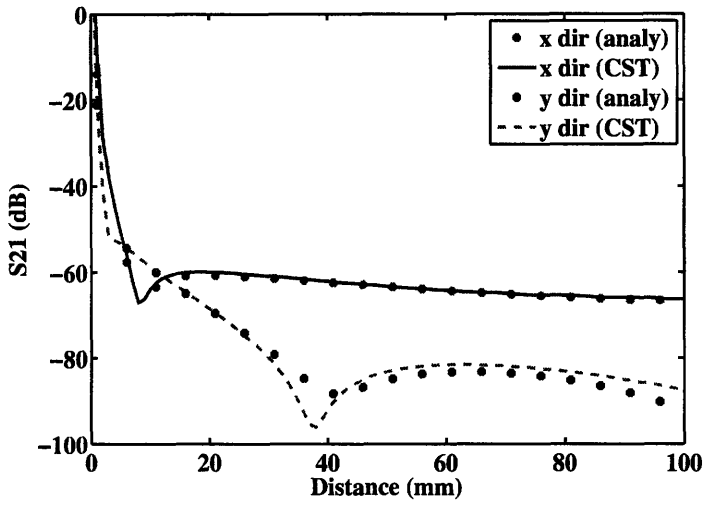

(a) RHM slab is 3 mm thick

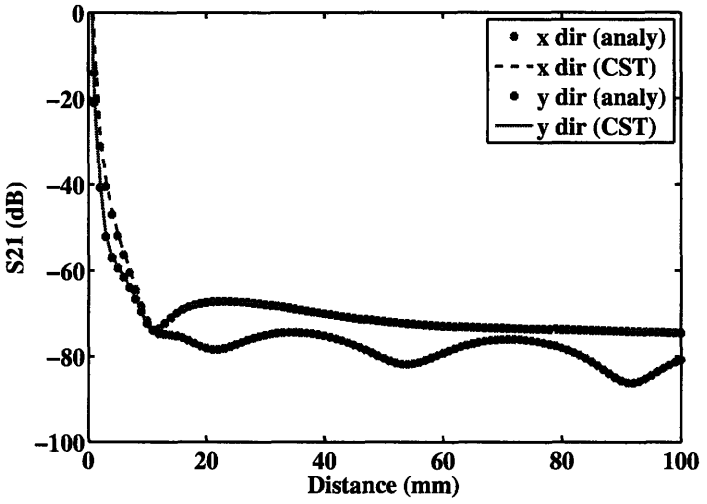

(b) RHM slab is 10 mm thick

Figure 4-19: Comparison between the Green's function method (analy) and the Microwave studio (CST) simulation results. A HED is placed on a grounded slab with (μ_r=2, ϵ_r=2) and the specified thickness. The source frequency is 10 GHz, and the fields are measured along the slab surface.

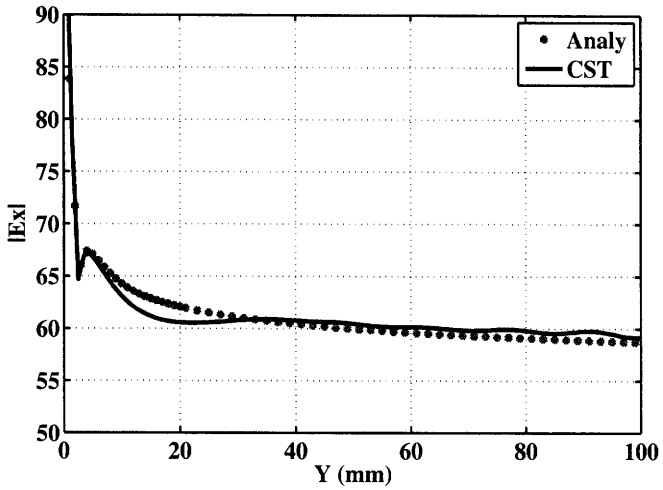

(a) LHM slab with (μ_r=-2, ϵ_r=-2)

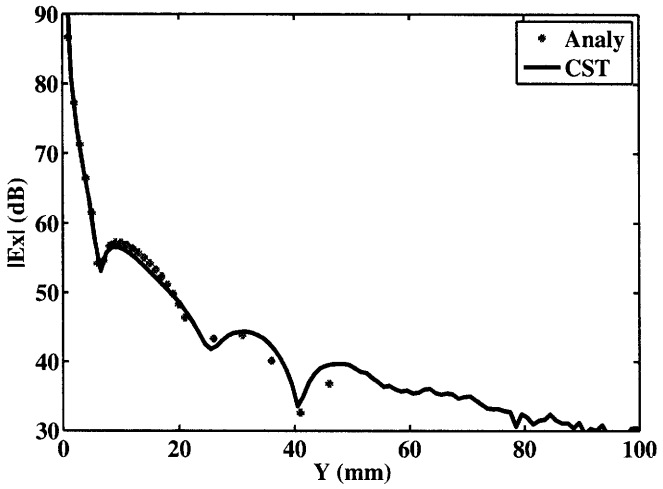

(b) LHM slab with (μ_r=-0.4, ϵ_r=-0.4)

Figure 4-20: Comparison between the Green's function method (analy) and the Microwave studio (CST) simulation results. A HED is placed on a grounded slab which is 3 mm thick with specified parameters. The source frequency is 10 GHz. and the fields are measured along the slab surface.

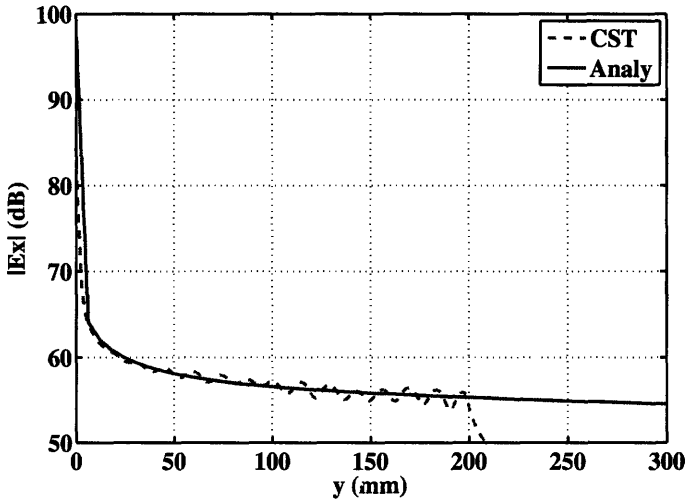

(a) MNG material

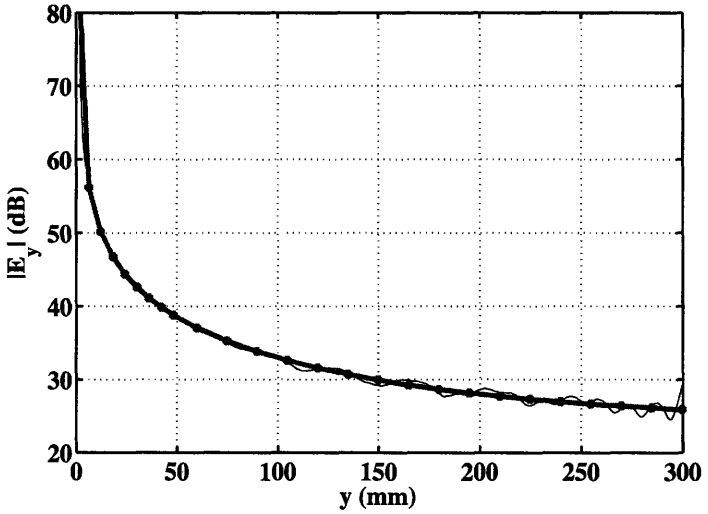

(b) ENG material

Figure 4-21: Comparison between the Green's function method (analy) and the Microwave studio (CST) simulation results. A HED is placed on a grounded slab with (a) MNG (μ_r=-10, ϵ_r=1) of a thickness of 3 cm (b) ENG (μ_r=1, ϵ_r=-10) with a thickness of 4 cm. The source frequency is 10 GHz, and the fields are measured along the slab surface.

4.4.4 Optimization Using Genetic Algorithm (GA)

Genetic Algorithm [80] is a global optimization technique based on the mechanism of natural selection. It starts by defining the variables, the cost function and cost, and ends by checking the convergence [81] . With the goal to minimize the cost function (a general purpose of any optimization method), the process [82] is to select only a portion of the total initial population (or initial guesses) which have a lower cost (or so called better fitness). In order to maintain the size of population, the new population is generated as "offsprings" of the selected population through the process of crossover and mutation. The process of selection is the process of optimization since only the best result (lower cost) is remained for the next generation. The process of crossover and mutation is the search process which has an advantage over conventional minimum seeking methods. Since GA doesn't require the knowledge of the gradient of the cost function, the method is very suited for a global optimization problem.

Since we have developed formulations to evaluate the fields on the grounded slabs, GA can be started by defining the cost function as

$$\text{Min:} \quad f = 20\log_{10} E_z(\mu, \epsilon, d)|_{\rho=10\lambda} \tag{4.62}$$

The cost function defines the variables in the optimization process. The search range of the variables are $\mu_r \in [-3,\ 1]$, $\epsilon_r \in [-3,\ 10]$, $d \in [0.1,\ 5]\ mm$. A binary GA code is used with the bits of 5,7,6 for μ_r, ϵ_r, d respectively. We choose the population size as 40. The probability of crossover as 0.8 and the probability of mutation as 0.03. For the convergence, we set the maximum repeated cost as 10, which means if the cost is not

changed for 10 generations, the search is stopped.

The optimization result is shown in Fig. 4-22

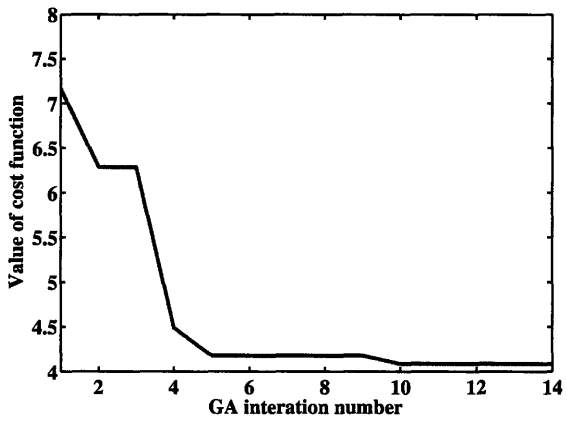

Figure 4-22: Plot of minimum cost of each generation in GA optimization for field isolation using a grounded slab.

The result for the optimized variables are in Table 4.6. For the purpose of comparison, the normalized values to air are shown in both the case of dipole in grounded slab and the case of horn antenna with grounded finite slab (as shown in Fig. 4-8). In addition to the GA optimized result, several slab parameters in each of the four material categories (*i.e.* RHM, LHM, MNG, ENG) are also evaluated for the coupling level. It can be seen that the GA optimized result gives the best isolation of all the materials presented. Due to the numerical dynamic range in CST, lower than -34 dB isolation is not able to be observed. The data also validate the choice of using dipole in infinite slabs as a simplified model for horn antenna coupling in finite slabs.

4.4.5 Asymptotic Formulation

The fields inside stratified media due to dipole sources can also be found using the plane wave expansion methods as presented in [42]. Using Sommerfeld identity, fields due to

Table 4.6: GA result of isolation using grounded slabs compared with other configurations. The data shown are values normalized to air case. The actual values for air case are in brackets.

μ_r	ϵ_r	$d(mm)$	Field coupling (dB)	CST (dB)	comments
-1.75	0.05	5	-42	- 34	GA result
1	1	4	0(46)	0 (-31)	air
1	2	4	+8	+9	RHM
0.1	0.1	4	-34	-33	
1	-0.1	4	-36	-34	ENG
1	-0.9	4	-20	-34	
-0.1	1	4	-16	-20	MNG
-0.9	1	4	-19	-25	
-0.1	-0.1	4	-34	-33	LHM
-0.1	-1	4	-36	-33	
-1	-0.1	4	-34	-33	
-10	-0.1	4	+3	-2	

a dipole can be decomposed into plane waves along the longitudinal axis of the layered media. For a single layer grounded slab, we set up the slab from $z = d_{-1}$ to $z = d_0$ with the ground plane at $z = d_{-1}$ (see Fig. 4-10). For a z directed dipole above the surface of the slab the electric field can be written as

$$E_z = \int_{-\infty}^{\infty} \mathrm{d}k_\rho H_0^{(1)} k_\rho \rho \begin{cases} A_{0+}e^{ik_{0z}z} + B_{0+}e^{-ik_{0z}z} & z > 0 \\ A_{0-}e^{ik_{0z}z} + B_{0-}e^{-ik_{0z}z} & d_0 < z \leq 0 \end{cases} \tag{4.63}$$

where the dipole is located at $z = 0$. The wavevector in air is k_0 and the wavevector in the slab is $k_1 = \omega\sqrt{\mu\epsilon}$. When the dipole is at the slab's boundary, $d_0 = 0$. Therefore, the second expression in Eq. (4.63) only has meaning at the limit when $d_0 \to 0$. This is important since the boundary condition at the slab surface will need to use this term to satisfy the continuity of electric flux $\overline{D}$.

The unknowns in Eq. (4.63) can be written as

$$\begin{cases} A_{0+} = A_{ved} + E_{ved}, \quad B_{0+} = 0 \\ A_{0-} = A_{ved}, \quad B_{0+} = E_{ved} \end{cases} \tag{4.64}$$

where E_{ved} is the field amplitude in free space due to a $\hat{z}$ dipole, which has the form of

$$E_{ved} = -\frac{Ilk_\rho^3}{8\pi\omega\epsilon_o k_{0z}}, \tag{4.65}$$

A_{ved} is the field amplitude due to the presence of the grounded slab.

Applying the reflection coefficient formula for layered media [42], we have the expression for R_{0-}^{TM} as

$$R_{0-}^{TM} = \frac{A_{0-}}{B_{0-}} = \frac{e^{-i2k_{0z}d}}{R_{01}^{TM}} + \frac{[1-(1/R_{01}^{TM})^2]e^{-i2(k_{0z}+k_{(1)z}d_0)}}{(1/R_{01})e^{-i2k_{(1)z}d_0} + (A_1/B_1)} \tag{4.66}$$

Plugging the expression for A_1/B_1

$$\frac{A_1}{B_1} = e^{-i2k_{(1)z}d_1} \tag{4.67}$$

into Eq. (4.66), and realizing that [42]

$$A_{0+} = (1 + R_{0-}^{TM})E_{ved}, \tag{4.68}$$

we can then solve for the unknown A_{0+} as

$$A_{0+} = -\frac{\mathrm{I}lk_\rho^2\epsilon_1}{4\pi\omega\epsilon_0(\epsilon_0 k_{1z} + \epsilon_1 k_{0z})}\frac{1+e^{i2k_{1z}d}}{1+R_{01}^{TM}e^{i2k_{1z}d}} \tag{4.69}$$

where $d = d_{-1} - d_0$ is the thickness of the slab.

So the longitudinal electric field at the slab boundary is

$$E_z = \int_{-\infty}^{+\infty} \mathrm{d}k_\rho A_{0+} H_0^{(1)}(k_\rho\rho) \tag{4.70}$$

For fields far away from the source, the asymptotic formula for $II_0^{(1)}(k_\rho\rho)$ can be used to simplify the integration so we have

$$E_z \approx \int_{-\infty}^{+\infty} \mathrm{d}k_\rho A_{0+}\sqrt{\frac{2}{k_\rho\rho\pi}}e^{i(k_\rho\rho-\pi/4)} \tag{4.71}$$

The classic way to evaluate this integral is to transform the integrand from k_ρ plane to α plane using $k_\rho = k\sin\alpha, k_z = k\cos\alpha$. As shown in [42], the multiple Riemann sheets overlapping in k_ρ plane become one sheet on α plane, which greatly simplifies the analysis. Due to the rapid oscillatory behavior of the integrand, the saddle point method is use to evaluate the integral and the result is

$$E_z = \frac{iIlk_\rho^3\epsilon_1}{4\pi\omega\epsilon_0}\frac{1+e^{i2k_{1z}d}}{1+R_{01}^{TM}e^{i2k_{1z}d}}\frac{2}{\epsilon_0 k_{1z}+\epsilon_1 k_{0z}}\sqrt{\frac{k_1}{k_\rho}}\frac{e^{ik_1 r}}{k_1 r}k_1\cos\theta \tag{4.72}$$

where $k_{1z} = k_1\cos\theta$, $k_\rho = k_1\sin\theta$ and $k_{0z} = \sqrt{k_0^2 - k_\rho^2}$.

When the observation point is at the slab boundary, $\theta = 90°$ so Eq. (4.72) is zero which

means the saddle point contribution to the integral is zero and the second order contribution, the branch cut contribution (as shown in Fig. 4-23), needs to be considered.

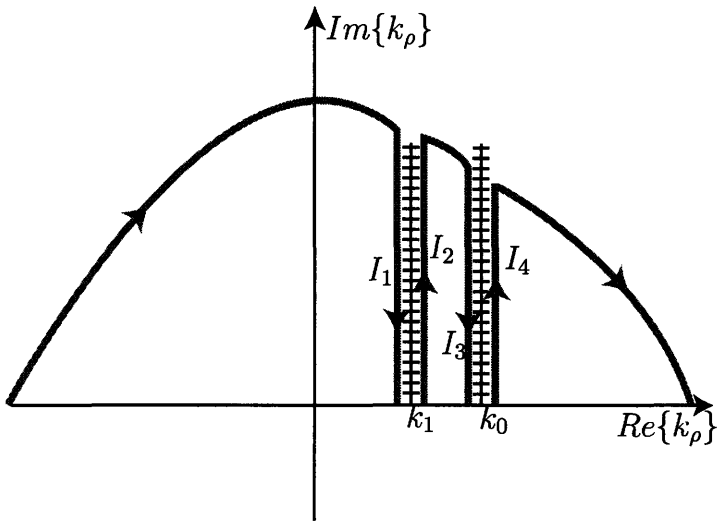

(a)

Figure 4-23: Illustration of integration path for branch cuts

A careful analysis shows that only k_0 is the real branch point.A_{0+} is an even function of k_1 so k_1 is not a branch point. The integrand summation along the two branch paths for k_0 becomes

$$\begin{aligned} A_{0+}|_{I_3} + A_{0+}|_{I_4} &= -A_{0+}(k_{0z})|_{I_3} + A_{0+}(-k_{0z})|_{I_4} \\ &= \frac{Ilk_\rho^2\epsilon_1}{4\pi\omega\epsilon_0}\left[\frac{1+e^{i2k_{1z}d}}{\epsilon_0 k_{1z}+\epsilon_1 k_{0z}}\right]^2 \frac{2\epsilon_1 k_{0z}}{(1+R_{01}^{i2k_{1z}d})(R_{01}+e^{i2k_{1z}d})} \end{aligned} \quad (4.73)$$

Therefore, the integral of Eq. (4.70) can be obtained as

$$\begin{aligned} E_z &\approx i\int_0^{\infty} dq(A_{0+}|_{I_3} + A_{0+}|_{I_4})\sqrt{\frac{2}{k_\rho \rho \pi}}e^{ik_\rho \rho}e^{-i\pi/4} \\ &= \frac{-Ilk_0^2\epsilon_1^2}{2\pi\omega\epsilon_0}\left[\frac{1+e^{i2k_{1z}d}}{\epsilon_0 k_{1z}(1-e^{i2k_{1z}d})}\right]^2 \frac{e^{ik_0\rho}}{\rho^2} \end{aligned} \tag{4.74}$$

where $k_{1z} = \sqrt{k_1^2 - k_0^2}$. More detailed derivation can be seen in Appendix D.

It can be concluded that the saddle point contribution gives rise to the dependence of $1/\rho$ while the contribution from the branch cuts gives rise to $1/\rho^2$. So the decay on the slab boundary is much faster than the fields in the space. When the surface wave modes exist the fields become (for the pole at k'_ρ)

$$E_z = 2\pi i(k_\rho - k'_\rho)A_{o+}(k\rho)\sqrt{\frac{2}{k_\rho \rho \pi}}e^{i(k_\rho \rho - \pi/4)}\Big|_{k_\rho = k'_\rho} \tag{4.75}$$

Hence the surface wave contributes the $1\sqrt{\rho}$ dependence.

Validation of the asymptotic expression has been carried out on all four types of materials, namely RHM, LHM, MNG, ENG. The asymptotic results are compared with the fields evaluated from the analytical code. For RHM, the results are shown in Fig. 4-24. It can be seen that in the observation distance from 5λ to 10λ, the actual field (E_z) value deviates from the asymptotic value at 5 λ, but the two values gradually approaches each other and the agreement is excellent close to 10λ. In terms of the level of field amplitudes, the slab with smaller constitutive parameters has lower fields at the same distance. For LHM slabs, the comparison is shown in Fig. 4-25, while for MNG and ENG slabs, the results are in Fig. 4-26. Same observation can be made with these cases.

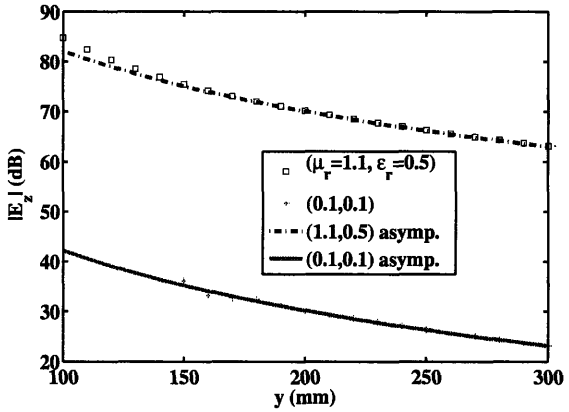

Figure 4-24: Validation of asymptotic formula for $\hat{z}$ directed electric dipole on a grounded RHM slab. The slab is with a 4 mm thickness. The dipole source is at y=0 mm with a frequency of 10 GHz. The measurement range is from 5λ to 10λ.

We are now able to use the Eq. (4.74) to design a slab for the best isolation. For the purpose of the slab design, we can ignore the constant parameters and directly use

$$E_z \propto \left| \frac{\epsilon_{1r}(1+e^{i2k_{1z}d})}{k_{1z}(1-e^{i2k_{1z}d})} \right| = \left| \frac{\epsilon_{1r}}{\sqrt{k_0^2-k_1^2}\tanh(\sqrt{k_0^2-k_1^2}d)} \right| \tag{4.76}$$

Therefore, in order to get lower E_z, we need to increase $|k_{1z}|$ and reduce ϵ_{1r}. Since $k_{1z} = \sqrt{k_1^2-k_0^2}$, for RHM and LHM slabs, the maximum k_{1z} can be achieved is k_0. However for MNG slabs, the maximum k_{1z} can be greater than k_0 since k_1^2 is a negative number. So the slab offers the best isolation is to use MNG with maximum $|k_1|$ and minimum ϵ_{1r}. The result from GA optimization agrees with this conclusion.

We shall also remark on the distance dependence aspect of the isolation study. It is intuitive to see that as the antennas are positioned closer, the coupling level will increase (i.e. poorer isolation). This increase of coupling level as a function of distance will depend on the slab parameters. Observing from Fig. 4-19, Fig. 4-20 and Fig. 4-21, we note that the sharp increase in the coupling level usually occurs in less than 1 λ distance away from

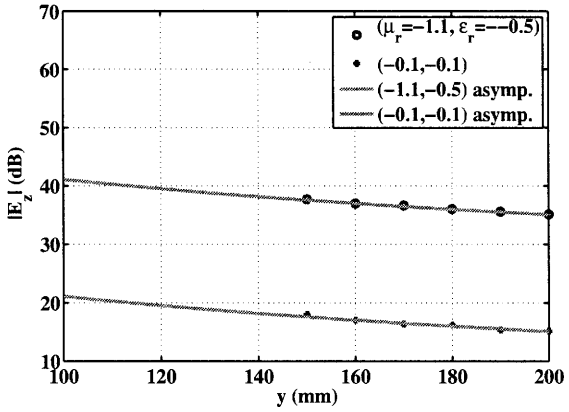

Figure 4-25: Validation of asymptotic formula for $\hat{z}$ directed electric dipole on a grounded LHM slab. The slab is with a 4 mm thickness. The dipole source is at y=0 mm with a frequency of 10 GHz. The measurement range is from 5λ to 10λ.

the source. Therefore, it is recommended that the antennas should be kept away from each other for a minimum 1 λ distance while the further away the separation, the better isolation can be achieved.

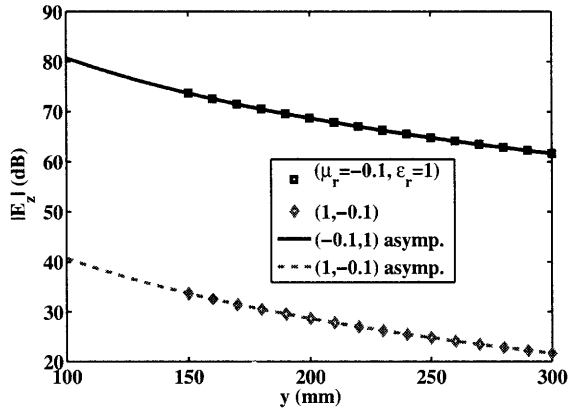

Figure 4-26: Validation of asymptotic formula for $\hat{z}$ directed electric dipole on a grounded MNG and ENG slab. The slab is with a 4 mm thickness. The dipole source is at y=0 mm with a frequency of 10 GHz. The measurement range is from 5λ to 10λ.

4.5 Antenna Isolation In Layered Grounded Slabs

In this section, we investigate the isolation design using 5-layered slab structures. The configuration is shown in Fig. 4-27. The parameters to design are each layer's constitutive parameters and the thickness. Since the asymptotic expression for the field is very complicated to derive, GA method is preferred. It is understood that a 5-layered structure may not be necessary in practice. However for the purpose of testing the capability of the method, it is a legitimate choice due to its sufficient complexity. The parameter range for the variables are kept the same as the one in single layer case. Also the same cost function as Eq. (4.62) is adopted. The convergence of GA method is shown in Fig. 4-28.

The final result of 5 layer slab configuration is shown in Table 4.7. The results from two GA runs are slightly different, but the resulting field coupling level is almost the same. As expected, GA optimization result shows that the best isolation can be achieved by using MNG layers for all the 5 layers. Since the dipole is placed on the first layer surface, the result for the first layer is very similar to the single layer case. We find large negative μ, close to zero ϵ and large thickness d for the first layer. This example shows that GA method is versatile and can be directly applied to multilayered media design when used with the spectral domain Green's function method for the field evaluation.

Table 4.7: GA result of isolation using 5-layered slabs

layer	μ_r	ϵ_r	d(mm)
1	-2.8	0.5	4.4
2	-0.5	6.6	4.7
3	-1.7	6.1	3.3
4	-1.0	9.1	4.7
5	-2.9	6.4	2.8

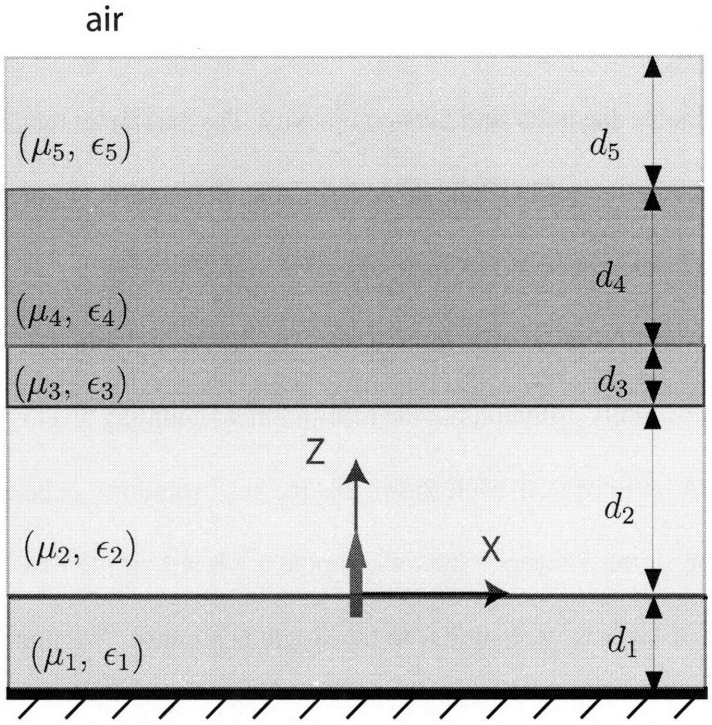

(a)

Figure 4-27: Setup of 5-layered slab with $\hat{z}$ directed electric dipole. Genetic Algorithm is used to optimize the slab parameters for the best antenna isolation.

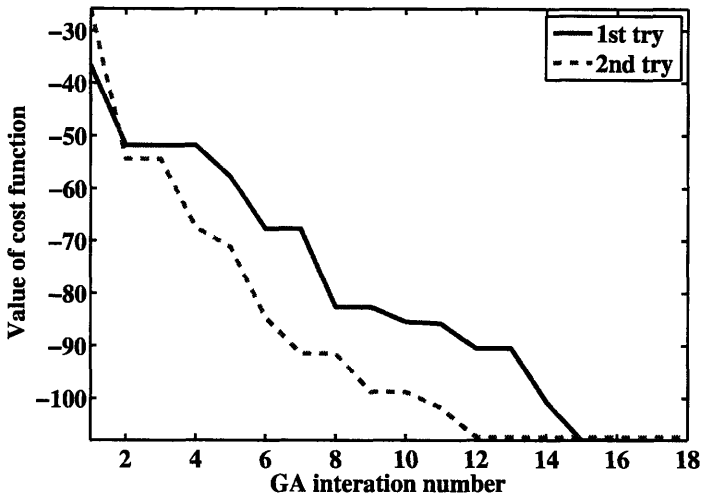

Figure 4-28: Plot of minimum cost of each generation in GA optimization for field isolation using a grounded 5-layered slab.

4.6 Conclusions

We demonstrate an antenna isolation design example is provided with a z directed dipole antenna. Two different approaches are used to find the optimum slab parameters for the isolation. One approach is to use Genetic Algorithm (GA) to optimize the slab's constitutive parameters and the thickness for a minimum coupling level. The other approach is to develop an analytic asymptotic expression for the field, and then uses the expression to design the slab parameters for the best isolation. Both results agree well. Finally, possibility of using multi-layered media in place of the slab for the antenna isolation is studied. GA method is used to search for the optimization design solution. We show that GA converges very fast to the solution and the result yields satisfactory isolation for the antennas.

Chapter 5

Conclusion

The reflection properties of the LHM slabs are studied on the GH lateral shift phenomena. We show theoretically that the GH lateral shift of a Gaussian beam can be both positive and negative at different incident angles with a single LHM slab. The relation between the slab parameters and the GH shift directions is illustrated in an analytical expression. Applying this expression, we further show that there are in general three different cases in which GH lateral shift can change directions with the incident angle. In addition, methods are developed to accurately simulate the GH lateral shifts using FDTD. Good agreements are achieved comparing the simulation results and the analytical results. Furthermore, using the derived expression for GH lateral shift direction, we explain the physical reason for the phenomena. It turns out that it is due to the energy flux line pattern changes inside the slabs. The relative amplitude of the growing and decaying evanescent waves changes inside the slab as function of slab parameters and the incident angle of Gaussian beams. The negative shifts are the results of decaying evanescent wave dominates inside the slab, and the positive shifts are due to growing evanescent waves. It is concluded that the unique

ability of LHM slabs to amplify evanescent waves, already used for the design of a perfect lens, is responsible for the GH shift direction change.

The transmission properties of the LHM slabs are studied on the imaging effects. In developing the numerical tool -FDTD- for simulating the imaging using LHM slabs, we find that the imaging resolution can be limited by the numerical simulation due to the mismatch between the slab and its surrounding media. By studying the constitutive parameters in the FDTD implementation, it is found that the mismatch is due to the time discretization rather than space discretization. By comparing the simulation results and analytical calculations, we demonstrate that the simulated image resolution of an LHM perfect lens is mainly limited by this mismatch. In other applications such as the simulation study of surface plaritons at LHM/RHM interfaces where the matching condition is required, the understanding of this limitation in FDTD can also be very important. Imaging properties of finite-size LHM slabs are also analyzed. In particular, we use an approximate analytical method to study the effect of the finite size by considering only the aperture. It is shown that the approximated current sheet with a Gaussian shape truncated at the aperture reproduces the key features of the image spectrum. Hence the method can be used as a fast alternative to numerical simulations, although the simulations are still needed for a better accuracy. Furthermore, we explain that the negative energy stream at the image plane come from the inherent spectrum of the source, and more precisely from interactions between propagating waves and amplified evanescent waves from LHM slabs. This phenomenon does not depend on the finite size of the slab. We show that once again the capability of amplifying evanescent waves by LHM slabs make possible this unique property.

The properties of multi-layered media structure are studied for the application of an-

tenna isolations. We extend the traditional spectral domain Green's function method to include media like LHM, MNG and ENG materials. Comparison with results from CST simulations are used to validate the method. For practical considerations, we demonstrate a design example using grounded slabs for reducing the coupling from a $\hat{z}$ directed dipole antenna. Two different approaches are used to find the optimum slab parameters for the best isolation. One approach is to use Genetic Algorithm (GA) to optimize the slab's constitutive parameters and the thickness for a minimum coupling level. The other approach is to develop an analytic asymptotic expression for the field, and then used the expression to design the slab parameters for the best isolation. Both results agree well. Finally, possibility of using multi-layered media in place of the slab for the antenna isolation is studied. GA method is used to search for the optimization design solution. We show that GA converges very fast to the solution and the result yields satisfactory isolation for the antennas.

Appendix A

GH Lateral Shift Formulation

The incident Gaussian beam (TE polarization) in region #1 (refer to Fig. 2-1):

$$E_{iy} = \int_{-\infty}^{\infty} dk_x \exp[i(k_x x + k_{1z} z)]\psi(k_x) \tag{A.1}$$

where,

$$\psi(k_x) = \frac{g}{2\sqrt{\pi}} \exp[-g^2(k_x - k_{ix})^2/4]$$

In region 1, the reflected electric field can be expressed as:

$$E_{1y}^r = \int_{-\infty}^{\infty} dk_x R e^{ik_x x} e^{-ik_{1z} z} \psi(k_x) \tag{A.2}$$

In region 2 and 3, the total electric field can be expressed as:

$$E_{2y} = \int_{-\infty}^{\infty} dk_x (Ae^{ik_{2z}z} + Be^{-ik_{2z}z}) e^{ik_x x} \psi(k_x) \tag{A.3}$$

$$E_{3y} = \int_{-\infty}^{\infty} dk_x T e^{ik_x x} e^{ik_{3z}z} \psi(k_x) \tag{A.4}$$

The coefficients can be obtained by phase matching and boundary conditions:

$$R = \frac{R_{12} + R_{23}e^{i2k_{2z}d}}{1 + R_{12}R_{23}e^{i2k_{2z}d}}, \qquad T = \frac{4e^{i(k_{2z}-k_{3z})d}}{(1+p_{12})(1+p_{23})(1+R_{12}R_{23}e^{i2k_{2z}d})}$$

$$A = \frac{2}{(1+p_{12})(1+R_{12}R_{23}e^{i2k_{2z}d})}, \qquad B = \frac{2R_{23}e^{i2k_{2z}d}}{(1+p_{12})(1+R_{12}R_{23}e^{i2k_{2z}d})}$$

where

$$R_{12} = \frac{1-p_{12}}{1+p_{12}}, \quad R_{23} = \frac{1-p_{23}}{1+p_{23}}, \quad p_{12} = \frac{\mu_1 k_{2z}}{\mu_2 k_{1z}}, \quad p_{23} = \frac{\mu_2 k_{3z}}{\mu_3 k_{2z}}$$

With the incident angle above the critical angle for both media #2 and #3, we choose

$$k_{2z} = (k_2^2 - k_x^2)^{1/2} = i\alpha_{2z}, \quad k_{3z} = (k_3^2 - k_x^2)^{1/2} = i\alpha_{3z} \tag{A.5}$$

and define

$$C = B/A = R_{23}e^{-2\alpha_{2z}d} \tag{A.6}$$

as the ratio of growing and decaying evanescent wave amplitudes inside the slab.

If the reflection coefficient R is expressed as: $R = |R|e^{i\Phi(k_x)}$, then the lateral shift can be characterized by : $S = -\frac{\partial \Phi}{\partial k_x}|_{k_x = k_{ix}}$ and

$$\Phi = -2\tan^{-1}\frac{p_{12}(1-R_{23}e^{-2\alpha_{2z}d})}{1+R_{23}e^{-2\alpha_{2z}d}} = -2\tan^{-1}F, \quad \text{where} \quad F = \frac{p_{12}(1-C)}{(1+C)} \tag{A.7}$$

Taking advantage of

$$sign\{S\} = sign\{-\frac{\partial\Phi}{\partial k_x}\} = sign\{\frac{\partial F}{\partial k_x}\} \tag{A.8}$$

we can write (when $|C| \neq \infty$)

$$\begin{aligned} sign\{\frac{\partial F}{\partial k_x}\} &= sign\{\frac{\partial p_{12}}{\partial k_x}(1-C^2) - 2p_{12}\frac{\partial C}{\partial k_x}\} \\ &= sign\{\frac{\mu_{1r}}{\mu_{2r}}\big[1-C^2+\frac{4\alpha_{2z}dk_{1z}^2}{k_1^2-k_2^2}C - \frac{4\alpha_{2z}}{\alpha_{3z}}\frac{(k_2^2-k_3^2)\mu_{2r}\mu_{3r}}{(\mu_{3r}^2\alpha_{2z}^2-\mu_{2r}^2\alpha_{3z}^2)}\frac{k_{1z}^2}{k_1^2-k_2^2}C\big]\} \end{aligned}$$

If $|C| = \infty$ (when $\mu_{3r}\alpha_{2z} + \mu_{2r}\alpha_{3z} = 0$),

$$sign\{\frac{\partial F}{\partial k_x}\} = sign\{-\mu_{1r}\mu_{2r}\left[(k_1^2-k_2^2)\alpha_{3z}^2e^{-2\alpha_{2z}d} - (k_2^2-k_3^2)k_{1z}^2\right]\}$$

If we let

$$U \equiv \frac{\alpha_{2z}k_{1z}^2}{k_1^2-k_2^2} \qquad V \equiv d - \frac{(k_2^2-k_3^2)\mu_{2r}\mu_{3r}}{\alpha_{3z}(\mu_{3r}^2\alpha_{2z}^2-\mu_{2r}^2\alpha_{3z}^2)} \tag{A.9}$$

Then

$$\begin{aligned} sign\{S\} &= sign\{\frac{\partial F}{\partial k_x}\} = sign\{\frac{\mu_{1r}}{\mu_{2r}}\left[1-C^2+4UVC\right]\} \\ &= sign\{-\frac{\mu_{1r}}{\mu_{2r}}\left[C-C_1\right]\left[C-C_2\right]\} \end{aligned}$$

where

$$C_1 = 2UV + \sqrt{4U^2V^2 + 1}$$

$$C_2 = 2UV - \sqrt{4U^2V^2 + 1}$$

If $V > 0$ and $U > 0$

$$C_1 = 2UV + \sqrt{4U^2V^2 + 1} > 2UV + |1 - 2UV| >= 1$$

$$C_1 < 2UV + (1 + 2UV) = 1 + 4UV$$

$$C_2 = 2UV - \sqrt{4U^2V^2 + 1} > 2UV - (1 + 2UV) = -1$$

$$C_2 < 2UV - 2UV = 0$$

therefore $1 + 4UV > C_1 > 1$

$0 > C_2 > -1$

If $V \leq 0$ and $U > 0$

$$1 \geq C_1 > 0$$

$$-1 \geq C_2 \geq -1 + 4UV$$

We conclude that (1) There exist three value ranges for C: $C > C_1$, $C_1 > C > C_2$ and $C_2 > C$, (2) When GH lateral shift direction is altered, the value of C will change from one value range to another.

Appendix B

FDTD Simulation of Evanescent Waves

For numerical methods, the primary concerns are usually the accuracy and stability, while the computation expense of time and memory are of the secondary. In the presense of LHM, the ability to model evanescent waves accurately becomes very important since many unique phenomena are associated with evanescent waves. Therefore we present the study of FDTD on evanescent wave simulations.

B.1 Stability Condition

The conventional way to derive the stability condition is to separate the update equations into time domain and spatial domain, calculate the eigenvalues int these two domains separately and obtain the condition by letting the space domain eigenvalues to be within the ones in time domain.

Here we take a different approach. The method we use is to treat FDTD as an initial value problem and systemmetically derive the stability condition. With the time domain

and spatial domain equation coupled together. Therefore this new approach provides a better insight to the stability of the FDTD stability.

It is easy to show that 2D FDTD update equations can be rewritten in the matrix form as

$$\begin{bmatrix} E_y^{n+\frac{1}{2}} \\ H_x^n \\ H_z^n \end{bmatrix} = \overline{\overline{G}} \begin{bmatrix} E_y^{n-\frac{1}{2}} \\ H_x^{n-1} \\ H_z^{n-1} \end{bmatrix}$$

$$\overline{\overline{G}} = \begin{pmatrix} 1 - \frac{a^2}{\mu\epsilon} - \frac{b^2}{\mu\epsilon} & i\frac{a}{\epsilon} & -i\frac{b}{\epsilon} \\ i\frac{a}{\mu} & 1 & 0 \\ -i\frac{b}{\mu} & 0 & 1 \end{pmatrix}$$

$$a = 2\sin(\frac{k_z\Delta z}{2})\frac{\Delta t}{\Delta z}, \qquad b = 2\sin(\frac{k_x\Delta x}{2})\frac{\Delta t}{\Delta x}$$

Note that the field vectors on the left hand side are the fields at next time step which can be updated from the fields at current time step through a multiplication of the matrix $\overline{\overline{G}}$. The same matrix $\overline{\overline{G}}$ can be mulitipled again for the continuous update. So in order for this initial value problem to be stable, the eigenvalues of $\overline{\overline{G}}$ must be less or equal to one which means

$$|\lambda_i| \leq 1$$

Two of the eigenvalues are equal to one. The third eigenvalue is

$$|\lambda_3| = |1 - \frac{(\frac{a^2+b^2}{\mu\epsilon}) \pm \sqrt{(\frac{a^2+b^2}{\mu\epsilon})^2 - 4(\frac{a^2+b^2}{\mu\epsilon})}}{2}| \leq 1$$

case(a) if $\frac{a^2+b^2}{\mu\epsilon} > 4$ then

$$\frac{(\frac{a^2+b^2}{\mu\epsilon}) \pm \sqrt{(\frac{a^2+b^2}{\mu\epsilon})^2 - 4(\frac{a^2+b^2}{\mu\epsilon})}}{2} > 2 \tag{B.1}$$

which means $\lambda_3 > 1$. That is not allowed for the solution.

case(b) if $\frac{a^2+b^2}{\mu\epsilon} \leq 4$ then $\sqrt{(\frac{a^2+b^2}{\mu\epsilon})^2 - 4(\frac{a^2+b^2}{\mu\epsilon})}$ is an imaginary number. Therefore

$$\begin{aligned} |\lambda_3| &= \frac{1}{2}|2 - (\frac{a^2+b^2}{\mu\epsilon}) \pm \sqrt{(\frac{a^2+b^2}{\mu\epsilon})^2 - 4(\frac{a^2+b^2}{\mu\epsilon})}| \\ &= \frac{1}{2}\sqrt{(2 - (\frac{a^2+b^2}{\mu\epsilon}))^2 - (\frac{a^2+b^2}{\mu\epsilon})^2 - 4(\frac{a^2+b^2}{\mu\epsilon})} \\ &= 1 \end{aligned} \tag{B.2}$$

which means the requirement for stability condition is met. So the stability condition can be satisfied by letting

$$\frac{a^2+b^2}{\mu\epsilon} \leq 4 \tag{B.3}$$

Using this condition, for plane waves, we get

$$0 \leq \sin^2(\frac{k_z \Delta z}{2})(\frac{\Delta t}{\Delta z})^2 + \sin^2(\frac{k_x \Delta x}{2})(\frac{\Delta t}{\Delta x})^2 \leq \frac{1}{c^2} \tag{B.4}$$

which is the same result as the one in standard FDTD references.

For evanescent waves, we have

$$0 \leq \sin^2(\frac{k_x \Delta x}{2})(\frac{\Delta t}{\Delta x})^2 - \sinh^2(\frac{\alpha_z \Delta z}{2})(\frac{\Delta t}{\Delta z})^2 \leq \frac{1}{c^2} \tag{B.5}$$

B.2 Numerical Dispersion

Numerical dispersion concerns with the deviation of the dispersion relation in the numerical domain. The expression for the plane wave can be directly adapted for evanescent waves by letting $k_z = i\alpha_z$, we the have the following dispersion relation:

$$\left[\frac{1}{c\Delta t}\sin(\frac{\omega \Delta t}{2})\right]^2 = \left[\frac{1}{\Delta x}\sin(\frac{k'_x \Delta x}{2})\right]^2 - \left[\frac{1}{\Delta z}\sinh(\frac{\alpha'_z \Delta z}{2})\right]^2 \tag{B.6}$$

B.3 Material Implementation

The numerical implementation of the material is illustrated with effective ϵ (the derivation for μ is similar). We start with the update equation

$$\frac{\partial \overline{J_e}}{\partial t} + \Gamma_e \overline{J_e} = \epsilon_o \omega_{pe}^2 \overline{E_y} \tag{B.7}$$

$$\oint \mathrm{d}\bar{l}\overline{H} = \frac{\partial}{\partial t}\oint \mathrm{d}\bar{s}\epsilon_o \overline{E_y} + \oint \mathrm{d}\bar{s}\overline{J_e} \tag{B.8}$$

Expanding Eq. (B.7) in finite difference form, we can obtain

$$J_e \frac{-i2\sin(\omega\Delta t/2)}{\Delta t} + \Gamma_e J_e \cos(\omega\Delta t/2) = \epsilon_o \omega_{pe}^2 E_y \tag{B.9}$$

If we assume Γ_e=0 in the simulation, then the above equation becomes

$$J_e = \frac{\Delta t \omega_{pe}^2 \epsilon_o}{-i2\sin(\omega\Delta t/2)} E_y \tag{B.10}$$

Pluging this equation to Eq. (B.8), we can get

$$\epsilon_o E_y \frac{\Delta t \omega_{pe}^2 \epsilon_o}{-i2\sin(\omega\Delta t/2)} = \epsilon_1 E_y \tag{B.11}$$

Eliminating E_y, we have the following expression for the effective ϵ in the numerical implemention of Drude model

$$\epsilon = \epsilon_o \left(1 - \frac{\omega_{pe}^2}{4\sin(\omega_o \Delta t/2)/(\Delta t)^2}\right) \tag{B.12}$$

which is same as Eq. (3.6).

Appendix C

Derivation of Finite Slab Fields from Huygen's Principle

Electric field from a line source can be written as:

$$\overline{E}(x,z)_{ln} = \hat{y}\frac{-\omega\mu_o}{4}H_0^{(1)}(k_o|\rho|) = \hat{y}\frac{-\omega\mu_o}{4\pi}\int_{-\infty}^{\infty}\mathrm{d}k_z\frac{1}{k_x}e^{ik_x|x|}e^{ik_z z}$$

At the slabs boundary the fields are:

$$\begin{aligned} E_y(z) &= \frac{-\omega\mu_o}{4\pi}\int_{-\infty}^{\infty}\mathrm{d}k_z\frac{T(k_z)}{k_x}e^{ik_x d_2}e^{ik_z z} \\ H_z(z) &= \frac{-1}{4\pi}\int_{-\infty}^{\infty}\mathrm{d}k_z T(k_z)e^{ik_x d_2}e^{ik_z z} \end{aligned}$$

where the transmission coefficient $T(k_z)$ is

$$T(k_z) = \frac{4e^{ik_x d_1}e^{i2k_{1x}(d_2-d_1)}}{(1+p_{12})(1+p_{23})(1+R_{12}R_{23}e^{i2k_{1x}(d_2-d_1)})}$$

The next step is to find the fields at the image plane. Referring to Fig. 3-5, we first find the equivalent currents from the fields at the slab boundary and then use Stratton-Chu formula to write the fields at the image region as:

$$\begin{aligned}
\overline{E}(x,z) &= \iint_{S'} \mathrm{d}S' \left\{ i\omega\mu_o[\hat{n}\times\overline{H}(\overline{r}')]g(\overline{r},\overline{r}') \right. \\
&\qquad \left. +[\hat{n}\cdot\overline{E}(\overline{r}')]\nabla' g(\overline{r},\overline{r}') + [\hat{n}\times\overline{E}(\overline{r}')]\times\nabla' g(\overline{r},\overline{r}') \right\} \\
&= \hat{y}\int_{-\infty}^{\infty}\mathrm{d}z'\frac{i\omega\mu_o}{4\pi}\int_{-\infty}^{\infty}\mathrm{d}k_z T(k_z)e^{ik_x d_2}e^{ik_z z'} \\
&\qquad \frac{i}{4}H_0^{(1)}(k_o\sqrt{(z-z')^2+x^2}) \\
&+ \hat{y}\int_{-\infty}^{\infty}\mathrm{d}z'\frac{-\omega\mu_o}{4\pi}\int_{-\infty}^{\infty}\mathrm{d}k_z \frac{T(k_z)}{k_x}e^{ik_x d_2}e^{ik_z z'} \\
&\qquad \frac{\partial}{\partial x'}\frac{i}{4}H_0^{(1)}(k_o\sqrt{(z-z')^2+(x-x')^2})|_{x'=0} \\
&= \hat{y}E_1 + \hat{y}E_2 \qquad \text{(C.1)}
\end{aligned}$$

It is straightforward to see that $E_2 = E_1$ so that $E(x,z) = 2E_1(x,z)$ By replacing the Hankel function $H_0^{(1)}(k_o\sqrt{(z-z')^2+x^2})$ with the integral representation, we can simplify

Eq. (C.1). Here are the detailed steps.

$$
\begin{aligned}
& E_1(x,z) \\
= & \frac{-\omega\mu_o}{16\pi}\int_{-\infty}^{\infty} \mathrm{d}z' H_z(z') H_0^{(1)}(k_0\sqrt{(z-z')^2+x^2}) \\
= & \frac{-\omega\mu_o}{16\pi}\int_{-\infty}^{\infty} \mathrm{d}k_z T(k_z) e^{ik_x d_2} \int_{-\infty}^{\infty} \mathrm{d}z' e^{ik_z z'} (1/\pi) \int_{-\infty}^{\infty} \mathrm{d}k_z' \frac{e^{ik_x' x}}{k_x'} e^{ik_z'(z-z')} \\
= & \frac{-\omega\mu_o}{16\pi^2}\int_{-\infty}^{\infty} \mathrm{d}k_z T(k_z) e^{ik_x d_2} \int_{-\infty}^{\infty} \mathrm{d}k_z' \frac{e^{ik_x' x}}{k_x'} \int_{-\infty}^{\infty} \mathrm{d}z' e^{ik_z z'} e^{ik_z'(z-z')} \\
= & \frac{-\omega\mu_o}{16\pi^2}\int_{-\infty}^{\infty} \mathrm{d}k_z T(k_z) e^{ik_x d_2} \int_{-\infty}^{\infty} \mathrm{d}k_z' \frac{e^{ik_x' x}}{k_x'} e^{ik_z' z} 2\pi\delta(k_z - k_z') \\
= & \frac{-\omega\mu_o}{8\pi}\int_{-\infty}^{\infty} \mathrm{d}k_z T(k_z) e^{ik_x d_2} \frac{e^{ik_x x}}{k_x} e^{ik_z z}
\end{aligned}
$$

For a finite size slab, we consider a general case:

$$
\begin{aligned}
E_{y,fs}(z) &= \frac{-\omega\mu_o}{4\pi} f(z) \int_{-\infty}^{\infty} \mathrm{d}k_z \frac{T(k_z)}{k_x} e^{ik_x d_2} e^{ik_z z} \\
H_{z,fs}(z) &= \frac{-1}{4\pi} f(z) \int_{-\infty}^{\infty} \mathrm{d}k_z T(k_z) e^{ik_x d_2} e^{ik_z z}
\end{aligned}
$$

Once again, the equivalent currents can be found from the fields at the slab boundaries and the fields in image region can be found as:

$$
\begin{aligned}
& E_1(x,z) \\
= & \int_{-\infty}^{\infty} \mathrm{d}z' H_{z,fs}(z') H_0^{(1)}(k_0\sqrt{(z-z')^2+x^2}) \\
= & \frac{-\omega\mu_o}{16\pi^2}\int_{-\infty}^{\infty} \mathrm{d}k_z T(k_z) e^{ik_x d_2} \int_{-\infty}^{\infty} \mathrm{d}k_z' \frac{e^{ik_x' x}}{k_x'} \int_{-\infty}^{\infty} \mathrm{d}z' f(z') e^{ik_z z'} e^{ik_z'(z-z')} \\
= & \frac{-\omega\mu_o}{16\pi^2}\int_{-\infty}^{\infty} \mathrm{d}k_z T(k_z) e^{ik_x d_2} \int_{-\infty}^{\infty} \mathrm{d}k_z' \frac{e^{ik_x' x}}{k_x'} e^{ik_z' z} \int_{-\infty}^{\infty} \mathrm{d}z' \, f(z') e^{i(k_z - k_z')z} \\
= & \frac{-\omega\mu_o}{16\pi^2}\int_{-\infty}^{\infty} \mathrm{d}k_z T(k_z) e^{ik_x d_2} \int_{-\infty}^{\infty} \mathrm{d}k_z' \frac{e^{ik_x' x}}{k_x'} e^{ik_z' z} F(k_z - k_z')
\end{aligned}
$$

The spectrum at the image location can be obtained by inverse Fourier transform:

$$
\begin{aligned}
E(k_z) &= \int_{-\infty}^{\infty} \mathrm{d}z\, 2E_1(x_0, z)e^{-ik_z z} \\
&= \frac{-\omega\mu_o}{8\pi^2} \int_{-\infty}^{\infty} \mathrm{d}z\, e^{-ik_z z} \int_{-\infty}^{\infty} \mathrm{d}k_z' T(k_z') e^{ik_x' d_2} \int_{-\infty}^{\infty} \mathrm{d}k_z'' \frac{e^{ik_x'' x_0}}{k_x''} e^{ik_z'' z} F(k_z' - k_z'') \\
&= \frac{-\omega\mu_o}{8\pi^2} \int_{-\infty}^{\infty} \mathrm{d}k_z' T(k_z') e^{ik_x' d_2} \int_{-\infty}^{\infty} \mathrm{d}k_z'' \frac{e^{ik_x'' x_0}}{k_x''} F(k_z' - k_z'') 2\pi\delta(k_z'' - k_z) \\
&= \frac{-\omega\mu_o}{4\pi} \int_{-\infty}^{\infty} \mathrm{d}k_z' T(k_z') e^{ik_x' d_2} \frac{e^{ik_x x_0}}{k_x} F(k_z' - k_z) \\
&= \frac{-\omega\mu_o}{4\pi} \frac{e^{ik_x x_0}}{k_x} \int_{-\infty}^{\infty} \mathrm{d}k_z' T(k_z') e^{ik_x' d_2} F(k_z' - k_z) \\
&= \frac{-\omega\mu_o}{4\pi} \frac{e^{ik_x x_0}}{k_x} \{T_1(k_z) \otimes F(k_z)\}
\end{aligned}
$$

where

$$T_1(k_z) = T(k_z)e^{ik_x d_2}$$

Hence we have the spectrum of the image expressed as the convolution of the transmission coefficient and the modulation from the slab's finite size:

$$E(k_z) = \frac{-\omega\mu_o}{4\pi} \frac{e^{ik_x x_0}}{k_x} \{T_1(k_z) \otimes F(k_z)\}$$

Appendix D

Asymptotic Formula For E_z Due to z Dipole on Grounded Slabs

Referring to Fig. 4-23, Eq. (4.71) can be integrated along the branchcuts as

$$E_z = \int_{-\infty}^{+\infty} \mathrm{d}k_\rho (A_{0+}\big|_{I_1} + A_{0+}\big|_{I_2} + A_{0+}\big|_{I_3} + A_{0+}\big|_{I_4}) \sqrt{\frac{2}{k_\rho \rho \pi}} e^{i(k_\rho \rho - \pi/4)} \qquad \text{(D.1)}$$

Along each brachcut, k_{1z} and k_{0z} takes different values. By letting $k_\rho = k_1 + iq$ for the path of I_1 and I_2, $k_\rho = k_0 + iq$ for the path of I_3 and I_4 (where q is a positive real number),

we can write

$$
\begin{aligned}
k_{1z} &= \sqrt{(k_1 - k_\rho)(k_1 + k_\rho)} \\
&= \sqrt{-qe^{-i3\pi/2}}\sqrt{k_1 + k_\rho} \\
&= e^{-i\pi/4}\sqrt{q}\sqrt{k_1 + k_\rho} \qquad \text{along } I_1 \\
k_{1z} &= e^{i3\pi/4}\sqrt{q}\sqrt{k_1 + k_\rho} \qquad \text{along } I_2 \\
k_{0z} &= e^{-i\pi/4}\sqrt{q}\sqrt{k_0 + k_\rho} \qquad \text{along } I_3 \\
k_{0z} &= e^{i3\pi/4}\sqrt{q}\sqrt{k_0 + k_\rho} \qquad \text{along } I_4
\end{aligned}
$$

It is staightforward to show that $A_{0+}\big|_{I_1} - A_{0+}\big|_{I_2} = 0$. Therefore, k_1 is not a branch point. Plugging Eq. (4.73) into Eq. (D.1), we have

$$
\begin{aligned}
E_z &= i\int_0^\infty \mathrm{d}q(A_{0+}\big|_{I_3} + A_{0+}\big|_{I_4})\sqrt{\frac{2}{k_\rho \rho \pi}}e^{i(k_\rho \rho - \pi/4)} \\
&= \frac{Ilk_0^3\epsilon_1}{4\pi\omega\epsilon_o}\left[\frac{1 + e^{i2k_{1z}d}}{\epsilon_o k_{1z}}\right]^2 \frac{4\epsilon_1\sqrt{\dfrac{1}{\pi\rho}}e^{ik_o\rho}}{-(1 - e^{i2k_{1z}d})^2}\int_0^\infty \mathrm{d}q q^{1/2}e^{-\rho q} \qquad \text{(D.2)}
\end{aligned}
$$

Replacing q by s^2 to facilitate the integration, it can be shown that

$$
\int_0^\infty \mathrm{d}q q^{1/2}e^{-\rho q} = \frac{1}{2\rho}\sqrt{\frac{\pi}{\rho}}
$$

Substituting above result into Eq. (D.2), we have

$$E_z = \frac{-\mathrm{I}lk_0^2\epsilon_1^2}{2\pi\omega\epsilon_0}\left[\frac{1+e^{i2k_{1z}d}}{\epsilon_0 k_{1z}(1-e^{i2k_{1z}d})}\right]^2 \frac{e^{ik_0\rho}}{\rho^2}$$

which is Eq. (4.74).

Bibliography

[1] V. G. Veselago, "The electrodynamics of substances with simultaneously negative values of ϵ and μ," *Sov. Phys. Uspekhi*, vol. 10, no. 4, pp. 509–514, January-February 1968.

[2] J. B. Pendry, A. J. Holden, W. J. Stewart, and I. Youngs, "Extremely low frequency plasmons in metallic mesostructures," *Phys. Rev. Lett.*, vol. 76, no. 25, pp. 4773–4776, 17 June 1996.

[3] J. B. Pendry, A. J. Holten, and W. J. Stewart, "Magnetism from conductors and enhanced nonlinear phenomena," *IEEE Trans. on Microwave Theory and Techniques*, vol. 47, no. 11, pp. 2075–2084, November 1999.

[4] R. A. Schelby, D. R. Smith, and S. Schultz, "Experimental verification of a negative index of refraction," *Science*, vol. 292, pp. 77–79, April 2001.

[5] A. N. Lagarkov and V. N. Kissel, "Near-perfect imaging in a focusing system based on a Left-Handed-Material plate," *Phys. Rev. Lett.*, vol. 92, no. 7, pp. 077401, 2004.

[6] H.-S. Chen, L.-X. Ran, J.-T. Huangfu, X.-M. Zhang, K.-S. Chen, T. M. Grzegorczyk, and J. A. Kong, "Negative refraction of a combined double S-shaped metamaterial," *Applied Physics Letters*, vol. 86, pp. 151909, 2005.

[7] H.-S. Chen, L.-X. Ran, J.-T. Huangfu, X.-M. Zhang, K.-S. Chen, T. M. Grzegorczyk, and J. A. Kong, "Magnetic properties of S-shaped split-ring resonators," *Progress In Electromagnetics Research*, vol. 51, pp. 249–279, 2005.

[8] T. H. Koschny, L. Zhang, and C. M. Soukoulis, "Isotropic three-dimensional Left-Handed metamaterials," *Physical Review B*, vol. 71, no. 121103, March 2005.

[9] J. A. Kong, "Electromagnetic interactions with stratified negative isotropic media," *Progress In Electromagnetics Research (PIER)*, vol. 35, pp. 1–52, 2001.

[10] J. Lu, T. M. Grzegorczyk, Y. Zhang, J. Pacheco, B.-I. Wu, J. A. Kong, and M. Chen, "Cerenkov radiation in materials with negative permittivity and permeability," *Optics Express*, vol. 11, no. 7, pp. 723–734, 2003.

[11] A. Grbic and G. V. Eleftheriades, "Experimental verification of backward-wave radiation from a negative refractive index metamaterial," *Journal of Applied Physics*, vol. 92, no. 10, pp. 5930–5935, November 2002.

[12] L.-X. Ran, J.-T. Huangfu, H.-S. Chen, X.-M. Zhang, K.-S. Chen, T. M. Grzegorczyk, and J. A. Kong, "Beam shifting experiment for the characterization of Left-Handed properties," *J. Appl. Phys.*, vol. 95, no. 5, pp. 2238–2241, March 2004.

[13] P. R. Berman, "Goos-Hänchen shift in negative refractive media," *Phys. Rev. E*, vol. 66, no. 067603, pp. 067603, 2002.

[14] J. B. Pendry, "Negative refraction makes a perfect lens," *Phys. Rev. Lett.*, vol. 85, no. 18, pp. 3966–3969, 30 October 2000.

[15] D. R. Smith, D. Schurig, M. Rosenbluth, and S. Schultz, "Limitations on subdiffraction imaging with a negative index slab," *Applied Physics Letters*, vol. 82, no. 10, pp. 1506–1508, Mar. 2003.

[16] M. W. Feise, J. B. Schneider, and P. J. Bevelacqua, "Finite-Difference and Pseudospectral Time-Domain methods applied to backward-wave metamaterials," *IEEE Trans. on Antennas and Propagation*, vol. 52, no. 11, pp. 2955–2962, Nov. 2004.

[17] X.S. Rao and C.K. Ong, "Subwavelength imaging by a Left-Handed Material superlens," *Physical Review E*, vol. 68, no. 6, pp. 067601, Dec. 2003.

[18] M. W. Feise and Y. S. Kivshar, "Sub-wavelength imaging with a Left-Handed Material flat lens," *Physics Letters A*, vol. 334, no. 4, pp. 326–330, January 2005.

[19] L. Chen, S.-L. He, and L.-F. Shen, "Finite-size effects of a Left-Handed Material slab on the image quality," *Phys. Rev. Lett.*, vol. 92, no. 10, pp. 107404, 2004.

[20] J. J. Chen, T. M. Grzegorczyk, B.-I. Wu, and J. A. Kong, "Limitation of FDTD in simulation of a perfect lens imaging system," *Optics Express*, vol. 13, no. 26, pp. 10840, 2005.

[21] V. N. Kissel and A. N. Lagarkov, "Superresolution in Left-Handed composite structures: From homogenization to a detailed electrodynamic description," *Phys. Rev. B*, vol. 72, pp. 085111, 2005.

[22] S.-H. Jiang and R. Pike, "A full electromagnetic simulation study of near-field imaging using silver films," *New Journal of Physics*, vol. 7, no. 169, 2005.

[23] D. O. S. Melville and R. J. Blaikie, "Super-resolution imaging through a planar silver layer," *Optics Express*, vol. 13, no. 6, pp. 2127–2134, March 2005.

[24] A. Husakou and J. Herrmann, "Focusing of scanning light beams below the diffraction limit without near-field spatial control using a saturable absorber and a negative-refraction material," *Phys. Rev. Lett.*, vol. 96, no. 013902, 2005.

[25] W.-T. Lu and S. Sridhar, "Flat lens without optical axis: Theory of imaging," *Optical Express*, vol. 13, no. 26, pp. 10673, 2005.

[26] J. D. Wilson and Z. D. Schwartz, "Multifocal flat lens with Left-Handed metamaterial," *Applied Physics Letters*, vol. 86, no. 02, pp. 021113, January 2005.

[27] T. M. Grzegorczyk, X. Chen, J. Pacheco, J. J. Chen, B.-I. Wu, and J. A. Kong, "Reflection coefficeints and Goos-Hänchen shifts in anisotropic and bianisotropic Left-Handed metamaterials," *Progress In Electromagnetic Research*, vol. 51, no. 1, pp. 83–113, 2005.

[28] J. J. Chen, T. M. Grzegorczyk, B.-I. Wu, and J. A. Kong, "Role of evanescent waves in the positive and negative Goos-Hänchen shifts with Left-Handed Material slabs," *Journal of Applied Physics*, vol. 98, no. 094905, 2005.

[29] B.-I. Wu, T. M. Grzegorczyk, Y. Zhang, and J. A. Kong, "Guided modes with imaginary transverse wave number in a slab waveguide with negative permittivity and permeability," *Journal of Applied Physics*, vol. 98, no. 11, pp. 9386–9388, 2003.

[30] P. Baccarelli, P. Burghignoli, F. Frezza, A. Galli, P. Lampariello, G. Lovat, and S. Paulotto, "Fundamental modal properties of surface waves on metamaterial grounded slabs," *IEEE Transactions on Microwave Theory and Techniques*, vol. 53, no. 4, pp. 1431– 1442, April 2005.

[31] P. Baccarelli, P. Burghignoli, F. Frezza, A. Galli, P. Lampariello, G. Lovat, and S. Paulotto, "Effects of leaky-wave propagation in metamaterial grounded slabs excited by a dipole source," *IEEE Transactions on Microwave Theory and Techniques*, vol. 53, no. 1, pp. 13, January 2005.

[32] C. Li, Q. Sui, and F. Li, "Complex guided wave solutions of grounded dielectric slab made of metamaterials," *Progress In Electromagnetics Research (PIER)*, vol. 51, pp. 187–195, 2005.

[33] T.-J. Cui, Q. Cheng, W.-B. Lu, Q. Jiang, and J. A. Kong, "Localization of electromagnetic energy using a Left-Handed-Medium slab," *Physical Review B*, vol. 71, no. 045114, 2005.

[34] I. V. Shadrivov, R. W. Ziolkowski, A. A. Zharov, and Y. S. Kivshar, "Excitation of guided waves in layered structures with negative refraction," *Optics Express*, vol. 13, no. 2, pp. 481–492, Jan. 2005.

[35] S. Rikte, G. Kristensson, and M. Andersson, "Propagation in bianisotropic media - reflection and transmission," *IEE Proc.-Microw. Antennas Propag.*, vol. 148, no. 1, pp. 29–36, February 2001.

[36] I. V. Shadrivov, A. A. Sukhorukov, and Y. S. Kivshar, "Beam shaping by a periodic structure with negative refraction," *Applied Physics Letters*, vol. 82, no. 22, pp. 3820–3822, June 2003.

[37] Von F. Goos and H. Hänchen, "Ein neuer und fundamentaler versuch zur totalreflexion," *Ann. der Phys.*, vol. 6, pp. 333–346, 1947.

[38] L. M. Brekhovskikh, *Waves in layered media*, Academic Press, New York, 2nd edition, 1980.

[39] B. R. Horowitz and T. Tamir, "Lateral displacement of a light beam at a dielectric interface," *Journal of the Optical Society of America*, vol. 61, no. 5, pp. 586–594, May 1971.

[40] A. Lakhtakia, "Positive and negative Goos-Hänchen shifts and negative phase-veloctiy mediums," *Aeu-International Journal of Electronics and Communications*, vol. 58, no. 3, pp. 229–231, 2004.

[41] R. W. Ziolkowski, "Pulsed and CW Gausssian beam interactions with double negative metamaterial slabs," *Optics Express*, vol. 11, no. 7, pp. 662–681, apr 2003.

[42] J. A. Kong, *Electromagnetic Wave Theory*, EMW, Cambridge, MA, 2005.

[43] R. Ruppin, "Surface polaritons of a Left-Handed Medium," *Physics Letters A*, vol. 277, pp. 61–64, Oct. 2000.

[44] I. V. Shadrivov, A. A. Zharov, and Y. S. Kivshar, "Giant Goos-Hänchen effect at the reflection from Left-Handed metamaterials," *Applied Physics Letters*, vol. 83, pp. 2713–2715, Sep. 2003.

[45] R. W. Ziolkowski and E. Heyman, "Wave propagation in media having negative permittivity and permeability," *Phys. Rev. E*, vol. 64, no. 056625, Oct. 2001.

[46] I. V. Shadrivov, A. A. Sukhorukov, and Y. S. Kivshar, "Guided modes in negative-refractive-index waveguides," *Physical Review E*, vol. 67, no. 057602, pp. 057602, May 2003.

[47] H. M. Lai, C. W. Kwok, Y. W. Loo, and B. Y. Xu, "Energy-flux pattern in the Goos-Hänchen shift effect," *Phys. Rev. E*, vol. 62, no. 5, pp. 7330–7339, Nov. 2000.

[48] S. A. Cummer, "Simulated causal subwavelength focusing by a negative refractive index slab," *Applied Physics Letters*, vol. 82, no. 10, pp. 1503–1505, Mar. 2003.

[49] A. Taflove, *Computational Electrodynamics - The Finite-Difference Time-Domain Method*, Artech House, 1995.

[50] J. Lu, T. M. Grzegorczyk, B.-I. Wu, J. Pacheco, M. Chen, and J. A. Kong, "Effect of poles on subwavelength focusing by an LHM slab," *Microwave Opt. Technol. Lett.*, vol. 45, no. 1, pp. 49, April 2005.

[51] P. Baccarelli, P. Burghignoli, F. Frezza, A. Galli, P. Lampariello, G. Lovat, and S. Paulotto, "The nature of radiation from leaky waves on single- and double-negative metamaterial grounded slabs," *IEEE Microwave Symposium Digest, 2004 IEEE MTT-S International*, vol. 1, pp. 309–312, June 2004.

[52] J. D. Joannopoulos, R. D. Meade, and J. N. Winn, *Photonic Crystals, Molding the Flow of Light*, Princeton University Press, 1995.

[53] M. Sigalas, C. T. Chan, K. M. Ho, and C. M. Soukoulis, "Metallic Photonic Band-Gap materials," *Physical Review B*, vol. 52, no. 16, pp. 11744–11751, Oct. 1995.

[54] A. de Lustrac, F. Gadot, S. Cabaret, J. M. Lourtioz, T. Brillat, A. Priou, and E. Akmansoy, "Experimental demonstration of electrically controllable Photonic Crystals at centimeter wavelengths," *Appl. Phys. Lett.*, vol. 75, no. 11, pp. 1625–1627, 1999.

[55] D. F. Sievenpiper, E. Yablonovitch, J. N. Winn, S. Fan, P. R. Villeneuve, and J. D. Joannopoulos, "3D metallo-dielectric Photonic Crystals with strong capacitive coupling between metallic islands," *Phys. Rev. Lett.*, vol. 80, no. 13, pp. 2829–2832, Mar. 1998.

[56] D. Sievenpiper, L.-J. Zhang, R. F. J. Broas, N. G. Alexopolous, and E. Yablonovitch, "High-impedance electromagnetic surfaces with a forbidden frequency band," *IEEE Trans. Microwave Theory and Techniques*, vol. 47, no. 11, pp. 2059–2074, Nov. 1999.

[57] J. R. Mosig, *Numerical Techniques for Microwave and Millimeter-Wave Passive Structures, chapter 3*, T. Itoh Ed., Wiley Interscience, USA, 1989.

[58] K. A. Michalski and J. R. Mosig, "Multilayered media Green's functions in integral equation formulations," *IEEE Trans. Antennas Propagat.*, vol. 45, pp. 508–519, Mar 1997.

[59] T. M. Grzegorczyk, *Integrated 3D Antennas For Millimeter-Wave Applications: Theoretical Study and Technological Realization*, Ph.D. Thesis, Swiss Federal Institute of Technology, Lausanne, Switzerland, 2000.

[60] J. R. Mosig and F. E. Gardiol, "General integral equation formulations for microstrip antennas and scatterers," *IEE proc. Part H: Microwaves. Opt. Antennas,*, vol. 132, pp. 424–432, 1985.

[61] L. Felsen and N. Marcuvitz, *Radiation and Scattering of Waves*, Prentice Hall, New Jersey, USA, 1973.

[62] T. O. Espelid and K. J. Overholt, "An algorithm for automatic integration of infinite oscillating tails," *Num. Algorithms*, vol. 8, pp. 83–101, 1994.

[63] C. Brezinski and M. Redivo Zaglia, *Extrapolation Methods, Theory and Practice*, North-Holland, New York, 1991.

[64] M. Siegel and R. W. P. King, "Electromagnetic fields in a dissipative half-space: A numerical approach," *J. Appl. Phys.*, vol. 41, pp. 2415–2423, 1970.

[65] J. Ryu, H. F. Morrison, and S. H. Ward, "Electromagnetic fields about a loop source of current," *Geophys.*, vol. 35, pp. 862–896, Oct. 1970.

[66] J. P. Boris and E. S. Oran, "Evaluation of oscillatory integrals," *J. Comput. Phy.*, vol. 17, pp. 425–433, 1975.

[67] G. Pantis, "The evaluation of integrals with oscillatory integrands," *J. Comput. Phy.*, vol. 17, pp. 229–233, 1975.

[68] K. A. Michalski, "On the efficient evaluation of integrals arising in the Sommerfeld halfspace problem," *IEE proc. Part H: Microwaves. Opt. Antennas,*, vol. 132, pp. 312–318, 1985.

[69] K. A. Michalski, "Extrapolation methods for Sommerfeld integral tails," *IEEE Trans. Antennas Propagat.*, vol. 46, no. 10, pp. 1405–1418, 1998.

[70] J. R. Mosig and F. E. Gardiol, "A dynamical radiation model for microstrip structures," *Adv. Electron. Electron Phys., P. W. Hawkes, Ed.*, vol. 59, pp. 139–237, 1982.

[71] J. R. Mosig and F. E. Gardiol, "Analytic and numerical techniques in the Green's function treatment of microstrip antennas and scatterers," *Proc. Inst. Elect. Eng. pt. H*, vol. 130, pp. 175–182, Mar. 1983.

[72] A. Sidi, "Extrapolation methods for divergent oscillatory infinite integrals that are defined in the sense of Summability," *J. Comput. Appl. Math.*, vol. 17, pp. 105–114, 1987.

[73] C. M. Bender and S. A. Orszag, *Advanced Mathematical Methods for Scientists and Engineers*, McGraw-Hill, New York, 1978.

[74] G. J. Burke, E. K. Miller, J. N. Brittingham, D. L. Lagerand R. J. Lytle, and J. T. Okada, "Computer modeling of antennas near the ground," *Electromagn.*, vol. 1, no. 29-49, Jan. 1981.

[75] H. Cory and A. Barger, "Surface-wave propagation along a metamaterial slab," *Microwave Opt. Technol. Lett.*, vol. 38, pp. 392, Sept. 2003.

[76] P. Baccarelli, P. Burghignoli, G. Lovat, and S. Paulotto, "Surface-wave suppression in a double-negative metamaterial grounded slab," *IEEE Trans. Antennas Wireless Propag. Lett.*, vol. 2, no. 19, pp. 269, 2003.

[77] P. Baccarelli, P. Burghignoli, F. Frezza, A. Galli, P. Lampariello, G. Lovat, and S. Paulotto, "New dispersion characteristics and surface-wave suppression in double-negative metamaterial grounded slabs," *Int. Electromagnetic Theory Symp. in URSI*, vol. 1, pp. 379, May 2004.

[78] R. E. Collin, *Field Theory of Guided Waves*, IEEE press, New York, USA, 1990.

[79] A. A. Oliner and T. Tamir, "Backward waves on isotropic plasma slabs," *J. Appl. Phys.*, vol. 33, pp. 231, 1962.

[80] J. H. Holland, *Adaptation in Natural and Artificial Systems*, University of Michigan Press, Ann Arbor, Michigan, 1975.

[81] C. R. Reeves and J. E. Rowe, *Genetic Algorithms - Principles and Perspectives, a guide to GA theory*, Kluwer Academic Publishers, Norwell, Massachusetts, 2003.

[82] R. L. Haupt and S. E. Haupt, *Practical Genetic Algorithms*, John Wiley & sons, Inc., Hoboken, New Jersey, 2004.